LUMINESCENT SiC_xN_y THIN FILMS DEPOSITED BY ICP-CVD

LUMINESCENT SiC_xN_y THIN FILMS

DEPOSITED BY ICP-CVD

By

KAYNE DUNN, B. Sc.

A Thesis
Submitted to the School of Graduate Studies
in Partial Fulfilment of the Requirements
for the Degree
Master of Applied Sciences

McMaster University

MASTER OF APPLIED SCIENCE (2011) McMaster University

(Engineering Physics) Hamilton, Ontario

TITLE: LUMINESCENT SiC_xN_y THIN FILMS DEPOSITED BY ICP-CVD

AUTHOR: Kayne Dunn

SUPERVISOR: Dr. P. Mascher

NUMBER OF PAGES: xvii, 136

Abstract

In current microelectronic interconnect technology, significant delay is incurred due to capacitances in the intermediate and global interconnect layers. To avoid capacitive effects optical interconnects can be used; however conventional technologies are expensive to manufacture. One method to address these issues is to make use of quantum confinement effects and states lying within the bandgap of the material to enhance luminescence in a CMOS compatible silicon based system. Thin SiC_xN_y films appear to be suitable to work as luminescent silicon based films due to their lower direct bandgap and chemical stability but have not yet been studied in great detail.

This thesis is an exploratory work aiming to assess the suitability of SiC_xN_y films for the above applications and to identify future research areas. The films analyzed in this thesis were manufactured on the inductively coupled plasma-chemical vapour deposition reactor (ICP-CVD) at McMaster University. The ICP-CVD produces films of high uniformity by using a remote RF plasma and an arrangement of high vacuum pumps to attain a vacuum on the order of 10^{-7}Torr.

Several experimental techniques have been used to analyse the films. The complex index of refraction has been determined through the use of ellipsometry giving results typical of that of a-SiN_x:H. The photoluminescence spectroscopy results show a large broad emission peak with at least one shoulder at higher energies. The precise luminescence mechanism(s) could not be identified though a strong relationship with the bonding state of nitrogen has been found. The composition and structure of the films, as determined through ion beam measurements, infrared absorption measurements, and transmission electron microscopy measurements demonstrate the formation of a two-phase structure consisting of carbon rich clusters surrounded by a mostly silicon nitride matrix. These carbon rich regions have some graphitic character and act to dampen the luminescence.

Acknowledgements

There are many people I must thank for the skills, expertise, and support they have lent me during the completion of my degree and this thesis. First and foremost comes Dr. Peter Mascher, who took me on as a graduate student having faith in my capability to perform meaningful research. He started me down the path and then gave me the freedom to pursue the research where I felt it led. Also, his patience with me while I completed this thesis was exceptional and my gratitude in this regard is profound.

Dr. Jacek Wojcik has been instrumental in the development of this thesis. For his help with the fundamentals of thin film deposition when I was just beginning, his greatly appreciated work in the ellipsometric measurements, his friendly help and guidance on a day to day basis, and his encouragement to attend conferences he is greatly appreciated.

Graham Pearson and Martin Gerber both deserve recognition for their help in introducing and training me to use some of the equipment in the lab, especially for introducing me to the FTIR technique and interferometer which has given good results and is a key component of my thesis.

Dr. Tyler Roschuk and Patrick Wilson deserve a great deal of thanks for their patience and help, day-in, day-out in the office. Coming into my degree without prior research experience made the transition to graduate life difficult enough; without their help it would have been made nearly impossible.

Evgueni Chelomentsev has been the person to actually deposit the vast majority of the films in this thesis (ever since I broke the system’s shutter), for this, and for his general helpfulness in all the practicalities of thin film deposition I am extremely grateful.

The staff of the Canadian Centre for Electron Microscopy, Dr.'s Fred Pearson, Carmen Andrei, Martin Couillard all deserve recognition for taking a novice like me and teaching me something about electron microscopy.

Many others contributed to this thesis in some way, too many to list here, except for one: my new wife Susan has been a source of support and comfort without which this thesis would not have happened.

A final mark of gratitude must be given to McMaster University, the Canadian Institute for Photonics Innovation, and the Natural Sciences and Engineering Research Council for providing the funding to support this work.

Table of Contents

List of Figures

List of Tables

Acronyms

AD	As deposited	IR	Infrared
AFM	Atomic force microscope	ITO	Indium tin oxide
CCD	Charge coupled device	I-V	Current-voltage
CCEM	Canadian Center for Electron Microscopy	LDA	Local density approximation
CLS	Canadian Light Source	LED	Light emitting diode
CMOS	Complementary metal oxide semiconductor	MEMS	Micro electro-mechanical system
CRSC	Carbon rich silicon carbide	MIS	Metal insulator semiconductor
C-V	Capacitance-voltage	MOSFETS	Metal oxide semiconductor field effect transistor
CVD	Chemical vapour deposition	MWCVD	Microwave chemical vapour deposition
DC	Direct current	NIR	Near infrared
DFT	Density functional theory	OPD	Optical path difference
DOS	Density of states	PDS	Photothermal deflection spectroscopy
EDX	Energy dispersive x-ray spectroscopy	PECVD	Plasma enhanced chemical vapour deposition
EELS	Electron energy loss spectroscopy	PID	Proportional-integral-differential
EFTEM	Energy filtered transmission electron microscopy	PL	photoluminescence
EL	Electroluminescence	PLD	Pulsed laser deposition
ERD	Elastic recoil detection	PLE	Photoluminescence excitation
EXAFS	Extended X-ray absorption fine structure	PMT	Photo multiplier tube
FTIR	Fourier transform infrared spectroscopy	RBS	Rutherford backscattering spectormetry
GDFT	Generalized density functional theory	RDF	Radial distribution function
HFCVD	Hot filament chemical vapour deposition	RF	Radio frequency
ICP-CVD	Inductively coupled plasma-chemical vapour deposition	SAD	Selected area diffraction

SOI	Silicon on insulator
SRSC	Silicon rich silicon carbide
SRSN	Silicon rich silicon nitride
SRSO	Silicon rich silicon oxide
STEM	Scanning transmission electron microscope
STEM-EELS	Scanning transmission electron microscope -electron energy loss spectroscopy
TEM	Transmission electron microscope
UHP+	Ultra high purity +
UV-Vis	Ultraviolet-visible
UWO	University of Western Ontario
VASE	Variable angle spectroscopic ellipsometry
VLSPGM	Variable line spacing-plane grating monochromator
XANES	X-ray absorption near edge spectroscopy
XAS	X-ray absorption fine structure
ZLP	Zero loss peak

Chapter 1 : Introduction

The purpose of this research, and indeed almost all research into silicon photonics, is to leverage the expertise and equipment capabilities of the microelectronics industry for photonic applications. In practice this means the development of detectors, modulators, waveguides, couplers and, last but not least, a light source.

In 1965 Gordon Moore, who would later co-found Intel, made a famous observation that "The complexity for minimum component costs has increased at a rate of roughly a factor of two per year [1]." Though later modified to every two years, this statement, dubbed Moore's Law, has become a self fulfilling prediction of progress in integrated electronics. Though this trend can't continue indefinitely it has been maintained through serious technical challenges in the past. The conventional way to achieve this is to shrink the transistor and interconnects (a deceptively simple description to the numerous problems which have been encountered and overcome) to reduce RC time delay. However, this approach is fast coming upon fundamental limits including the lower limits to gate dielectric thickness and channel length, and, the issue that this work hopes to contribute to: interconnects. To illustrate this problem, and referring to Figure 1-1, we follow the analysis in [2]. Consider the interconnect as a resistor, R, in series, with two parallel capacitances. The interconnect delay τ_C, is approximately

$$\tau_C = 0.89RC = 0.89K_I\left(\frac{\rho L}{A}\right)(C_I + C_S) = 0.89(2)\left(\frac{\rho L}{HW}\right)\left(K_{ox}\varepsilon_0\frac{HL}{L_S} + K_{ox}\varepsilon_0\frac{WL}{X_{ox}}\right) \qquad (1\text{-}1)$$

Where K_I is an empirical constant typically taken to be around two, K_{ox} is the relative dielectric constant of the dielectric layer, ρ is the resistivity of the interconnect, and the other variables are defined as in Figure 1-1. If one assumes that H, W, L_S and x_{ox} are all of the same order of magnitude, approximating each as length, F, gives

$$\tau_C \sim 1.78\left(\frac{\rho L}{F^2}\right)\left(K_{ox}\varepsilon_0\frac{FL}{F} + K_{ox}\varepsilon_0\frac{FL}{F}\right) = 3.56K_{ox}\varepsilon_0\left(\frac{\rho L^2}{F^2}\right) \qquad (1\text{-}2)$$

So, we see that for local interconnects, where both F and L scale in rough proportion to each other, the time constant does not change. However, in the case of global interconnects, see Figure 1-2, where the length of the global interconnects stays relatively constant, the interconnect delay increases. Physically, this change in the RC time constant is interpreted as an increase in R due to the smaller cross section, but a relatively constant C value as the capacitance reduction due to scaling is negated by the decreasing interconnect distance.

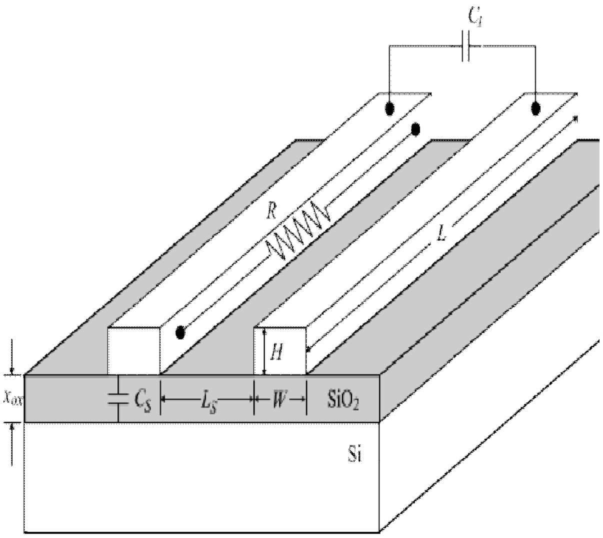

Figure 1-1: Diagram of interconnect position and interactions. Recreated from [2].

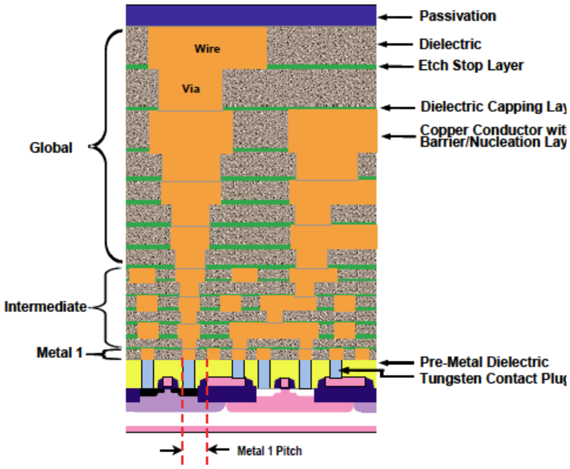

Figure 1-2: Schematic of a microelectronic circuit with multiple interconnect layers [3].

A further effect of this decreasing interconnect distance (L_S) is that the degree of interference caused between nearby wires, called cross-talk, increases with scaling thereby degrading the signal quality. A final major issue caused by interconnect scaling is the increase in Joule heating (I^2R losses) due to the increased interconnect resistance.

There have been four main revolutionary proposals for new interconnect structures to resolve this problem (note that reduction of the dielectric constant of the medium would be sufficient for at most one generation of scaling, and that would require a free space medium): 1) manufacture the circuits in three dimensions, 2) replace the electron conducting interconnects with RF waveguides, 3) use MEMS switched interconnects, and finally 4) replace the interconnects with optical waveguide interconnects. This last approach is the solution where this thesis hopes to contribute.

As a final item for consideration, when evaluating a new material for silicon photonics one should be aware of the methods which have already been successfully employed in generating lasing in a silicon based material. Each of these methods uses principles other than those of the quantum confinement and defect related luminescence studies. The most famous of them is the stimulated Raman laser first reported in [4]. This was the first device to demonstrate lasing in silicon, making use of the high stimulated Raman scattering coefficient, and the relatively high refractive index of silicon (around 4). This allows for greater mode confinement to produce optically pumped gain and was used to produce lasing in a silicon rib waveguide in a ring resonator configuration. A key drawback to implementing this kind of device in inter- and intra-chip communication applications is that optical pumping is necessary. Another type of device, significant for the fact that it has actually been implemented in commercial devices, is the result of the so called hybrid approach involving both III-V materials and silicon. The most famous of these systems, which was developed by Bowers' group at the University of California at Santa Barbara and Intel, involved a conventional InAlGaAs multiple quantum well structure wafer bonded to SOI rib waveguides which serve to distribute the light signal [5]. Finally, a photonic crystal created through reactive ion etching of holes into a SOI substrate demonstrated gain and stimulated emission under an optical pump at cryogenic temperatures [6]. While this device has not been useful for the target applications, future developments enabling higher temperature operation and electrical stimulation would provide an extremely flexible and powerful solution to the light source problem.

The other major research thrust in the development of a silicon based light source is for solid state lighting applications, where a light emitting diode or similar device is used for illumination purposes instead of the traditional incandescent and fluorescent light bulbs. For this application silicon based light sources face very strong competition in the mature technology of III-V LEDs, and in the relatively new, yet very promising organic LED technology. Silicon based light emission is usually targeted towards so-called "planar" lighting applications, where the luminescence originates from a relatively large surface area as opposed to a point as with conventional LEDs. However, one advantage of conventional LEDs is that converting its point source distribution to a planar distribution results in a more efficient device than the silicon based approach even though the conversion process is lossy.

The goal of this thesis is to be an exploratory work attempting to identify potential strengths and weaknesses of a-SiC_xN_y:H as a material for the production of a silicon based injection laser, suitable for integration in the CMOS procedural framework. Many properties of the films and light emission characteristics are examined within this thesis, but a comprehensive analysis of all properties across the entire compositional and preparative space is well beyond its scope. There are two fundamental reasons that a-SiC_xN_y:H is interesting. First, when compared with amorphous silicon nitride, it is expected to have a smaller bandgap, which promotes radiative recombination of charge carriers. Second, a-SiC_xN_y:H has a higher refractive index allowing for a greater index contrast between it and silicon oxide, which would be suitable as the dielectric layer in the CMOS stack. Another reason that a-SiC_xN_y:H is interesting is that the large compositional space should allow for extensive material optimization for applications with potentially different structures forming with different preparation methods. This means that more recombination pathways can exist allowing, hopefully, for the creation of a white light LED.

Now that the technical problem has been identified, the organization of this thesis can be outlined. Following this introductory chapter where we reviewed the basic problem the research is meant to address, chapter 2 begins by reviewing some of the most promising proposed materials for the development of luminescent silicon. It is not intended that this review could be anything close to an exhaustive review of all the methods and ideas brought to the fray in developing luminescent silicon. This would be an impossible endeavour due to the large volume of published work. Rather, I hope only to provide the context for my research that it may be meaningfully evaluated. In Chapter 3 the process by which the samples are manufactured is described. The deposition reactor, its structure, operating principles, and parameters of interest are described. This is followed by a discussion of the annealing process. The chapter concludes with a short review of silicon carbon nitride properties. In Chapter 4, the theoretical background behind the major characterization tools used in this thesis is given. That is: ellipsometry, Rutherford backscattering spectrometry (RBS) and elastic recoil detection (ERD), infrared spectroscopy, photoluminescence (PL), x-ray absorption near edge spectroscopy (XANES), electron microscopy and electron energy loss spectroscopy (EELS). In Chapter 5 the results of the experiments are given concurrently with a description thereof, leading to a discussion of the role of carbon in the a-SiC_xN_y:H, focussing on its structure and its impact on the luminescent process. Chapter 6 is devoted to the discussion of the possibilities for future research in this field, which primarily involves an expansion of the deposition parameters. I have produced many samples in the pursuit of this thesis but, this is a *quaternary* system which is a relatively recent arrival in materials analysis, so the effect of changing various parameters is not fully understood. Finally, Chapter 7 concludes this thesis by summarizing the main experimental results.

Chapter 2 : Material Systems for Luminescent Silicon

L. Canham *et al.* started the field of searching for luminescent silicon in 1990 when, after subjecting silicon to an electrochemical etch, intense photoluminescent activity was observed [7]. This etch formed a highly porous material, consisting of nanoscale wires and clusters. The photoluminescence has most commonly been attributed to quantum confinement effects by analogy with the "particle in the box" problem. However, other proposed mechanisms for the luminescence, such as surface state recombination, also play a role in the photoluminescence spectra [8]. A great deal of work has been published on porous silicon, however, the structural and chemical instability are major drawbacks for the implementation of an efficient, reliable electroluminescent device.

By far the most researched and best understood system using quantum confinement effects for light emission is silicon-rich silicon oxide (SRSO) where silicon nanoclusters (amorphous or crystalline) are formed through post-deposition thermal annealing. While this will be covered in more detail later, the basic principle is to shrink crystals or clusters of silicon down to such a scale that the symmetries which result in the bulk band structure are broken. Light emission can then occur within the nanocluster itself. In Figure 2-1 we see an example of the high quality of nanocrystals that can be obtained. The crystals are large, and possess well aligned crystal axes as the diffraction fringes from the lattice clearly demonstrate (These can be compared to results from the darker region near the right of the image, representing the substrate or the even darker line which represents the interface between film and substrate). The dominant

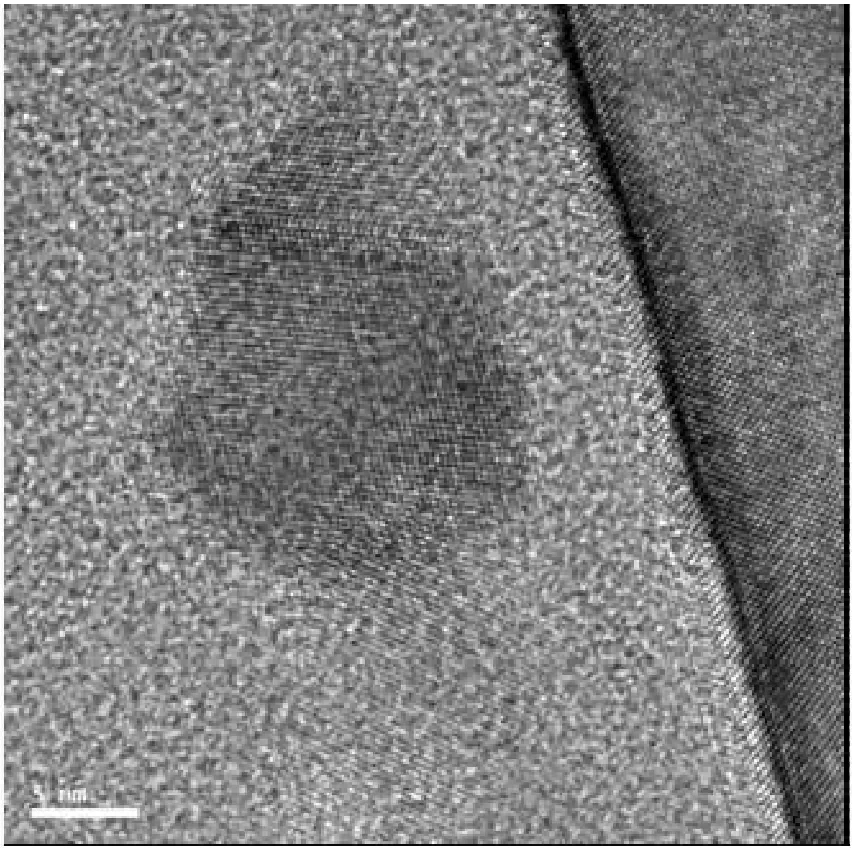

Figure 2-1: Example of silicon nanocrystals in a silicon rich silicon oxide film [11].

manufacturing methods are typically one of the many variants of sputtering or chemical vapour deposition (CVD), or thermal growth of a stoichiometric oxide followed by silicon implantation, all of which lead to films with different properties. Usually the films are subsequently annealed to promote nanocrystal growth (as well as repair implant damage), which results in a distribution in cluster diameter of a few nanometers. For instance in [9] a thermally grown oxide was implanted with silicon and nanocluster size and distribution were measured through several transmission electron microscope (TEM) techniques. As expected, the position of the nanoclusters followed a Gaussian distribution similar to that of the implant profile with mean cluster sizes between 5.6 and 7nm depending on whether dark field, scanning transmission electron microscope (STEM) angular dark field, or Z-contrast imaging was used. In addition it was found that 12% of the clusters were amorphous [9]. On the other hand, Iacona *et al.* [10] found nanocrystals between 1.4 and 4.2nm in diameter that were homogeneously distributed throughout their CVD grown SRSO films.

Silica is an excellent material choice for several reasons, not the least of which is its familiarity to semiconductor professionals in the field. It is relatively easy to grow thermally, and it has a low refractive index which makes it suitable for wave guiding in silicon. However silica, while an excellent material for the advancement of the field, presents some fundamental limitations that prevent it from being the ultimate commercial material. First, the bandgap of silica is approximately 8.9eV, which is very large when compared with other materials, and implies that very large fields will be required for the operation of an EL device. This is confirmed in the literature. For instance, Creazzo *et al.* [12] contacted a plasma enhanced chemical vapour deposition (PECVD) grown silica/silicon superlattice with indium tin oxide (ITO) and had to apply a field of more than 1MV/cm for EL to occur. As the field strength was increased the luminescence signal intensity also increased. However, the actual electron transport mechanism responsible for the electroluminescence (Frenkel-Poole conduction or Fowler-Nordheim conduction) could not be distinguished. Typical external quantum efficiencies for EL fall in the 10^{-6} range, unsuitable for practical application. S. Prezioso *et al.* [13] performed I-V, C-V and EL measurements on their silicon oxynitride films (<10% nitrogen) and were able to develop an equivalent circuit model from their results. Their luminescence results are shown in Figure 2-2. The samples were made using SiH_4, N_2O and NH_3 in a PECVD process. Contact pads were formed from aluminum, and layers of silicon nitride and silicon oxide were deposited to improve the light extraction efficiency. From electrical measurements they determined that hot-electron injection (i.e. Frenkel-Poole conduction) followed by impact ionization of the nanocluster was responsible for the EL signal.

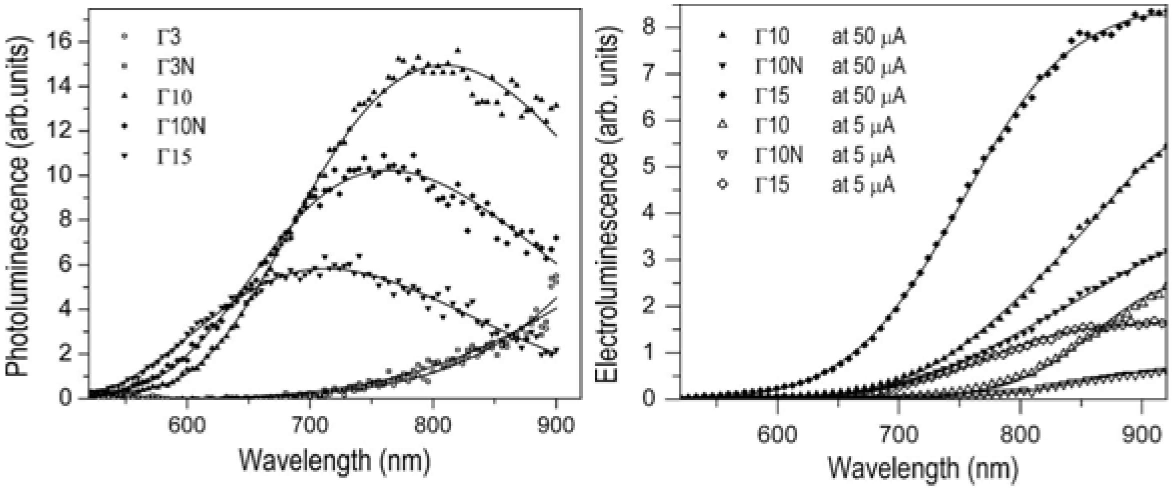

Figure 2-2: PL, left, and EL, right, reproduced with permission from [13]. The films are labelled according to the ratio of N_2O to SiH_4 flow rates used during deposition, (indicated by the number) and by the presence of an additional flow of NH_3 (indicated by the N). The PL shows a shift to shorter wavelengths as the silicon concentration decreases. The EL intensity increases sub-linearly with input current as well as shifting to longer wavelengths.

A significant cause of the difficulty of obtaining high energy emission from silicon nanocrystals embedded in an oxide matrix is the presence of low energy states at the interface between the nanocrystals and the oxide matrix. These highly localized states pin the energy of the excited electron so that recombination energies, and hence PL/EL curves, lie mostly in the near infrared (NIR) with very low emission in the visible. The physical origin of these states has been the subject of some debate with two main possibilities being identified. The first is the presence of an oxygen atom bonded to two nanocrystal silicon atoms (the oxygen bridging bond), the second is an oxygen atom double bonded to a single nanocrystal silicon atom. Molecular dynamics simulations performed in [14] found both bridging oxygen between two nanocrystal silicon atoms as well as oxygen connected between a silicon atom in the matrix and in the nanocrystal. In addition the authors of [14] found that the spherical shape typically obtained for nanocrystals was the preferred shape at crystal sizes less than 5nm, beyond which faceting begins to occur. The formation of silicon to oxygen double bonds however, was found to be unlikely, which is in agreement with [15]. The results of the unconstrained molecular dynamics simulations of [15] identify various defects present near the nanocluster-matrix interface and the authors found it likely that these defects were responsible for the optical properties of SRSO nanocrystals. On the other hand, recent experimental work, [16], has used the quantum confinement interpretation to explain the time dependent properties of PL spectra through a dependence on the degree of crystallinity of the nanoclusters. It is claimed that as the clusters become more amorphous, defect states promote non-radiative recombination. Indeed, new models for describing the luminescence mechanism are still being put forth, such as the blinking methods of K. Dunn *et al.* in [17]. This lack of a definitive understanding of the luminescence process in SRSO, by far the most studied of the candidate materials, does not bode well for other materials like silicon nitride.

A significant advantage of silicon dioxide as the cluster matrix is that optical gain is definitely possible. A landmark study published by Pavesi *et al.* in Nature, [18], showed that optical gain is possible in silica containing silicon nanocrystals, and even comparable to that found in the more established III-V materials, using the variable length stripe method. This method essentially involves exposing more and more of the potential gain material to the laser and recording the quantity of emitted power. If the material exhibits gain, then a super-linear dependence will be exhibited in a plot of light intensity versus strip length exposed.

A typical attempt to generate EL is to use the conceptually simple metal-insulator-semiconductor (MIS) structure. Usually these devices are driven with a direct current in the hope that recombination of the electrons and holes occurs at a luminescent site. However, referring once again to the importance of interface effects in the Si-SiO_2 system, Lorenzo Pavesi's group has found that carriers will preferentially travel along the lower energy states present at the nanocrystal interface avoiding the luminescent nanocrystals [19]. This is not to say

that research in oxide materials is pointless, as a further advantage of the oxide based system is that it forms naturally in air, making it cheap and relatively easy to produce via many different methods. Also, the production of more exotic structures, for instance the core-shell silica-silicon colloidal quantum dots produced in [20] potentially open up other wide fields of application.

In silica optical fibres, there is an absorption minimum at approximately 1550nm, the so-called third absorption window or C-band. This happens to be nearly the same wavelength as the emission from the erbium ${}^4I_{13/2} \rightarrow {}^4I_{15/2}$ transition at approximately 1540nm. For inter-chip communication in silica waveguides, this transition wavelength gives a significant advantage to Er doped silicon. However, for intra-chip communication the relatively long transition wavelength, which necessitates relatively large waveguides and bend radii, could be impractical. An additional hurdle to the implementation of devices based on erbium doping is that erbium has a low solid solubility in silicon and thus tends to form non-radiative clusters. The reduction in distance between erbium ions that this entails results in strong coupling between the ions and reduced luminescence [21]. The solubility can be increased through adding oxygen, and has the added advantage of increasing the luminescence at 1540nm [21]. This much stronger luminescence originates from erbium ions with six-fold oxygen coordination. Figure 2-3 shows the PL and EL from an erbium doped SRSO sample produced by co-sputtering silicon, silica and erbium oxide with annealing done at 900˚C for 1 hour in nitrogen [22]. The EL is broadened due to experimental choices but both spectra clearly indicate erbium emission. The most commonly held view on the erbium excitation mechanism is that the pump laser or electron current excites the silicon nanoclusters which then transfer the energy to the erbium dopants for radiation. In [22] the erbium luminescence is attributed to hole injection from the substrate and electron injection from the ITO (no luminescence was observed in reverse bias) into the silicon nanoclusters with the energy transfer occurring excitonically. Erbium transmission has been studied in many material systems other than that of silicon oxide, including: crystalline silicon, porous silicon, silicon carbide, amorphous silicon (hydrogenated and not), silicon nitride, and silicon germanium, and likely others as well.

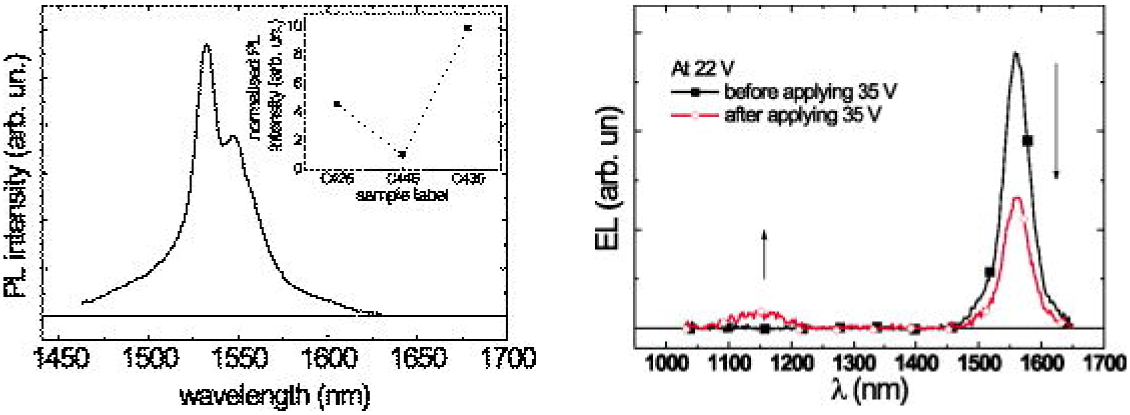

Figure 2-3: PL (left) and EL (right) of erbium doped silicon oxide produced in[22].

There has also been some very interesting work involving ion implanting carbon alongside silicon ions into a silica layer and subjecting the sample to a post deposition anneal [23]. These carbon atoms have the effect of producing additional peaks in the PL spectra; as a result the emission appears white to the eye.

There has been a great deal of interest in silicon nitride in recent years in the hope that it can alleviate the difficulty of carrier injection with nanocrystals in a silicon dioxide matrix. Crystalline silicon nitride is a hard, wide-bandgap (around 5eV though it depends on the crystalline form) material, with an ideal stoichiometry of Si_3N_4 and crystallizes in either trigonal, hexagonal, or cubic structure (labelled α, β, γ respectively). The hope is that these silicon nitride films will be easier to electrically stimulate. This is inspired by the lower bandgap of silicon nitride (compared to silicon oxide), and hence a smaller barrier at the silicon nitride-silicon nanocluster interface [24]. Other advantages include the possibility of visible-light PL tuneable over almost the entire visible range [25] and nanosecond decay constants (as opposed to tens of microseconds for silicon oxide based films).

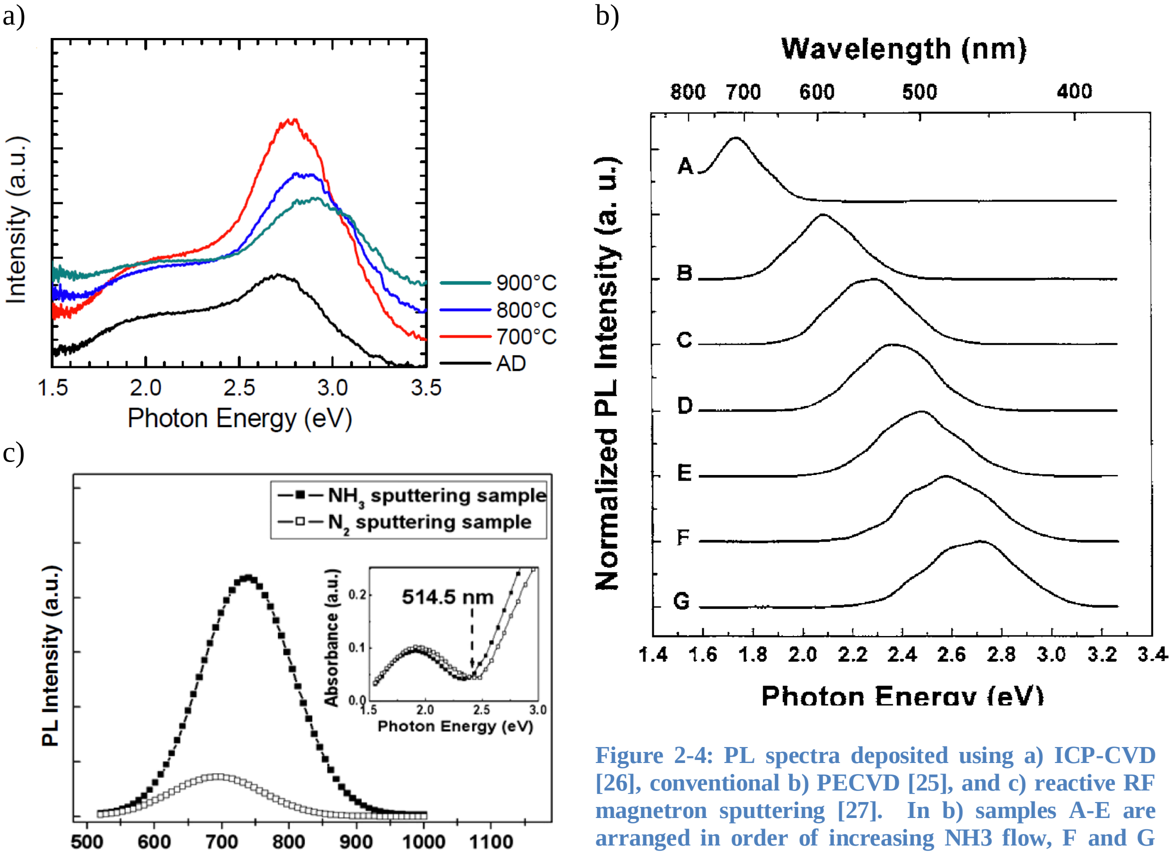

Figure 2-4: PL spectra deposited using a) ICP-CVD [26], conventional b) PECVD [25], and c) reactive RF magnetron sputtering [27]. In b) samples A-E are arranged in order of increasing NH3 flow, F and G are deposited at a lower deposition pressure with the higher nitrogen flow at G.

Examples of the PL of films grown on the McMaster ICP-CVD system are shown in Figure 2-4a [26], conventional PECVD in Figure 2-4b [25], and magnetron sputtering in Figure 2-4c [27]. In the ICP-CVD sample we see a large broad peak near 2eV and a narrower, yet more intense peak at 2.7eV. No detailed description of the origin of the PL signal was provided, though the importance of hydrogen passivation was noted. The fact that the maximum PL intensity is obtained at 700˚C as opposed to the 1200˚C found in oxides is a distinct advantage possessed by nitride based films. The PECVD spectrum also evidences separate peaks though they are not as clearly resolved as in the ICP-CVD spectra. The shift towards higher energies follows the increase in the flow of NH_3 and presumably increased nitrogen content. It is also interesting to note that depositing at a lower pressure results in a more heavily shifted signal that also exhibits more clearly defined features. In [25] the authors also contrast these results with some of their earlier work, using nitrogen as the source gas where they obtained weaker luminescence and amorphous clusters instead of nanocrystals. This point is made explicit, referring to Figure 2-4c, where the spectra appear to consist wholly of a single Gaussian peak, though the authors of [25] found a shift to higher energy with increasing ammonia flows.

It has been suggested that the lower mobility of silicon in silicon nitride promotes smaller cluster formation than is found in oxides. This could be at least a partial explanation for the higher energy luminescence from nitrides that is usually observed. The PL is also typically weaker than the luminescence from silicon oxide. One common reason for the reduced efficiency is the difficulty in obtaining nanocrystals as opposed to amorphous nanoclusters [28] since the more localized states in amorphous materials are less sensitive to the surrounding structure, be it quantum dot or bulk material. The less well-defined interfaces result in less well confined carriers and hence reduced efficiency.

Silicon nitride is commonly used within the microelectronics field, though it does not have the history of silicon dioxide in the field of luminescent silicon and is not nearly as well understood. In addition, the exact mechanisms involved in luminescence also remain uncertain. On the one hand we have quantum confinement effects, which have been used to explain the shifts in the PL and on the other we have a wide variety of potentially important defect states. Density functional theory (DFT) in the local density approximation (LDA) calculations of several different atomic structures showed that a nitrogen bridging bond at the nanocluster-matrix interface results in a reduced bandgap and a strong influence on the luminescent properties, rendering them less sensitive to the size of the nanocluster [24]. The seminal paper by Deshpande *et al.*, [29], used a suite of experimental techniques on hot filament chemical vapour deposition (HFCVD) grown films, including electron spin resonance, PL, EL, and photoluminescence excitation (PLE) to develop a defect based model for the PL that completely neglected quantum confinement effects. The authors were able to fit Gaussians to their PL spectra at 1.8, 2.5, and 3.0eV, and so assigned these energies to the Si^0, N_4^+, and N_2^0 defect levels (see Figure 2-5). The Si^0 defect is the Si-Si dangling bond defect, $N4^+$ fourfold coordinated N centre, and N_2^0 is a dangling bond associated with two bonded nitrogen atoms [30]. As noted in [29], there is a large degree of variation in the actual defect energies depending upon the composition and structure of the films. For instance, Gaussian fits to the PL spectrum in [28] yielded peaks at 1.54, 1.72, and 1.98eV for their PECVD grown samples. The importance of choosing the exciting laser wavelength for the PL is made clear in [31] where the PL spectra under 325nm He-Cd excitation are similar to those in Figure 2-4a, but 514nm Ar^+ radiation excited lower energy states that are typically associated with quantum confinement effects, like those in Figure 2-4c. Band tail states (states near the valence and conduction band edges within the bandgap) have also been identified as being important to the PL spectrum in a-Si_3N_4 [32].

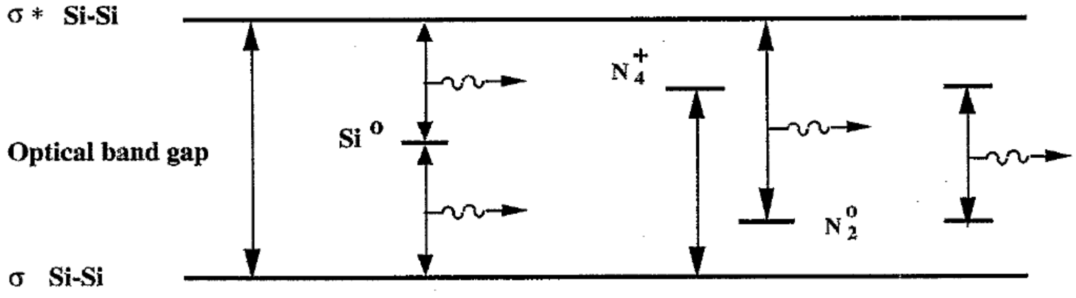

Figure 2-5: Defect levels in silicon nitride. PL activity has been ascribed to the transitions indicated [29].

EL devices have also been constructed. In [29], a metal insulator semiconductor (MIS) structure contacted with ITO and aluminum showed visible room temperature EL at a lower energy than the PL. The source of the luminescence may be quantum confinement related states that could not be excited with the Ar^+ laser that was used in the PL measurements. A different study involving a singly implanted sample actually showed a spectral shape that depended upon the injection current [33]. At low injection currents the spectrum was a light violet, becoming whiter as the current rose. This sample was singly implanted with a peak silicon concentration near the middle of the sample and very low excess silicon near the film-substrate interface. As the applied voltage was raised, the carriers were able to penetrate deeper into the film before recombining. Thus, higher energy luminescent sites associated with higher silicon excess became more important. In a different study however, multiply implanted silicon rich silicon nitride (SRSN) did not show this shift in the relative peak intensity, as can be seen in Figure 2-6 [34]. Figure 2-6 also shows that the EL can have a linear dependence on the current; this implies that this luminescence is primarily caused by electron and hole recombination. This is a good sign, although since there are only 4 data points one must temper one's exuberance. Other work has suggested various current mechanisms including: Frenkel-Poole [35], Fowler-Nordheim [36], and trap assisted tunnelling [36].

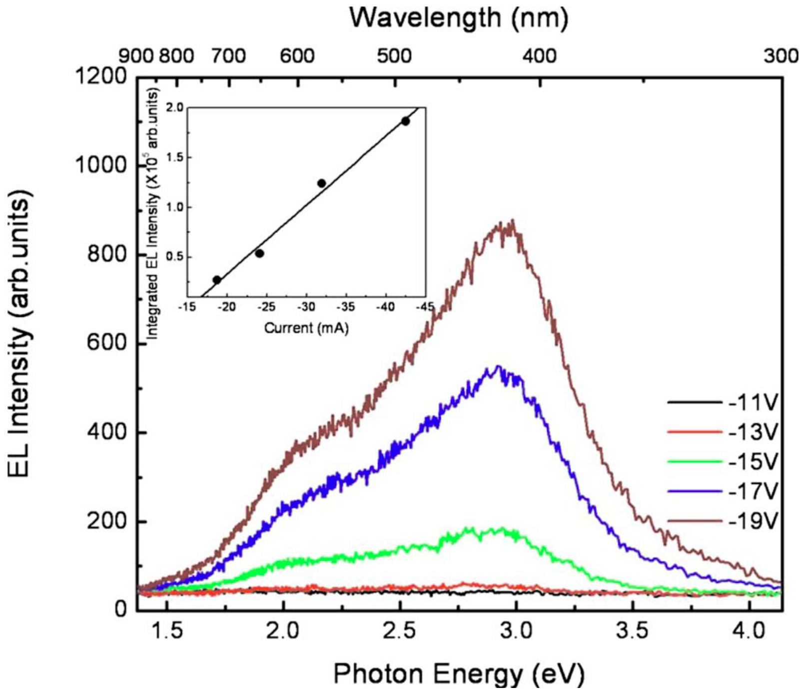

Figure 2-6: EL from multiply silcon implanted SRSN [34].

A possible source gas for depositing silicon oxide films by PECVD is N_2O, which means that some amount of nitrogen makes its way into the film. This silicon oxynitride is an intermediate case between silicon oxide and silicon nitride and is interesting as the increased compositional space permits a greater flexibility in tuning light emission characteristics.

The interest in silicon carbide stems from a different source as it has been studied extensively at a basic science level as well as for applications such as high power MOSFETS that make use of its excellent thermal stability. Crystalline silicon carbide exists in a huge variety of structural polytypes though here only the most common polytypes will be discussed, namely: the Zinc-Blende crystal structure, called β-SiC or 3C-SiC, as well as the simplest hexagonal structures 6H, 4H, and 2H. Several studies have calculated the band-structure of SiC, and we can see a sample of their results, from

[37], in Figure 2-7. The bandgap calculations show indirect bandgaps between 1.24 and 2.24eV depending on the calculation scheme used. This is a classic example of the systematic underestimation of the bandgap predicted by density functional

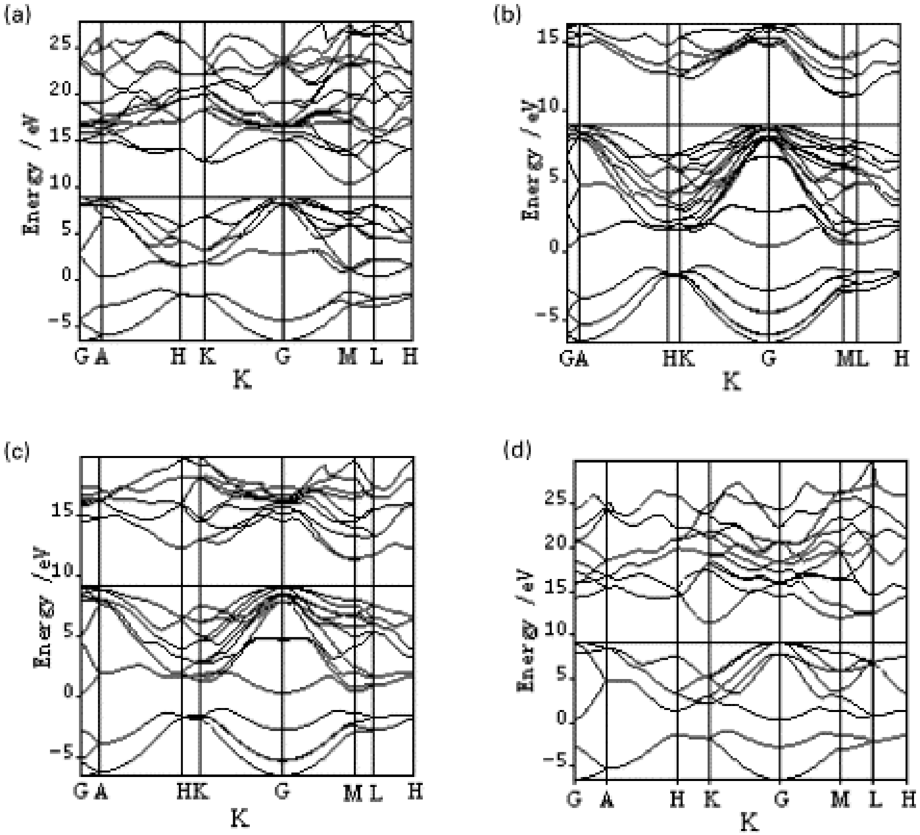

Figure 2-7: Density functional theory-local density approximation (DFT-LDA) band structure calculation for 3C (a), 6H (b), 4H (c), 2H (d) SiC polytypes [37].

theory (DFT). Experimental results for 3C-SiC and 6H-SiC give indirect bandgaps of 2.2 and 2.86 eV respectively, as well as a direct bandgap of 6.0eV for 3C-SiC [38]. However, crystalline silicon carbide is not suitable for integrated optics applications due to the necessity of high temperature deposition or processing, depending on the technique (temperatures in excess of 1000˚C are routinely encountered). Therefore, amorphous films seem to be the best candidate for consideration for an integrated silicon based light source. An additional feature of silicon carbide is that carbon can remain solid at room temperature which allows for the creation of carbon rich films, unlike oxides or nitrides where excess oxygen or nitrogen simply bond to one another and desorb into the gas phase. In the preparation of non-stoichiometric silicon carbide it is often found that SiC cluster formation occurs rather than silicon cluster formation. The PECVD film analysed in [39] consisted of a 4:1 silicon to carbon ratio, as well as large amounts of hydrogen, yet no evidence of silicon nanoclusters was obtained after high temperature annealing, though these authors, as well as others ([40], [41]), have found silicon nanocrystals forming in their films at lower Si to C ratios.

Examples of PL from silicon rich silicon carbide (SRSC) and carbon rich silicon carbide (CRSC) are shown in Figure 2-8a) and Figure 2-8b). The silicon rich film, which was deposited by PECVD, shows a large peak near 1.8eV, and a broad tail. Higher annealing temperatures resulted in a significantly enhanced PL signal that, in contrast to other materials, decreased after hydrogen passivation. The PL was associated with the presence of defect states related to the presence of SiC nanoclusters but not Si nanoclusters [39]. On the other hand, the carbon rich film showed a decrease in PL intensity, at 351nm Ar^+ excitation, with increasing annealing temperature after approximately 450˚C. The authors report that by 650˚C the PL signal has completely disappeared and attribute it to the formation of graphitic clusters. The initial increase in PL was attributed to a minor increase in the hydrogen passivation of dangling bonds and,

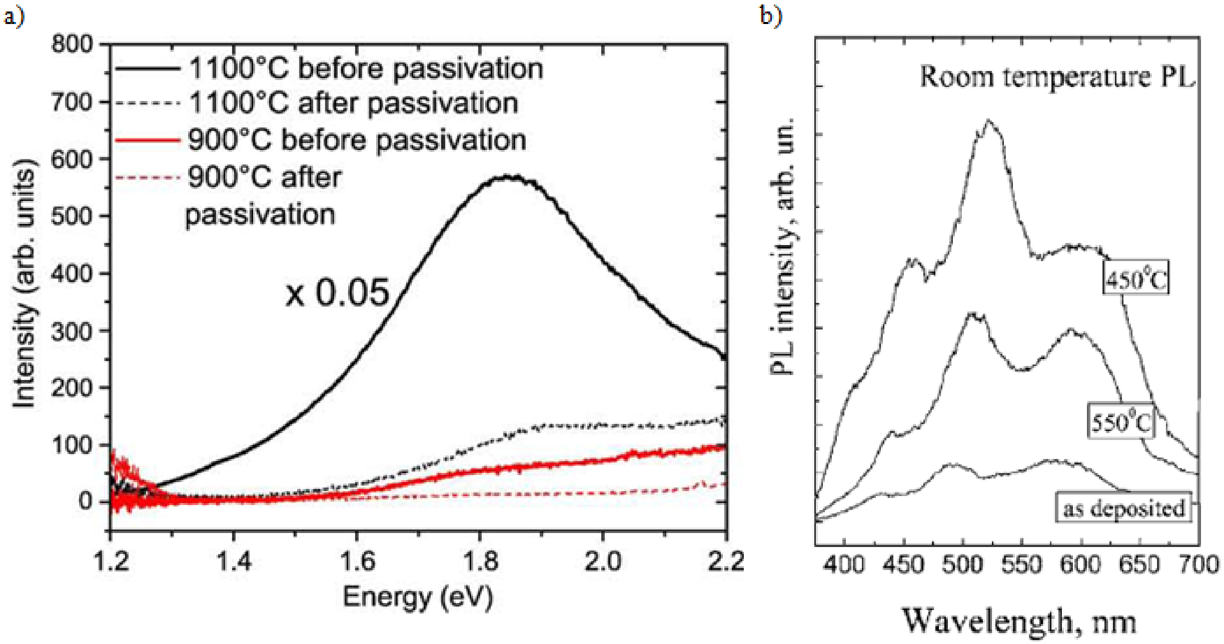

Figure 2-8: a) PL of a silicon rich PECVD SiC film after annealing both before and after hydrogen passivation in a dedicated remote plasma chamber [39]. b) PL of a carbon rich magnetron sputtered SiC film after annealing in vacuum [42].

as the dominant factor, replacement of carbon double bonds with a single bond and an additional bond to a hydrogen atom [42]. However, the authors in [42] also note that during their Raman experiments, with 514nm excitation, the PL background changed shape and intensity up to 850˚C, the highest annealing temperature used in the study. In this same paper, [42], the authors attributed the pronounced features in the PL spectra to interference effects, but they provide little explanation of the luminescence mechanisms involved. However, Li *et al.*, [41], performed a similar study on PECVD grown films and were able to assign wavelength values to fitted Gaussians of around 427, 500, and 580nm, though the values did shift significantly depending upon composition. Peaks were assigned to geminate recombination of electron-hole pairs and transitions between defect states based on a defect model developed using photothermal deflection spectroscopy (PDS) results [43], as well as theoretical calculations [44]. The theoretical calculations used 3 different types of defects: dangling bonds, five fold-coordination, and "anomalous" four fold coordinated atoms (atoms which were bonded to 3 or 5 fold coordinated atoms), and were able to produce optical absorption spectra which qualitatively match the experimental results very well. The differences are most likely caused by the neglect of hydrogen passivation leading to lower absorption coefficients in the PECVD films they considered [44]. PL decay constants in a-SiC_x:H are very fast (less than 1ns) and demonstrate a dependence on the wavelength of the emitted photon and tend to decrease with increasing carbon content [45], an effect which can be explained through broadening of the band tails and a multiple trapping model.

EL studies have been performed on thin films of silicon carbide deposited by the standard deposition processes, though the volume of published work seems small in comparison to the nitride and oxide based films. Typical devices made for EL measurements are MIS capacitors, and p-i-n diode structures, which produce spectra with multiple peaks associated with band tail states and defect states similar to those occurring in silicon nitride. An example of the EL signal, from [46], can be seen in Figure 2-9. This spectrum was obtained from a p-i-n diode consisting of front and back contacts of sputtered ITO, a boron-doped SRSC film, a luminescent layer of near stoichiometric a-SiC_x:H, and a layer of phosphorus-doped SRSC, all of which were deposited by PECVD. Though the main peak energies are in the NIR, other studies, for instance [47] which used xylene ($C_6H_4(CH_3)_2$) as a source gas for carbon in a PECVD process, have produced EL in the visible.

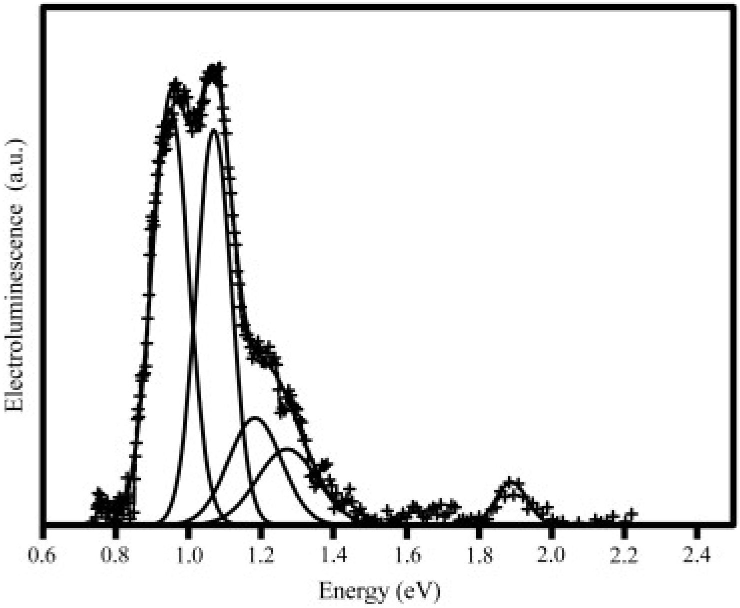

Figure 2-9: EL and Gaussian fits of an a-SiCx:H film [46].

Chapter 3 : Sample Manufacture

The thin films produced for analysis in this thesis were manufactured using an ICP-CVD system in the Tandem Accelerator Building at McMaster University. ICP-CVD is similar to the more common plasma enhanced chemical vapour deposition used routinely in vacuum coating industries with an additional specification on the generation of the plasma. CVD in general is a gas phase deposition technique where precursor gases are chemically dissociated, "cracked," to produce reactive species. The species then react either in the gas phase or in interaction with the substrate to produce a solid film. Deposition pressures are usually such that mean free path lengths are small. This means that turbulent flow occurs and the deposition process is conformal to the substrate. CVD is the standard thin film deposition technique in the semiconductor industry and is a common deposition technique in other industries, for instance some tribological coatings such as thin film diamond are deposited with CVD.

ICP-CVD

System

A schematic of the aforementioned ICP-CVD reactor is shown in Figure 3-1. The fundamental building blocks of the system are: the main chamber, where deposition occurs; the load lock, used to minimize the main chamber's exposure to atmosphere when loading the sample; the plasma chamber, where the electrical radio frequency (RF) power is coupled into the plasma gas; the vacuum system consisting of a series of pumps to ensure good vacuum; and the control system, responsible for ensuring suitable deposition

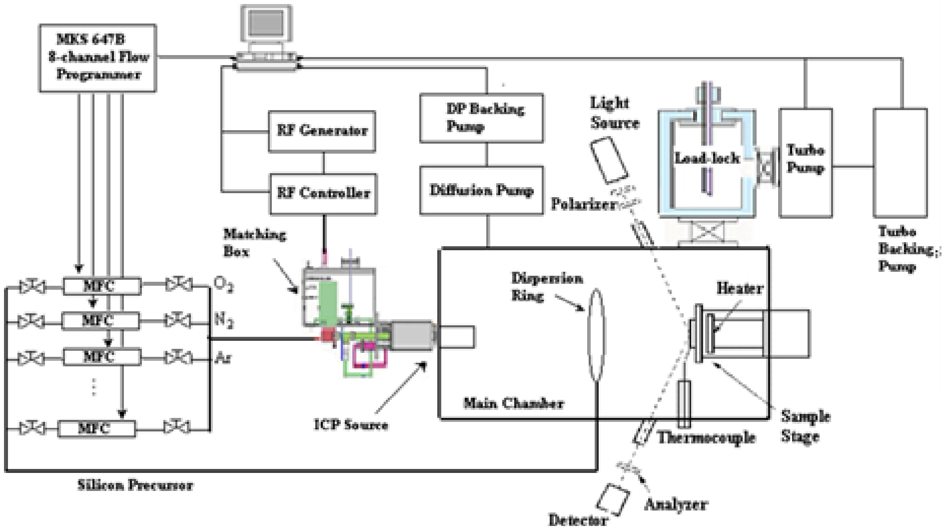

Figure 3-1: Schematic diagram of the ICP-CVD system [48].

parameters. The system is semi-automated with the various vacuum valves controlled through a computer driven control system, and optional recipe based deposition. Sample loading is a manual operation where the deposition substrate, silicon wafers up to 3” in diameter or fused silica substrates of comparable dimension, are clipped into a custom sample holder in the load lock. The load lock is roughed by a mechanical vane pump, which also serves to back the high vacuum turbo pump. The load lock is typically pumped to 5×10^{-6}Torr or better before the main gate valve between the load lock and main chamber is opened. The substrate is then transferred to the rotatable sample stage. The flow rates of the ultra high purity+ (UHP+) process gases are controlled through either the computer interface or through their dedicated controller, and the gases are flowed through either the plasma chamber or the dispersion ring.

The primary advantage of inductive coupling is the capability to form high density plasmas at low deposition pressures and plasma temperatures [48]. An additional advantage is the high efficiency demonstrated by modern plasma sources over more traditional capacitively coupled or DC plasmas. As well, when compared to sputtered films, evaporated films, HFCVD (where the precursors are broken down thermally) films, or films prepared by conventional hot plasmas, PECVD films tend to have less damage since energetic heavy particles do not impact the surface of the growing film as often.

Plasma Source

The plasma source in the ICP-CVD is a relatively simple device in concept and implementation. The source has the form of a helical current carrying conductor, i.e. a classic wire wound inductor with an air (or vacuum) core. A time-varying current in the conductor induces a magnetic field, and hence an electric field at the center of the inductor, and neglecting the effects of a finite length, the conductor gives the magnetic field (by a straightforward application of Ampere's Circuital law):

$$B = \mu_0 n i \tag{3-1}$$

where B is the magnetic flux intensity, n is the number of turns per unit length of the solenoid, and i is the current passing through the conductor,[1] and the electric field:

$$E(r) = \frac{-\omega \mu_0 n i}{2} r \tag{3-2}$$

---

[1] Actually, while this is the almost universally taught solution to the problem of an infinite solenoid it is in fact incorrect. The solution neglects the magnetic field created by the electric field. While in the low frequency limit the two are similar, at higher frequencies the two solutions are markedly different. The much more involved correct solution can be found in [49].

where ω is the angular frequency of the applied current, and r is the radial distance from the solenoid's axis. An inductively coupled plasma then begins to develop when the energy contained in the electric and magnetic fields is sufficient to ionize the plasma gas flowing through the solenoid's core:

$$U = \frac{\mu_0 n^2 i^2}{2} \tag{3-3}$$

The plasma evolves with increasing plasma power from a capacitively coupled E-discharge, to an inductively coupled H-discharge [50]. The E-mode has a much lower electron density (≈10^8-10^{10} /cm^3) than the H-mode (≈10^{10}-10^{12} /cm^3). This transition is clearly seen in practice when the plasma, which at low powers is small and not very bright suddenly grows larger and brighter. Following the discussion of [51] the transition is essentially caused by the magnetic field's greater ability to penetrate a conductor. At lower coil currents the majority of the ionization is caused by the electric field which is screened ever more strongly as the electron density in the plasma increases due to the decrease in skin depth. Eventually the skin depth effect dominates and prevents any significant increase in electron density. However, once the magnetic field grows large enough it too can ionize the gas species resulting in a steep rise in the electron density until, once again, skin effects become too large for the induced electric field to ionize gas atoms.

Other geometries for the generation of a plasma by induction are possible, notably the planar geometry where the spiral shape of the inductive coil is manufactured in a plane. It is most commonly encountered in the microelectronics field and is not part of the ICP-CVD. Thus, it and any other geometries will not be considered further.

Vacuum System

The load lock is serviced by two pumps. From atmosphere down to approximately 10^{-2} Torr a rotary vane pump is used. Below this pressure this mechanical vane pump serves as a backing pump for a small turbomolecular pump (a TMH 261) capable of reaching an ultimate pressure of approximately 10^{-6} Torr. The precise "ultimate" pressure depends on many factors, most relevantly the environmental temperature, the atmospheric humidity, the length of time the load lock was exposed to atmosphere during sample change, and the experimenter's patience. The operating principle of the mechanical vane pump, like all mechanical pumps, is that of volume displacement. In this case, the pump consists of an immobile cylindrical chamber, called the stator, with two ports. Inside the stator, a smaller diameter rotating cylinder is positioned off set from the stator centre so that it lies just touching the stator wall. Passing through the rotor is a pair of spring loaded "vanes" which extend and contract to follow the stator wall, drawing gas from the volume to be pumped, and compressing it to a higher pressure suitable for the backing pump to remove. The basic principle of the turbomolecular pump is to directly impart momentum to the gas molecules. The pump consists essentially of a high speed rotating turbine. The turbine blades are angled so as to "hit" the gas molecules towards the outlet pump (i.e. into the mechanical vane pump). A primary advantage of the turbomolecular pump is its wide range of operation. Though the one servicing the load lock pumps only to high vacuum levels, turbomolecular pumps exist which pump down to the ultra high vacuum range (lower than $3.8x10^{-10}$ Torr). The turbomolecular pump is also a “dry” pump, which means that no lubricating oil is present. This minimizes back contamination into the chamber and eliminates the possibility of waste process gases reacting with the oil, degrading the pump’s capability and lifetime. The main chamber is primarily pumped by an Edwards EO9K diffusion pump, capable of reaching an ultimate pressure of less than $3x10^{-8}$ Torr.

The pressure is monitored in both the load-lock and main chamber by a collection of gauges falling into two basic categories: capacitance manometers (i.e. Baratron) and ion gauges. The capacitance manometer is essentially a parallel plate capacitor where a flexible membrane is exposed to vacuum. The membrane flexes when the pressure in the chamber changes, resulting in a change in capacitance, which can be easily monitored. The operating principle of an ion gauge is to measure the conductivity of a gas, which decreases as the density of the gas becomes very small, i.e. in a high vacuum. This is done by heating a filament with an electrical current. The filament then emits electrons which are accelerated by a second electrode, the grid, before impacting on a detecting electrode called the collector. On the way to the collector the electrons can ionize gas molecules. The gas ions then form a positive current which prevents charge build up on the collector. This ion current is proportional to the gas density and is the measured quantity in the ion gauge.

In the usual operation of the ICP-CVD system only three potential parameters are varied intentionally to span the experimental space of interest: the plasma power, the substrate heater temperature, and the various gas flow rates which are used to make the desired film. The substrate heater temperature is much more easily controlled than the substrate surface temperature. In Figure 3-2 we see that changing the substrate heater temperature by 100˚C results in an increase at the sample surface of around 30˚C. The base operating pressure and the reflected power are simply optimized as best as the operator can before deposition proceeds. The deposition pressure is not controlled throughout the deposition as there is no relief valve contained in the pumping system. The position of the substrate within the chamber is maintained at the optimal value for uniform film distribution that was determined as part of H. Zhang's thesis project [48]. It is unlikely that for the gas flows used in this thesis this substrate position still results in the most uniform film being produced but this is not significant for the materials analysis.

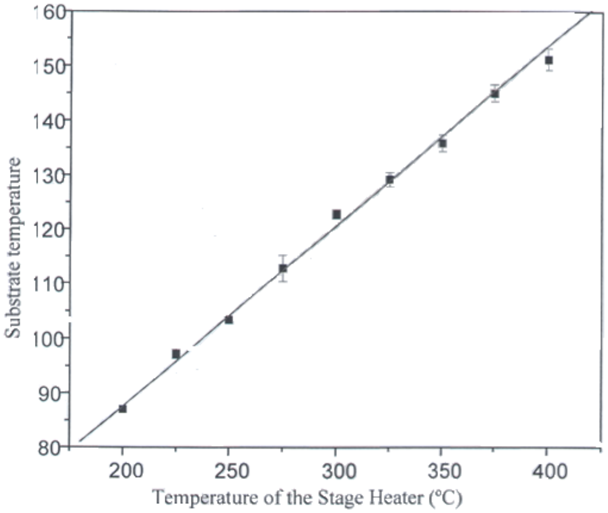

Figure 3-2: Variation of substrate surface temperature with stage heater temperature, as determined in [48].

Film Growth

In vapour based growth methods, evaporation, sputtering, CVD, pulsed laser deposition (PLD) etc., thin film growth occurs when an atomic or molecular species present in the gas phase impinges upon the substrate surface and bonds with it. If this bonding is through van der Waals forces then this is termed physisorption, and if a chemical bond is formed then this is termed chemisorption. The traditional materials science method for describing film growth involves applying thermodynamic rules. This theory is called capillarity theory and states that the essential cause of film growth is the minimization of the Gibbs free energy, defined as:

$$G(p,T) \ = H - TS \tag{3-4}$$

with H the enthalpy, T the temperature and S the entropy. Assuming as well an adatom impingement rate (number of adatoms per unit time, per unit area) of:

$$R = p\left(\frac{1}{2\pi m k_B T}\right)^{1/2} [s^{-1}m^{-2}] \tag{3-5}$$

with p equal to the pressure of the gas, m the mass of the incident atom or molecule, k_B the Boltzmann constant and T the temperature in Kelvins, one can derive an equation [52] for the minimum stable size of an island of growth,

$$r^* = \frac{-2\left(2\pi(1-\cos\theta)\gamma_{fv} + \pi\sin^2\theta\left(\gamma_{fs}-\gamma_{sv}\right)\right)}{\pi(2-3\cos\theta+\cos^3\theta)\Delta G_v} \tag{3-6}$$

with an associated change in Gibbs free energy

$$\Delta G^* = \frac{4\left(2\pi(1-\cos\theta)\gamma_{fv} + \pi\sin^2\theta\left(\gamma_{fs}-\gamma_{sv}\right)\right)^3}{3\left((2-3\cos\theta+\cos^3\theta)\Delta G_v\right)^2} \tag{3-7}$$

as well as the nucleation rate

$$\frac{dN}{dt} = 2\pi r^{*} a_0\, p \left(\frac{1}{2\pi mkT}\right)^{1/2} n_s e^{\left(\frac{E_{des} - E_s + \Delta G^{*}}{k_B T}\right)} \tag{3-8}$$

θ is the wetting angle, i.e., the interior angle between the film-substrate interface and the film-vacuum interface, γ_{fv}, γ_{fs}, γ_{sv}, are the strain energy per unit area of the film-vacuum, film-substrate, and substrate-vacuum interfaces respectively, a_0 is the characteristic dimension of the adatom, n_s is the total density of nucleation sites, E_{des} is the energy required for the adatom to desorb and E_s is the energy required for surface diffusion to occur.

This thesis is concerned with the growth of an amorphous film on a single crystal substrate. It is nonetheless useful to briefly review epitaxial film growth to provide a basis for comparison of a-SiC_xN_y:H. In epitaxial growth, and heavily depending upon the chemical system involved, 3 general modes of film growth are typically identified: layer-by-layer (i.e. Frank-van der Merwe), island growth (i.e. Volmer-Weber), and layer, then island growth (i.e. Stranski-Krastanov). So, layer by layer growth would occur when the Gibbs free energy associated with an additional adatom is minimized by completely covering the substrate surface prior to beginning the next layer of film material. Island growth occurs when the Gibbs free energy is minimized by minimizing the free surface area of the film material in preference to that of the substrate. Essentially, if the chemical potential energy well that the adatom falls into as film growth occurs is deeper for the substrate material than for the film material, layer-by-layer growth occurs whereas if the potential energy well is deeper for the film material, island growth occurs. Layer then island growth occurs when the existence of a strain field, which gradually builds up as the film thickens in heteroepitaxial growth causes the appearance of misfit dislocations, creating perturbations in the potential energy and inducing island growth. This is a simple model for the growth of crystalline films.

As a cluster (this happens in 3 dimensions as well as 2) grows via diffusion, the local area is depleted of the film species. When two clusters are nearby, the larger cluster has a lower concentration of free adatoms in its immediate vicinity [53]. This results in a concentration gradient of the given species pointing towards the smaller cluster and implying, according to Fick's First Law of Diffusion, $J = -D\frac{\partial c}{\partial x}$, diffusion towards the larger cluster. Due to kinetic constraints, namely that diffusive activation energies become large enough that over large distances diffusion becomes negligible, there is a non-zero steady state concentration of "free" adatoms that are not attached to any cluster. Thus atoms gradually dissociate themselves of the smaller cluster as the thermodynamically favoured configuration is that of a single large cluster (preferably crystalline in nature) and diffuse toward, and eventually becoming a part of the larger cluster. In more colloquial jargon the big clusters eat the little ones.

However there are several problems with the capillarity theory. It neglects the large potential energy barriers which can effectively prohibit structural reordering into a more thermodynamically stable structure, like the Ehrlich barrier [54], as well as the effects of adatom lifetime. One of the consequences of these factors is that true layer by layer growth can never actually occur. More relevant for this thesis is that purely thermodynamical considerations would forbid the formation of a truly amorphous film, such as those produced in this thesis. That said, there is some degree of applicability to the deposition of a-SiC_xN_y:H. *In situ,* real time monitoring of the growth of a sputtered CN_x film through ellipsometry has been correlated to the growth of a SiC interfacial layer and provides some evidence, albeit indirectly, for island then layer growth in that system [55]. Ultimately, no complete general understanding of film growth process has been developed with the ability to detail quantitatively the properties of a film.

To date there has been little analysis of the gas phase chemistry of SiC_xN_y:H produced from silane, methane and nitrogen gas, let alone complicated further by the presence of argon. One interesting study [56] used a solid source of carbon and inductive coupling of an RF field to excite nitrogen such that it would etch the carbon source for subsequent deposition onto a pair of silicon substrates to deposit a CN_x film. Using a quadrupole mass spectrometer the authors determined that the critical gas species for promoting growth was in fact the CN (possibly it was CN^+ as the mass spectrometer would not be able to distinguish between the two, though the geometry of their system makes this unlikely). Besling *et al* [57] used *in situ* mass spectrometry for a CO_2 laser based CVD process but did not see fit to publish their data and noted only the absence of oxygen contamination in their flow of ammonia. A detailed study using ion trap mass spectrometry and gas precursors of silane, ammonia, and propyne identified a large number of potential products with $Si_2H_4^+$/$SiCNH_6^+$, $Si_3H_6^+$, and $SiC_4NH_{10}^+$, composing the largest fraction of species, any of which could easily be produced in a silane, methane, nitrogen system [58]. In contrast, the most important precursor species for silicon nitride are SiH_3^+ and activated nitrogen N_2*[59]. As well, in the deposition of silicon nitride, hydrogen preferentially bonds to the nitrogen as opposed to the silicon

[59]. This was determined using *in situ* Fourier transform infrared (FTIR) spectroscopy in what is in effect an ICP-CVD reactor, where the nitrogen serves as the plasma gas. The same study found that film growth occurs via nitridation of an amorphous silicon layer and that as the growth occurs the silicon layer maintains its position at the surface of the film [59].

Annealing

After deposition the samples were cleaved into smaller pieces and annealed at various temperatures between 300 and 1200˚C in a tube furnace. The tube furnace consists of a proportional-integral-differential (PID) controller, the quartz tube, thermally insulating bricks with heater wires embedded in them, an external gas source to provide a flowing ambient atmosphere, and a “boat.” The boat is actually an annealed test tube which has been chopped in half then subsequently welded to a glass rod for positioning. When annealing at 1200˚C, the boat, which is primarily made of silica, actually evaporates slightly over the hour long anneals performed in this thesis. Initially this contaminant source was considered as a possible explanation for the reduced luminescence at higher annealing temperatures; however, the FTIR analysis confirms that it is only at 1200˚C that the evaporated silica is present.

The purpose of post-deposition annealing is to promote atomic diffusion and hence cluster formation. The formation of new structures occurs for the same ultimate reason that film growth occurs, to minimize the Gibbs free energy. The qualitative justification is that at higher temperatures, the atoms have higher average kinetic energy. This is simply restating the definition of temperature. Therefore, there is less of a difference between the atom's energy and the potential well in which it lies, meaning that the chance that a given atom will "break" its bonds and move to a new location with a new potential energy well has increased. The atom has then "diffused" to a new location, where it will remain until it gains enough energy to escape to a new, deeper well or until the temperature is lowered. Since the crystalline forms are the minimum energy forms for a given material it would be expected that film structures closer to that of a fully crystalline nature would be approached as either time or annealing temperature increases.

Silicon Carbon Nitride

Silicon nitride and silicon carbon nitride are both used as diffusion barriers in microelectronic applications between the copper interconnect lines and the low k dielectric medium in which the interconnects are embedded. Silicon carbide is used in a myriad of different industries including as a hard coating for wear reduction applications, as the active semiconductor in power electronics, as a thermal conductor for heat sink applications, and as a gemstone simulant for diamond. Formation of a-SiC_xN_y:H occurs from the base structure of α-Si_3N_4 by progressively replacing the silicon atoms with carbon. The electronic band structure of crystalline silicon carbon nitride has been simulated using a generalized density functional theory (GDFT) approach in the local density approximation (LDA) as shown in Figure 3-3 [60]. GDFT is used to help reduce the systematic over estimation of the bandgap energy. The crystal structure's bandgap progressively shrinks as carbon replaces silicon with direct bandgaps of 5.07, 3.82, 3.60eV, and indirect bandgaps of 5.05, 3.81, 3.58eV for α-Si_3N_4, α-Si_2CN_4, α-SiC_2N_4, respectively. In all the cases which contain silicon the band-gap is almost perfectly direct,

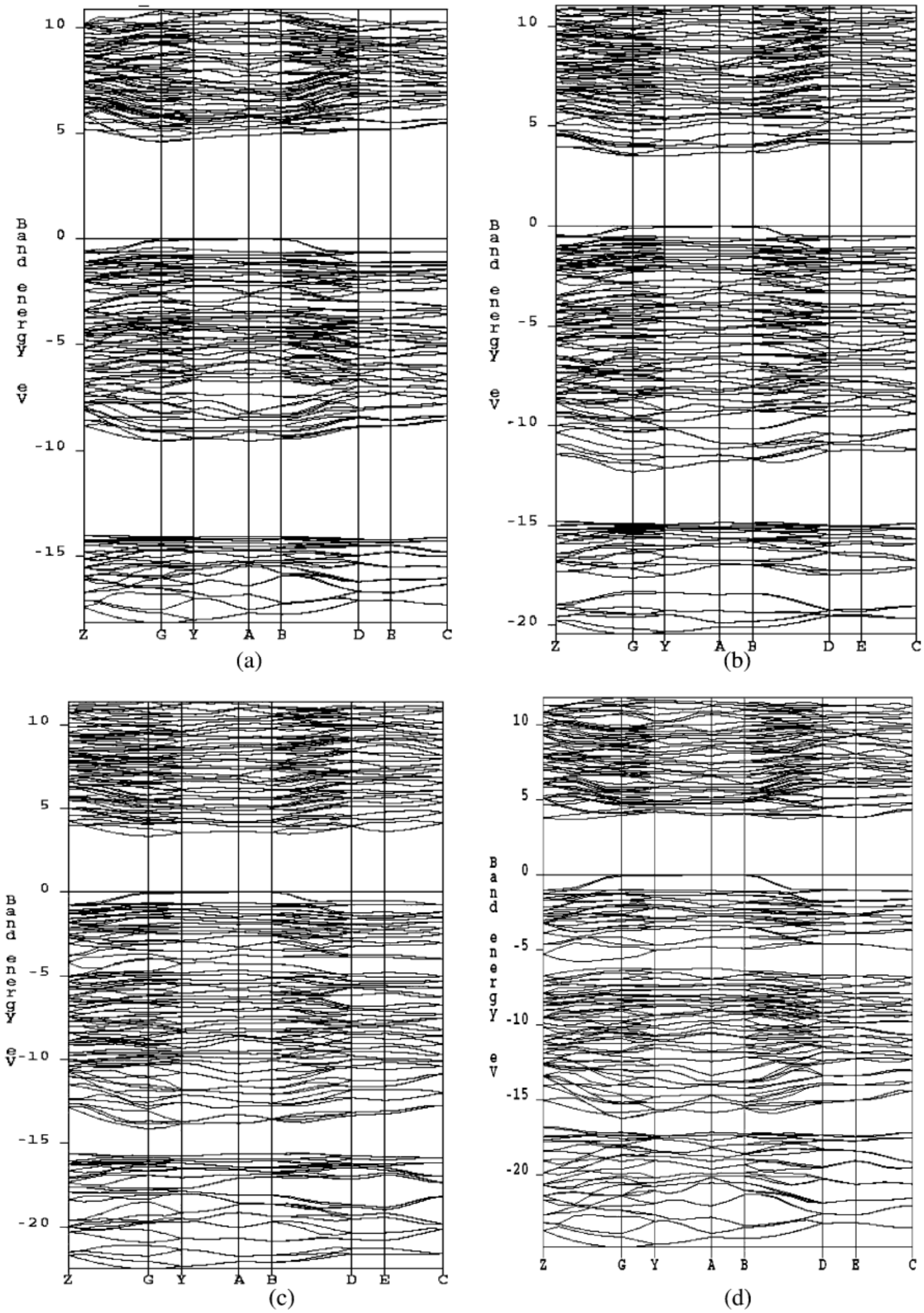

Figure 3-3: GDFT-LDA electronic band structures for crystalline a) α-Si_3N_4, b) α-Si_2CN_4, c) α-SiC_2N_4, and d) α-C_3N_4 [60]. Energies are measured relative to the top of the valence band.

whereas for α-C_3N_4 the indirect bandgap is 3.97eV and the direct one is 4.24eV. So it can be interpreted that the electronic structure of silicon carbon nitrides more closely approximates that of silicon nitride than carbon nitride. This is not surprising since α-Si_3N_4 was used as the base for constructing the other materials.

The structure of amorphous silicon carbon nitride materials has been simulated through classical [61] and DFT [62] based molecular dynamics. Comparison with thermodynamic phase diagrams could not be performed as there seems to be no published phase diagram that covers the low temperature region that we are concerned with in this thesis. Both of the simulation studies predict the formation of a heterogeneous mixture of phases. The more wide ranging classical study predicts the formation of a variety of phases depending on the composition. The general tendencies that the authors note in their conclusion are for silicon to attempt to coordinate entirely with nitrogen leaving carbon to form trigonal structures with more carbon (i.e. graphite) or excess silicon. Unfortunately, it was thought that the high annealing temperatures used in this study prohibited the existence of C-N bonds and bonding of this type was neglected. N-N bonding was also neglected-since nitrogen is a gas at room temperature and can diffuse out, this is not likely important. X-ray and neutron scattering experiments on a sample made by pyrolysis of a polysilylcarbodiimide polymer [63], then subsequently analyzed through reverse Monte Carlo simulations produced pair correlation features consistent with this theme of phase separation.

The initial impetus for the development of crystalline SiC_xN_y, was the prediction by Liu and Cohen [64] that C_3N_4 would have a bulk modulus comparable to that of diamond. However, difficulties in producing crystals of C_3N_4 were encountered that could be alleviated by the introduction of silicon. Production of both amorphous SiC_xN_y and crystalline SiC_xN_y has been reported in the literature. Some of the first crystalline structures were produced in [65] through the reaction of $SiCl_4$ and (trimethylsilyl)carbodiimide. Chen et al [66] used microwave PECVD (MWCVD) to produce well faceted hexagonal SiC_xN_y microcrystalline films that vary considerably in composition. The observed film morphologies range from highly non-uniform films with low surface coverage, to smooth, amorphous and nanocrystalline films [67], to large well faceted crystallites [66] to more complex structures like rough columnar structures [68]. Figure 3-4 clearly shows the large variation in crystal sizes that can be obtained.

There have been several works published which examine the PL properties of SiC_xN_y films but there is little consistency between the measured results. Early results from the microcrystalline film produced in [66] indicate a single sharp peak at approximately 380nm, which was attributed to the material bandgap (determined by photothermal deflection spectroscopy, PDS), and a large broad peak at around 440nm attributed to intersubband transitions caused by defects. Recent work, [69], has involved the doping of terbium into a RF magnetron sputtered film, followed by annealing in a carbothermal atmosphere. The authors measured PL peaks near 380nm and 424nm (resolved by Gaussian fitting) which they attributed to the effect of oxygen from the interface and surface oxygen defect states respectively. a-SiC_xN_y:H samples generated through ion implantation of C^+ ions and then subsequently annealed exhibit a more

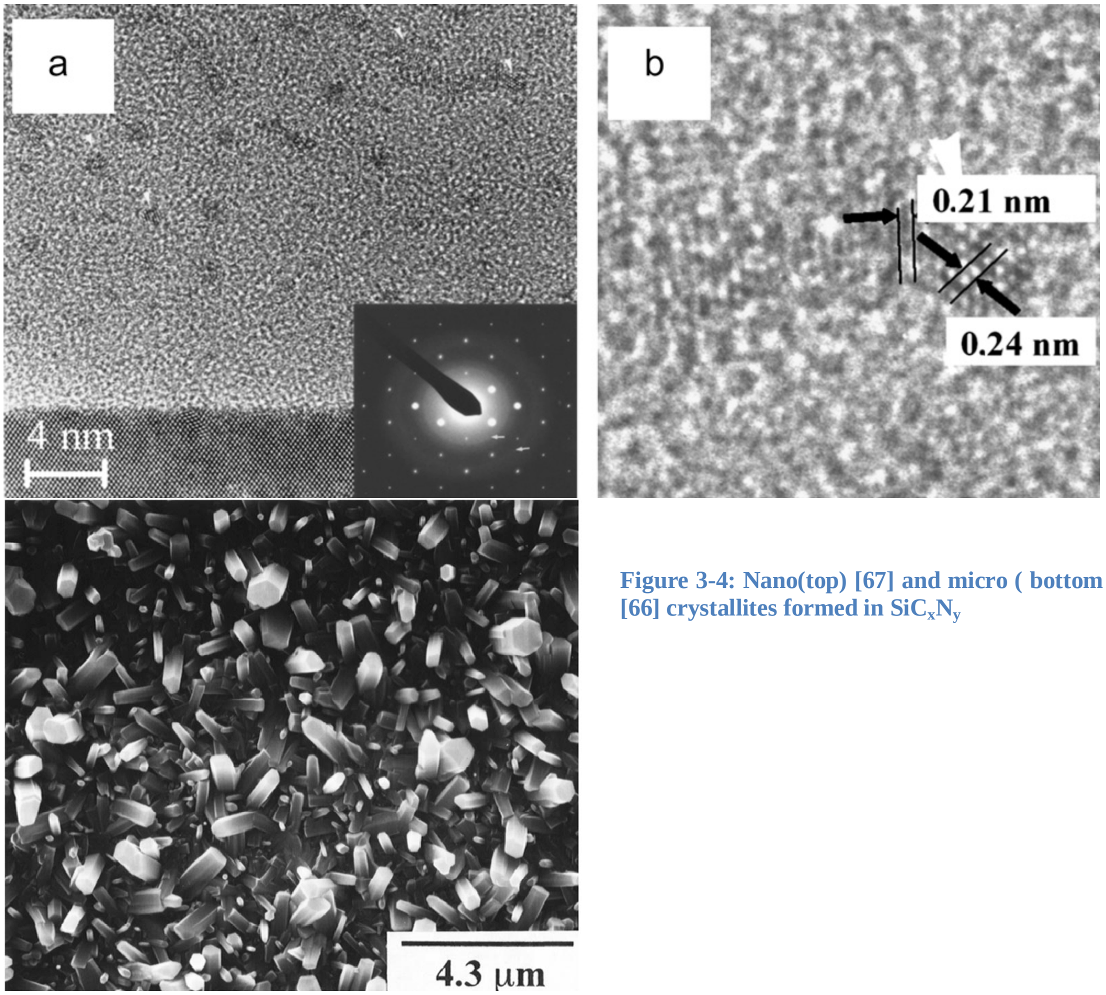

Figure 3-4: Nano(top) [67] and micro (bottom left) [66] crystallites formed in SiC_xN_y

complex PL structure (Figure 3-5), at least partly due to the authors' choice of cooling the samples in air after annealing [70]. The authors fit 4 Gaussian curves at wavelengths 420, 480, 541, 584nm and related them to structures composed of SiN_x, SiC_xN_y, SiC, and SiO_x respectively, with the peak at 584nm shifting, according to their fitting procedure, to longer wavelengths when the annealing temperature was increased to 1200˚C [70]. EL has been observed from a:SiC_xN_y from an RF sputtered film sandwiched between an ITO film deposited on glass, and an aluminum top contact [71]. Again the broad band radiation that results can be decomposed into two peaks, though both occur at longer wavelengths in this study [71].

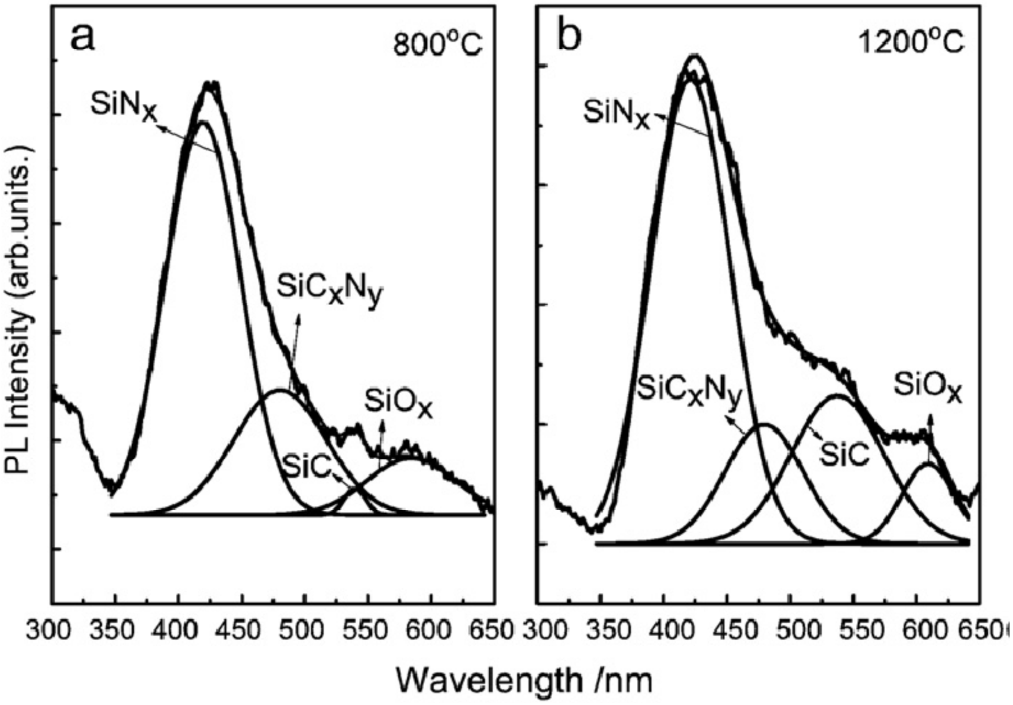

Figure 3-5: Typical PL spectra obtained from a:SiC$_x$N$_y$. Gaussian curve fits represent one possible assignment of luminescent activity [70].

Only a couple of studies have attempted spectroscopic ellipsometry to determine the complex refractive index/dielectric function of SiC$_x$N$_y$ films [72], [73]. However, there is a great deal of similarity between the index of refraction of SiC$_x$N$_y$ and those of silicon carbide and silicon nitride films. In Figure **3-6** the index of refraction of a SiC$_x$N$_y$ film produced using ion beam sputtering from a mixed adenine-silicon target is seen to increase from around 1.7 to over 2.4 at 632.8nm as the silicon content of the film increases, with the most rapid change occurring when the silicon content increased to around 30 at.% [73].

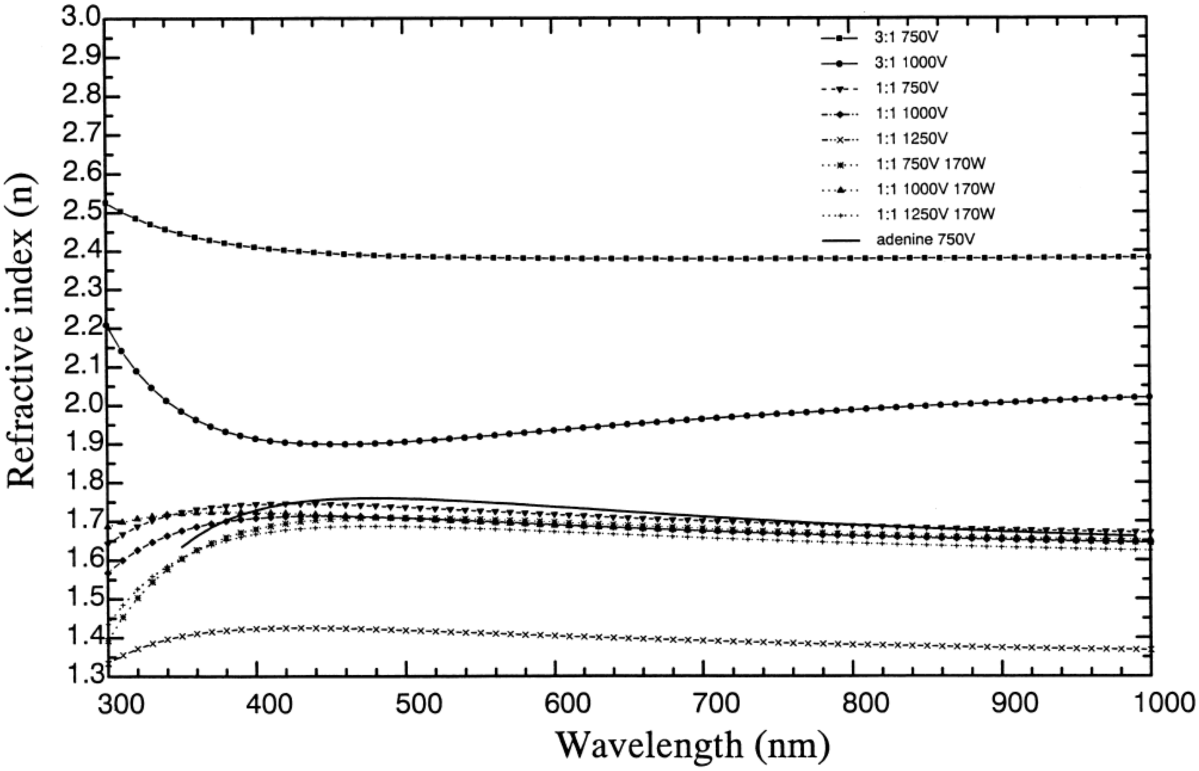

Figure 3-6: Complex refractive indices of ion beam sputtered SiC_xN_y thin films. Note the anomalous dispersion at the longer wavelengths in the top two curves [73]. The films are identified by the ratio of the sputtering target's area (silicon:adenine) and the sputtering voltage.

Chapter 4 : Analysis Techniques

As the essential effort in this thesis revolves around the characterization of thin SiC_xN_y films, an introduction to the techniques used to characterize them is merited. The order of the techniques presented is determined by logical progression and is not indicative of the order in which the measurements are performed. Chronologically, the first experiment performed on a sample is a measurement of the PL. The composition of our films was then determined by RBS and ERD measurements , followed by ellipsometric measurements. Finally, for some select samples, one or more of UV-Vis transmission, time dependent photoluminescence, XAS, TEM, and finally EELS measurements were performed.

Rutherford Backscattering and Elastic Recoil Detection

Rutherford backscattering spectrometry (RBS) and elastic recoil detection (ERD) are a pair of related and complementary ion beam techniques used, in this thesis, for routine determination of the elemental compositions of various samples. It is typically the starting point for any interpretation of results. The basic premise is to direct a high energy ion beam (typically 1-2MeV He^+) and to detect the energies of the scattered particles. For the work in this thesis all RBS and ERD experiments were carried out at the University of Western Ontario's Tandetron Accelerator Laboratory. The dominant feature of this lab is the namesake tandem accelerator and the several connected beam lines/endstations. Details of the operation of the accelerator are not necessary for comprehension of either RBS or ERD and thus will not be given. The primary feature of interest relating to the accelerator is the width of the energy distribution of the beam.

Under ideal circumstances (for these measurements) the beam would be purely monochromatic, which is to say all particles in the beam would possess the same energy. Unfortunately, this is not the case, so an effect referred to as energy “straggling” must be accounted for when interpreting the results of such experiments. The software program SIMNRA, [74], was used for the numerical analysis of all RBS and ERD spectra presented in this thesis.

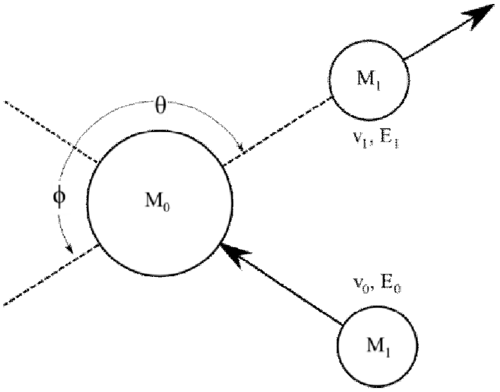

Figure 4-1: Classical scattering scenario encountered in RBS and ERD.

The physical argument makes use of classical interpretations of position, momentum, and energy, as the progression here follows the development present in the SIMNRA manual [75]. Consider two particles, of masses M_0 and M_1 involved in a collision, as in Figure 4-1 (where we take M_0 as our frame of reference, or by assuming M_0 stationary in the laboratory frame of reference, i.e., motionless with respect to the experimental apparatus). By applying the principles of conservation of energy and momentum, and after performing some algebra we arrive at the formula for the kinematic factor:

$$K = {}^{E_1}\!/_{E_0} = \frac{{M_1}^2}{(M_1 + M_0)}\left\{\cos\theta \pm \left[\left(\frac{M_0}{M_1}\right)^2 - \sin^2\theta\right]^{\frac{1}{2}}\right\}^2 \tag{4-1}$$

The positive sign applies when $M_1 < M_0$ and is the scenario encountered in RBS measurements. If $M_1 > M_0$ then both positive and negative signs apply since paths which pass the scattering centre at different distances (called the scattering distance or the scattering parameter) can both scatter at the same angle. It should be noted that for $M_1 < M_0$ only back scattering of the incident particles is permitted. Since the nuclei are positively charged they interact coulombically, exerting an electrostatic force on each other

$$F_E = \frac{{q_e}^2 Z_1 Z_2}{4\pi\varepsilon_0 r^2} \tag{4-2}$$

and therefore undergo (approximately) Rutherford scattering. The probability is provided by the famous Rutherford differential scattering cross-section, which gives the probability that a particle originating in a ring of width $d\sigma$ will scatter off the scattering center (atom), and pass through a differential solid angle ring, of width $d\Omega$, lying within the collection angle of the detector:

$$\frac{d\sigma}{d\Omega} = \frac{\left(\frac{Z_1 Z_2 {q_e}^2}{4\pi\varepsilon_0}\right)^2}{16E^2\sin^4 {}^{\theta}\!/_{2}} \frac{\left[\left({M_0}^2 - {M_1}^2\sin^2\theta\right)^{1/2} + M_0\cos\theta\right]}{M_0\left({M_0}^2 - {M_1}^2\sin^2\theta\right)^{1/2}} \tag{4-3}$$

While I have for the most part used Rutherford cross-sections to simulate the scattering from the films it should be noted that at high energies the nuclear force can influence the results. However, our experiments were conducted at 2MeV, which is below the region where nuclear effects can begin to become important (except for hydrogen but this is not detected anyway).

When considering a material rather than an isolated particle, the total number of detected particles ("counts") from a region of the sample of thickness dx is given by:

$$\mathrm{Q} = \frac{N\Omega_D}{\cos\alpha}\int_{x_1}^{x_2}\frac{d\sigma\big(E(x)\big)}{d\Omega}dx \tag{4-4}$$

where N is the number of incident particles, Ω_D is the solid angle of the detector, and α is the angle of incidence of the beam onto the sample. N is termed the "dose" and is usually measured in microcoulombs of charge using an ammeter and then converted into number of particles. When the incident particles do not scatter immediately at a high angle they begin to penetrate deeper into the material, losing energy as they travel due to electron drag and to a lesser extent nuclear drag. Electron drag is caused by the progressive ionization of atoms as the incident particle travels whereas nuclear drag is caused by the displacement of atoms (i.e. beam damage). The loss of energy per distance traveled through the sample is termed the stopping power of the material and is determined by the mass of the atom, the electronic distribution and the structure of the solid. We assume a constant stopping power, $S = \frac{dE}{dx}$, so we can reformulate the above formula into

$$\mathrm{Q} = \frac{N\Omega_D}{\cos\alpha}\frac{1}{S}\int_{E_1}^{E_2}\sigma(E)dE \tag{4-5}$$

which is the formula used within SIMNRA to calculate the number of counts.

Within SIMNRA, there are several different methods of determining the stopping power, however, in this thesis only the Ziegler-Biersack method is used; this is an empirically based formula. At the energies used nuclear stopping is unimportant, and while it is included in the simulations the details of the calculations will not be given here. The interested reader is referred to the SIMNRA manual or references [76], [77]. The electronic stopping power for a proton S_{ep} is given by

$$S_{ep} = \frac{\left(C_1E^{C_2} + C_3E^{C_4}\right)\left(\frac{C_5}{E^{C_6}}\ln\left(\frac{C_7}{E} + C_8E\right)\right)}{\left(C_1E^{C_2} + C_3E^{C_4}\right) + \left(\frac{C_5}{E^{C_6}}\ln\left(\frac{C_7}{E} + C_8E\right)\right)} \tag{4-6}$$

For helium the Ziegler-Biersack electronic stopping power S_{eHe}, is

$$S_{eHe} = S_{ep}(Z_{He}\gamma_{He})^2 = S_{ep}{Z_{He}}^2\left(1 - e^{-\sum_{i=0}^{5} C_iE^i}\right) \tag{4-7}$$

In both of these formulas the coefficients C_i are fitting parameters and are found in tabulated form in [77].

Elastic recoil detection is the complementary technique to RBS. Here, instead of measuring the backscattered atoms from the beam, forward scattered “recoils” are detected. They are collected in the same manner as the backscattered particles and one possible source of error is that hydrogen recoils could be detected as helium backscatters. The energy of these recoil particles can be calculated, again using the conservation of energy and momentum, as:

$$E_2 = E_0 4\frac{M_1M_2}{(M_1 + M_2)^2}\cos^2\theta \tag{4-8}$$

There are other effects which SIMNRA takes into account, or at least makes an approximation for, that are beyond the scope of this thesis. The two most important of these are nuclear reactions that can occur at the high energies used for RBS and ERD, and energy straggling. Nuclear reactions can occur at various energies depending on the reactant products. Energy straggling refers to the various mechanisms that broaden the distribution of energies of the beam. The relevant effects that are accounted for within SIMNRA are electronic energy loss straggling due to statistical fluctuations (nuclear loss is insignificant), geometrical straggling caused by the finite solid angle of the detector and non-zero size of the beam, multiple small angle scattering, and straggling due to surface roughness and thickness inhomogeneities.

Fourier Transform Infrared Spectroscopy

The absorption profile of a sample in the infrared portion of the electromagnetic spectrum is a powerful technique for probing the vibrational characteristics of the various species, and thus, is an indirect probe of the structure. In traditional infrared spectroscopy a thermally generated, possibly polarized, beam of light is passed first through a monochromator, to produce a monochromatic beam, then through the sample, into a detector. The wavelength of the beam is varied by the monochromator and the intensity of the transmitted beam is recorded as a function of wavelength. For a fairly high (though not exceptional) resolution of 2 cm^{-1} (1 cm^{-1} is said to be “1 wavenumber” and is equal to the reciprocal of wavelength) for example, this results in a large number of measurements and hence extremely long experiment times. FTIR alleviates this by measuring the entire spectral range simultaneously, called “Fellgett’s advantage,” and increases the light intensity at each measurement point [78]. This is possible by replacing the relatively simple grating monochromator with an interferometer. See Figure 4-2 for an example of the Michelson type. In this interferometer a light source generates a broad spectrum of collimated radiation and illuminates a 50/50 beam splitter. Half of the light is reflected onto a fixed position mirror whereas the other half is transmitted to a mirror which travels along the light's direction of propagation during the measurement. This movable mirror can introduce an optical path difference (OPD) $\delta \overset{\text{def}}{=} 2(M - F)$, which results in constructive and destructive interference when the beams recombine after returning to the beam splitter. Finally the beam passes through the sample to the detector. It should be noted that a beam returns to the light source and, though not shown, that there will in general also be a reflected component from the sample.

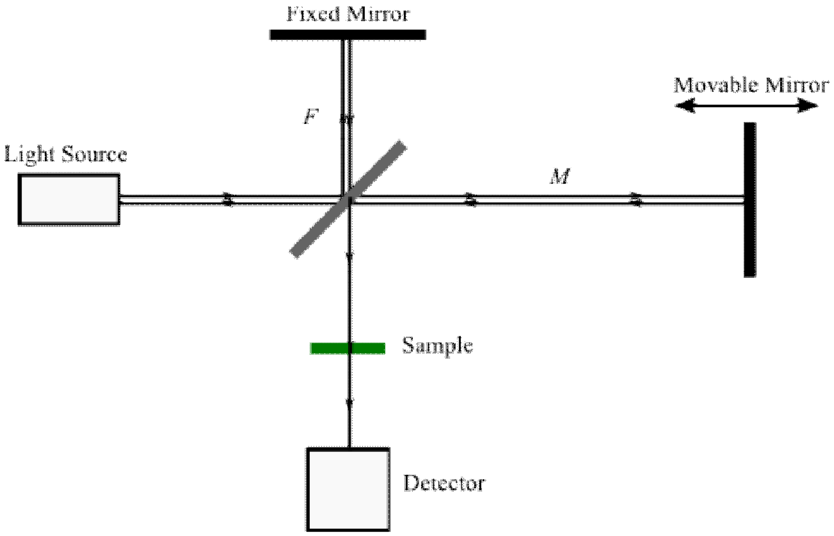

Figure 4-2: Schematic of the experimental setup of a typical Michelson interferometer used in FTIR.

When there is no sample present, the intensity measured at the detector is a function of the optical path difference and the source. In this scenario, whenever $\delta = n\lambda$, where λ is the wavelength of the light and n is an integer, there will be a maximum in intensity at that wavelength equal to that of the source intensity (due to the shifts in phase occurring at the mirror and beam splitter interfaces). When $\delta = n\lambda/2$ the two beams are perfectly out of phase and complete destructive interference occurs, with all light being reflected back into the source. So, the intensity measured at the detector, I_D, as a function of the optical path difference is:

$$I_D(\delta) = \int_{\lambda} {}^{1}\!/_{2}\, I_S(\lambda)\left[1 + \cos\left(2\pi\frac{\delta}{\lambda}\right)\right] d\lambda \tag{4-9}$$

which is simply half the total source intensity added to the Fourier cosine series of δ. Neglecting the initial source intensity we get the interferogram

$$I(\delta) = \int_{-\infty}^{\infty} {}^{1}\!/_{2}\, I_S(\lambda)\cos\left(2\pi\frac{\delta}{\lambda}\right) d\lambda \tag{4-10}$$

So far we have neglected some wavelength dependent factors which can modulate the intensity of the detected field, including instrumental factors such as the efficiencies of the beamsplitter and mirrors, or the detection efficiency of the detector, and most critically the role of the sample. The instrumental factors do not change from measurement to measurement and so can be combined into a single factor, $B(\lambda)$, but the sample does change, and must be accounted for with its own factor, $A(\lambda)$.

$$I(\delta) = \int_{-\infty}^{\infty} {}^{1}\!/_{2}\, I_S(\lambda)B(\lambda)A(\lambda)\cos\left(2\pi\frac{\delta}{\lambda}\right) d\lambda \tag{4-11}$$

So, the only unknown in this equation is the sample factor. δ is varied, $I(\delta)$ is measured and both the source and instrumental terms are constant between measurements. Thus we can take the inverse Fourier cosine transform to obtain

$$A(\lambda) = \frac{1}{2I_S(\lambda)B(\lambda)}\int_{-\infty}^{\infty} I(\delta)\cos\left(2\pi\frac{\delta}{\lambda}\right) d\delta \tag{4-12}$$

the transmissivity of the sample, that which was desired. The transmissivity alone is not sufficient to calculate the absorption or reflectivity since one cannot distinguish between the two with just this setup. While the simple transmittance measurement is the standard measurement there are many other variations and techniques that can be used including recovering the reflected spectrum from the sample. While the details of these techniques, specular reflection, attenuated total reflection, microspectroscopy, IR imaging, photoacoustic spectrometry, will not be given here, the interested reader is referred to the excellent review of FTIR techniques by Griffith [78].

At this time it is appropriate to describe the physics, at least in a rough approximate sense, of the light-matter interaction. The light will be treated as a classic electromagnetic wave, since the atomic dimensions are so much smaller than the wavelength of ultraviolet, visible, and infra-red radiation (hence we can also ignore the spatial variation of the field), but the material properties will be treated, in a simple manner, quantum mechanically. I reproduce here the development found in Chapter 2 of the Handbook of Ellipsometry [79], which is itself a compressed version of the explicitly detailed development found in [80]. The starting point is a single atom weakly interacting with its neighbours. The (time independent) Schrödinger equation is then

$$H_0\varphi_n = E_n\varphi_n \tag{4-13}$$

where H_0 is the steady state Hamiltonian, and E_n is the energy of eigenstate φ_n. The incident electromagnetic wave has an electric field vector chosen to be directed along the x direction and with a maximum at the origin.

$$\vec{\mathcal{E}} = \left[\mathcal{E}_0\left(e^{+i\omega t} + e^{-i\omega t}\right)\hat{x}\right] \tag{4-14}$$

It can be written as a time dependent perturbation to the Hamiltonian, $H^{'}(t)$, within the time dependent Schrödinger equation

$$i\hbar\frac{\partial\Psi}{\partial t} = \left(H_0 + H^{'}(t)\right)\Psi \tag{4-15}$$

which has solutions as

$$\Psi = \sum_n a_n(t)\,\varphi_n e^{-i\frac{E_n t}{\hbar}} \tag{4-16}$$

where $a_n(t)$ is the probability that a measurement of the energy at time *t* would return the energy E_n, placing the atom into state φ_n. This is the same as the time independent, unperturbed situation except the probability amplitudes, $a_n(t)$, are now a function of time. With the wave excitation above defining $H^{'}(t)$

$$H^{'}(t) = \frac{q_e\mathcal{E}_0 x}{2}e^{\gamma t}\left(e^{+i\omega t} + e^{-i\omega t}\right) \tag{4-17}$$

γ is the decay time of the transition, and q_e is the magnitude of the electron charge. From the above one can calculate the probability amplitudes as

$$a_n(t) = \frac{q_e\mathcal{E}_0 x_{n0}}{2\hbar}\left(\frac{e^{i(\omega_{n0}-\omega)t}}{\omega_{n0} - \omega - i\gamma} + \frac{e^{i(\omega_{n0}-\omega)t}}{\omega_{n0} + \omega - i\gamma}\right), x_{n0} = \int_V \varphi_n{}^{*}\vec{x}\,\varphi_0 d^3\vec{r} \tag{4-18}$$

using first order perturbation theory and the initial condition that the atom was in its ground state, φ_0. If the dipole matrix element, x_{n0}, is 0, the transition probability is zero and the transition is dipole forbidden. The polarization of the atom induced by the field is

$$\vec{P} = \epsilon_0(\epsilon_r - 1)\,\vec{\mathcal{E}} = -Nq_e \int_V \Psi^* \vec{x}\, \Psi_0 d^3\vec{r} \tag{4-19}$$

Solving the above for the complex relative dielectric constant, ϵ_r, gives

$$\epsilon_r = 1 + \frac{Nq_e^2}{2\epsilon_0 m} \sum_n \frac{f_{n0}}{\omega_{n0}} \left(\frac{1}{\omega_{n0} - \omega - i\gamma} + \frac{1}{\omega_{n0} + \omega - i\gamma} \right) \tag{4-20}$$

at short time scales (i.e. where $\gamma t \rightarrow 0$). f_{n0} is the oscillator strength

$$f_{n0} = \frac{2m\omega_{n0}}{\hbar} |x_{n0}|^2 \tag{4-21}$$

and the real and imaginary parts of the dielectric function are

$$\epsilon_1 = \epsilon_0 + \frac{q_e^2}{m\epsilon_0} \sum_n \frac{Nf_{n0}({\omega_{n0}}^2 - \omega^2)}{({\omega_{n0}}^2 - \omega^2)^2 + (2\gamma\omega)^2} \tag{4-22}$$

$$\epsilon_2 = \frac{q_e^2}{m\epsilon_0} \sum_n \frac{Nf_{n0}\gamma\omega}{({\omega_{n0}}^2 - \omega^2)^2 + (2\gamma\omega)^2} \tag{4-23}$$

which are Lorentzian distribution functions. The complex dielectric coefficient is related to the complex refractive index by

$$\tilde{n} = \sqrt{\epsilon_0 \epsilon_r} \tag{4-24}$$

This Lorentzian profile is often used to model absorptive oscillators to determine the complex refractive index, for example, in ellipsometry. However, in the solid state there are numerous inhomogeneous (i.e. Gaussian), broadening mechanisms beyond the simple lifetime broadening explored here. Crystal field effects and impurity effects both contribute significantly to the line width inhomogeneously, whereas the lifetime broadening considered above and the emission of phonons both produce homogenous broadening resulting in the actual oscillator being of the Voigt type. Extending these results to the relevant application of amorphous solids is non-trivial but the key point has been arrived at: quantum mechanical transitions between states interact with an electromagnetic plane wave of long wavelength through absorption which has the form of a Lorentzian lineshape. This is subsequently broadened into a Voigt profile through interactions of the local potential, and defects in the crystal. This justifies the use of Lorentzian profiles for ellipsometric modeling. In FTIR the measured transmittance spectrum is not proportional to the extinction coefficient and the high degree of disorder within these films prompted the use of Gaussians to fit the absorbance spectra.

Ellipsometry

Ellipsometry is a powerful optical technique used to determine the complex refractive index (i.e. complex dielectric function) and thickness of a thin film. As an optical technique it is truly non-destructive unlike, for instance, RBS and ERD.

The idea of ellipsometry is to measure the change in polarization that a light beam undergoes upon interaction with a sample. The vast majority of ellipsometers are made to perform measurements in reflection. Transmission ellipsometers do exist but the relative difficulty of sample mounting, combined with most of the users working in semiconductor industries with thicker substrates means these ellipsometers are fairly rare.

The complex refractive index, $\tilde{n}$, consists of two parts. The real part, n, also commonly called the refractive index, is the ratio of the speed of light in free space to the speed of light in the material under consideration. The imaginary part, labeled k and called the extinction coefficient, describes the absorption of the film. The polarization of a light beam, down to a single photon, is simply the direction of the electric field that the photon or beam has. We can decompose this vector into x and y components such that when looking back along the direction of propagation (propagating towards +z in Figure 4-3) and orienting the coordinate axes so the p direction is along x and the s direction is along y, we can define the ellipsometric angles, Ψ and Δ. $\tan\Psi$ is the ratio of the magnitudes of the s and p components of the electric field and Δ is the difference in phase between the s- and p- components, i.e. $\tan\Psi e^{i\Delta} = \overrightarrow{E_p}/\overrightarrow{E_s}$.

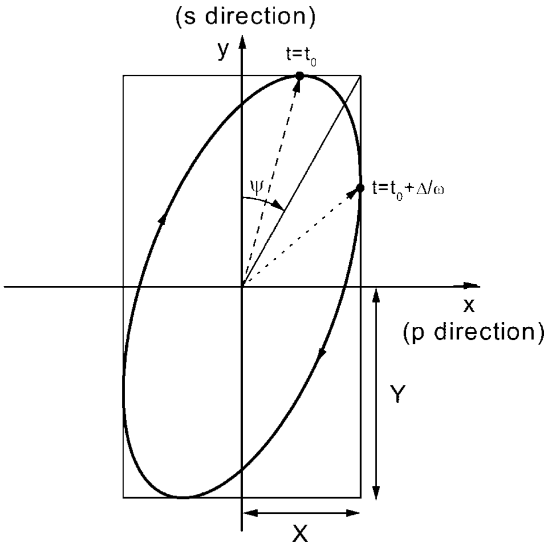

Figure 4-3: Ellipticly polarized light and the definition of Ψ and Δ [79].

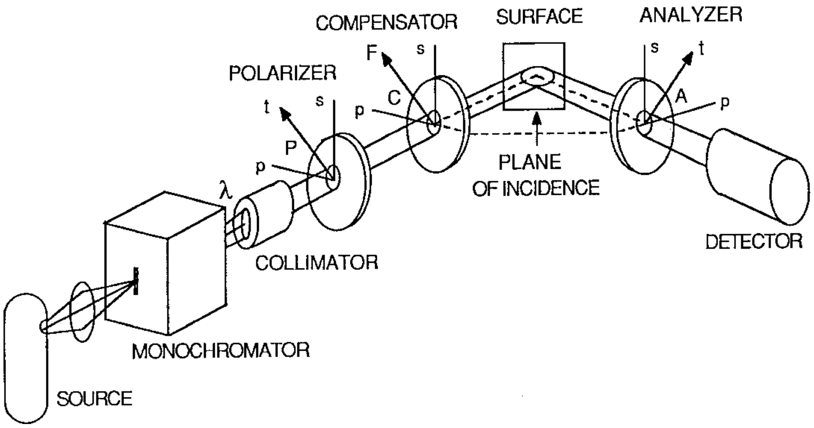

Figure 4-4: Schematic diagram of a PCSA ellipsometer [79].

A typical ellipsometer schematic is shown in Figure 4-4. Indeed, the spectroscopic ellipsometry (SE) measurements used in this thesis were made using a J.A. Woollam M2000V Variable Angle Spectroscopic Ellipsometer, which operates on a rotating compensator design with a schematic identical to that shown in Figure 4-4. Let us then assign co-ordinate axes such that the plane of incidence is the x-z plane, and the direction of propagation is along the z-axis. The light source could be either a thermal source with the generated light passing through a monochromator and a collimator, or a laser source. The advantage of the thermal source is that it can be used in spectroscopic measurements, but at an increased equipment cost. The randomly polarized beam produced is then passed through a polarizer, P, resulting in an electric field intensity:

$$\overrightarrow{E_p} = E_p \cos P\,\hat{x} + E_p \sin P\,\hat{y} \tag{4-25}$$

The beam then passes through a compensator which introduces a phase shift between the two components contained in the complex transmission coefficients t_{fast} and t_{slow},

$$\begin{aligned}\overrightarrow{E_c} &= E_p t_{fast}[(\cos P \cos C + \sin P\ \sin C)\cos C\,\hat{x} + (\cos P \cos C + \sin P\ \sin C)\sin C\,\hat{y}] + \\ &E_p t_{slow}\left[\left(\cos P \cos\left(C + \frac{\pi}{2}\right) + \sin P\ \sin\left(C + \frac{\pi}{2}\right)\right)\cos C\,\hat{x} + \left(\cos P \cos\left(C + \frac{\pi}{2}\right) + \sin P\ \sin\left(C + \frac{\pi}{2}\right)\right)\sin C\,\hat{y}\right] \\ &= E_p\big[t_{fast}\big((\cos(P - C))\cos C\,\hat{x} + (\cos(P - C))\sin C\,\hat{y}\big) - t_{slow}(\sin(P - C)\sin C\,\hat{x} - \sin(P - C)\cos C\,\hat{y})\big]\end{aligned} \tag{4-26}$$

After the sample the electric field becomes

$$\begin{aligned}\overrightarrow{E_s} &= E_{cx} r_x \hat{x} + E_{cy} r_y \hat{y} \\ &= E_p \begin{bmatrix}\big(t_{fast}(\cos(P - C))\cos C - t_{slow}\sin(P - C)\sin C\big)\hat{x} \\ \big(t_{fast}(\cos(P - C))\sin C + t_{slow}\sin(P - C)\cos C\big)\hat{y}\end{bmatrix}\end{aligned} \tag{4-27}$$

Due to the way the coordinate system was chosen the $\hat{x}$ direction is the direction of polarization for p waves and the $\hat{y}$ direction is the direction of polarization for s waves. Finally passing through the analyzer the amplitude of the transmitted light is

$$E_a = \left(E_{cx} r_x \hat{x} + E_{cy} r_y \hat{y}\right) \cdot (\cos A\,\hat{x} + \sin A\,\hat{y}) \tag{4-28}$$

$$E_a = E_p \left[\begin{array}{c} \left(t_{fast}(\cos(P-C))\cos C - t_{slow}\sin(P-C)\sin C\right)\cos A r_p + \\ \left(t_{fast}(\cos(P-C))\sin C + t_{slow}\sin(P-C)\cos C\right)\sin A r_s \end{array}\right] \tag{4-29}$$

For null ellipsometry we determine the angle (of the polarizer, compensator, or analyzer depending on the variant) that minimizes (ideally zeroes) the detected light.

$$0 = E_p \left[\begin{array}{c} \left(t_{fast}(\cos(P-C))\cos C - t_{slow}\sin(P-C)\sin C\right)\cos A r_p + \\ \left(t_{fast}(\cos(P-C))\sin C + t_{slow}\sin(P-C)\cos C\right)\sin A\, r_s \end{array}\right] \tag{4-30}$$

and hence

$$\frac{\mathrm{r_p}}{\mathrm{r_s}} = \tan A \frac{\tau_c \tan(P-C) + \tan C}{\tau_c \tan(P-C)\tan C - 1} = \tan \Psi e^{i\Delta} \tag{4-31}$$

The complex reflection coefficient can be calculated from the Fresnel equations:

$$\mathrm{r_p} = \frac{\tilde{n}_e \cos\theta_r - \tilde{n}_f \cos\theta_i}{\tilde{n}_e \cos\theta_r + \tilde{n}_f \cos\theta_i}, \mathrm{r_s} = \frac{\tilde{n}_e \cos\theta_i - \tilde{n}_f \cos\theta_r}{\tilde{n}_e \cos\theta_i + \tilde{n}_f \cos\theta_r} \tag{4-32}$$

where $\tilde{n}_e$ is the complex of index of refraction of the environment of our material of interest (equal to 1 in most cases since the environment is air), $\tilde{n}_f$ is the complex index of refraction of the material, , and θ_i and θ_r are the angles of incidence and refraction respectively. However, this is valid only for light incident on a single material. In this thesis the material of interest is a thin film on a substrate and this must be accounted for when we attempt to determine the index of refraction. For a thin film on a substrate the total reflection from the sample, R, is

$$R_s = \frac{\mathrm{r_s} + \mathrm{r_{s,s}}\mathrm{e}^{-\mathrm{i}2\mathrm{b}}}{1 + \mathrm{r_s}\mathrm{r_{s,s}}\mathrm{e}^{-\mathrm{i}2\mathrm{b}}}, R_p = \frac{\mathrm{r_p} + \mathrm{r_{s,p}}\mathrm{e}^{-\mathrm{i}2\mathrm{b}}}{1 + \mathrm{r_s}\mathrm{r_{s,p}}\mathrm{e}^{-\mathrm{i}2\mathrm{b}}}, b = \tilde{\mathrm{n}}_\mathrm{f}\frac{2\pi d}{\lambda}\cos\theta_f \qquad (4\text{-}33)$$

where $\mathrm{r_s}$ and $\mathrm{r_p}$ are the reflection coefficients of the air-film interface in the *s* and *p* directions, $\mathrm{r_{s,s}}$ and $\mathrm{r_{s,p}}$ are the reflection coefficients of the film-substrate interface in the *s* and *p* directions, d is the film thickness, λ is the free space wavelength of the radiation and θ_f is the angle defining the direction of light propagation in the film. For additional film layers the total reflection coefficients are developed in the same way, by applying the Fresnel equations at each interface, but the mathematics quickly becomes extensive and will not be detailed here. Since both thickness and the complex index of refraction are unknown, we have more unknowns than equations and thus we need some additional information to determine these variables. The additional information needed is the continuity of the refractive index with respect to wavelength, which allows us to attempt to determine the index numerically through the use of the Kramers-Kronig relations which relate the real and imaginary parts of a complex function which is analytic (which is to say, differentiable in the complex plane).

$$n(\omega) = 1 + \frac{1}{\pi}\int_{-\infty}^{\infty}\frac{\kappa(\omega')}{\omega' - \omega}d\omega' \qquad (4\text{-}34)$$

$$\kappa(\omega) = \frac{1}{\pi}\int_{-\infty}^{\infty}\frac{1 - n(\omega')}{\omega' - \omega}d\omega' \qquad (4\text{-}35)$$

Here $\omega = 2\pi/\lambda$ is the angular frequency of the light and ω' is a dummy variable for integration. The important points to note here are that we need an initial guess for either the refractive index or the extinction coefficient, and that the limits of integration go out to $\pm\infty$, and hence must be extrapolated out from the initial guess and the subsequent calculations. We propose a model structure and define starting values using a material as similar as possible to our actual material so that the fitting process yields good results. The goodness of fit parameter used is typically the reduced mean square error (MSE)

$$\chi^2 = \frac{1}{N-M-1}\sum_{j=1}^{N}\frac{\left(f_{exp}(\lambda_j) - f_{calc}(\lambda_j, \vec{z})\right)^2}{\left(\sigma(\lambda_j)\right)^2} \tag{4-36}$$

where N is the number of measurement points, $f_{exp}(\lambda_j)$ is the experimentally determined set of datapoints at each wavelength λ_j, $f_{calc}(\lambda_j, \vec{z})$ is the numerically determined set of data points for a certain set of input parameters $\vec{z}$, $\sigma(\lambda_j)$ is the experimental error at each data point. The advantage of using the reduced MSE is that it allows for repeatable fits to be determined irrespective of the particular representation of the experimental data used (i.e. Δ and Ψ, or any of several other possible representations including directly the measured data). Possible sources of error that can contribute to σ include nonidealities in the optical elements, poor calibration and misalignment of the elements, uncertainty in the measurement of the angle of incidence, and the error in any assumed data set used for modelling. The typical model structure used in this thesis is shown in Figure 4-5. The top most layer is modeled with an effective medium theory to estimate the surface roughness and its effects on the optical functions. Below this lies the homogenous layer that represents the bulk of the film. A flat smooth interface is assumed at the silicon substrate and the presence of a native oxide is neglected.

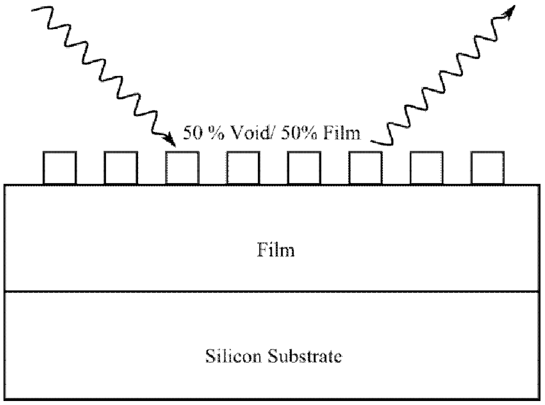

Figure 4-5: Model structure used for simulation of the ellipsometry results.

Photoluminescence

Photoluminescence is an optical technique which gives information regarding the electronic band structure and decay pathways. The fundamental idea is to optically excite the valence band electrons and examine the radiation that results when the electrons decay back to their ground state. The PL apparatus used in this thesis is pictured below in Figure 4-6. The system consists of a Helium-Cadmium laser operating at 325nm, a mirror, sample stage, front end optics, an optical fiber and a spectrometer. A detailed description of the theory of photoluminescence is not required for the purposes of this thesis; the interested reader is referred to the quite comprehensive treatment given by Bebb and Williams in Chapter 4 of [81]. The strength of the received signal cannot be used to reliably determine efficiency of the luminescence, though relative intensities are readily compared.

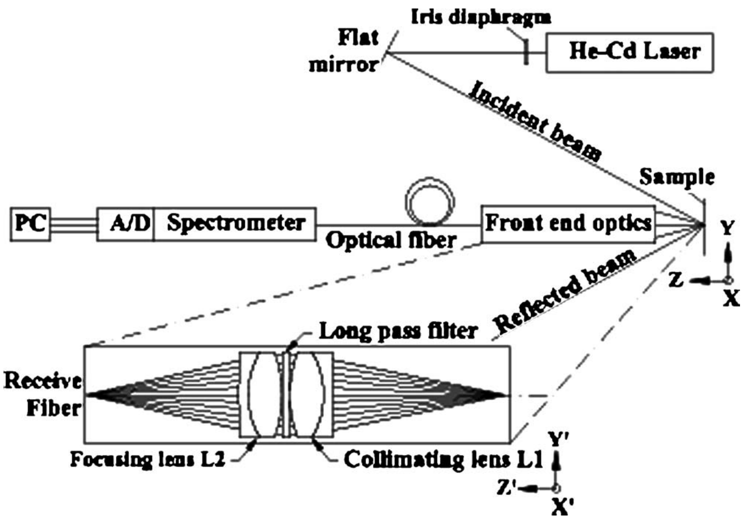

Figure 4-6: Schematic of a PL system [82].

The electron can be excited into states other than those of the conduction band. Defect states and surface/interface states can fall within the bandgap. Also, higher energy bands and states can be excited to such an extent that they are freed from the potential distribution of the sample. Typical spectra can be well approximated with Gaussian profiles, though in the more rigorous discussion in [81] the shapes are actually seen to be a sum of several different exponential terms. In silicon nitride several decay pathways from the valence band have been identified, including the direct bandgap energy of 5.05eV, and interbandgap states [29].

As was noted above silicon is an indirect bandgap material whereas silicon nitride and silicon carbon nitride are both direct. In Figure 4-7 the distinction between these two is made clear. On the left an incident photon excites an electron from the valence band to the conduction band with no change (or at least very little change due to the tiny momentum of the photon) in its wave vector, **k**. While **k** is not a good quantum number in amorphous materials it serves as a convenient label for momentum here. On the other hand, in an indirect semiconductor the electron is excited to a higher energy than that of the conduction band minimum. The electron then very rapidly decays via vibrational interactions to the conduction band minimum. The electron however cannot then decay to the valence band without also absorbing a phonon. Thus, the luminescence intensity depends on the probability of the excited electron interacting with a phonon, so a higher temperature (increasing the phonon density) increases the efficiency. However, as the temperature increases the probability that the electron decays back to the ground state non-radiatively also increases, resulting in decreasing luminescence efficiency. For silicon at or near room temperature the non-radiative decay paths dominate and thus silicon is a very inefficient light emitter.

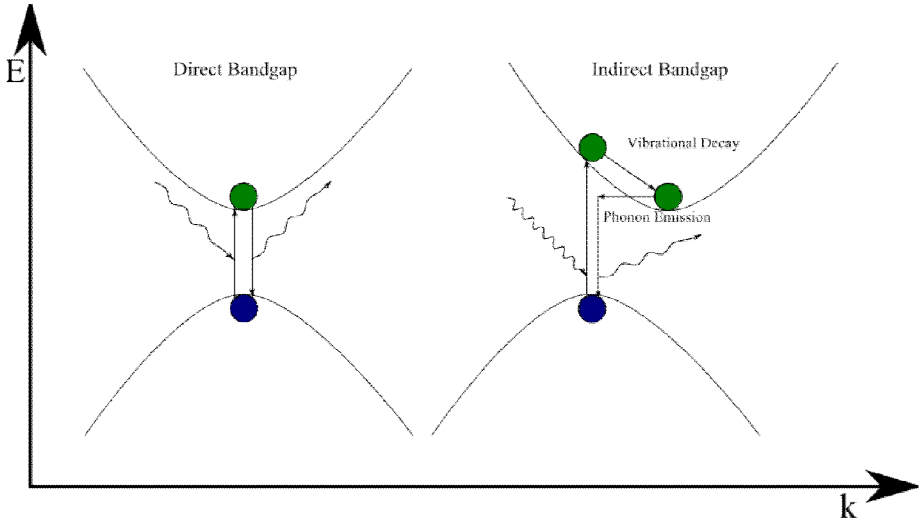

Figure 4-7: Cartoon of direct and indirect absorption and emission of photons.

As a mechanism to overcome the poor luminescent efficiency of silicon one can make use of quantum confinement. By analogy to the particle in a box problem the valence electrons are confined to a small region of space which results in more direct electronic transitions. The particle in a box problem places an elementary particle in a potential energy function of the form

$$V(x,y,z) = \begin{cases} 0 \text{ if } 0 < x,y,z < a,b,c \\ A \text{ otherwise} \end{cases} \tag{4-37}$$

i.e. a,b,c are the spatial bounds of the box. The time independent Schrödinger equation is then,

$$\nabla^2\psi + V\psi = E\psi \tag{4-38}$$

which has a solution

$$\psi = \sqrt{\frac{8}{abc}}\sin\frac{n_x\pi x}{a}\sin\frac{n_y\pi y}{b}\sin\frac{n_z\pi z}{c} \tag{4-39}$$

where n_x, n_y, n_z are integers and discrete energy eigenvalues

$$E_{n_x n_y n_z} = \frac{\hbar^2\left(\left(\frac{n_x\pi x}{a}\right)^2 + \left(\frac{n_y\pi y}{b}\right)^2 + \left(\frac{n_z\pi z}{c}\right)^2\right)}{2m} \tag{4-40}$$

So, spatial confinement results in well-defined energy levels, without the energy dependence on momentum that is found in solids. Attempting to approximate this idealized structure in a solid then can significantly alter its optical characteristics. In this thesis it is the working assumption that quantum confinement due to a nanocluster structure is important in developing efficient luminescence.

PL decay rates are important for a silicon light source to be capable of handling the high data throughput of modern computing architectures and in order to reduce the effect of the relatively slow non-optical recombination pathways via phonon excitation. To evaluate the suitability of SiC_xN_y for global interconnects some preliminary time dependent PL measurements were taken. The experimental setup consists of a pulsed laser source directly illuminating the sample, a photomultiplier tube, and a voltmeter which samples the PMT signal every 2 ps. The data collected is in the format of total intensity detected as a function of time. To this we fit a stretched exponential, i.e. a function of the form:

$$I(t) = I_0 e^{(-t/_\tau)^{\beta}} \tag{4-41}$$

where $I(t)$ is the total intensity, I_0 is representative of the peak intensity, β is the stretching factor, and τ is the decay time time constant and are used as fitting parameters, necessitating a minimum of three data points. For reference, decay times for silicon nanocrystals in a silicon dioxide matrix are often in the tens of µs, while in silicon nitride a typical time is in the neighbourhood of tens of ns. So, a non unity stretching factor indicates that there is more than one possible decay path.

Transmission Electron Microscopy

At the scale of the structures of interest in this thesis conventional visible light based microscopy is useless since structures on the scale of a few nanometres are well below the Raleigh diffraction limit and thus indistinguishable. To avoid this problem an electron microscope can be used which takes advantage of the wave nature of electrons, to form the image. The wavelength of an electron is related to its energy by the de Broglie relation:

$$\lambda = {}^{h}/_{p} \tag{4-42}$$

where h is Planck's constant, and p is the momentum. In this thesis a JEOL 2010F electron microscope was used for bright field images and an FEI Titan 80-300 high resolution transmission electron microscope was used to take the dark field images and electron energy loss spectroscopy (EELS) results. Both instruments are located in the Canadian Centre for Electron Microscopy (CCEM) at McMaster. Inelastic and elastic scattering mechanisms can change the direction and energy of electrons in the beam in a characteristic way that depends on the specific scattering mechanism (i.e. Rutherford, Plasmon, vibrational, core loss etc.). Hence, due to the extremely small wavelength, the imaging and analytical capabilities of the TEM make it a powerful tool to examine a wide variety of material science characteristics.

Prior to the experiment the sample must be specially prepared. This process has four main steps:

1) Cleaving small bars, approximately 1mm wide, of a bare silicon wafer and of the sample, then gluing them together with an epoxy to form a raft.
2) Mechanically polishing the raft, using up to 1200 grit silicon carbide sandpaper, to reduce the thickness of the raft down to 100-150μm.
3) Mechanical polishing using a rotary wheel "dimpler" to reduce the thickness down to approximately 15-20μm.
4) Ion beam milling using an Ar^+ ion beam at low angle (around 4°) to form a hole through the centre of the sample. The shallow angle of the ion beam(s) results in an extremely sharp pointed wedge region around the sample hole. It is this wedge region of the sample that will have the beam passed through for imaging.

The basic structure of a TEM is pictured in Figure 4-8. The primary feature of the TEM is the so-called stack whose basic components are the electron source, a variety of electromagnetic lenses, the sample stage, apertures, and a detector. The electron source generates electrons in one of two ways. The first is by thermionic emission where a tungsten (obsolete), or LaB_6 (the only kind used in modern TEMs) filament is heated and electrons "boil" off; this is called a hot source. The second is by field emission where a powerful DC voltage (in the range of a few kV) is applied. These electrons are then accelerated by the main stack voltage, sometimes into the hundreds of kVs that provide the energy for the beam. Via the de Broglie relation above it is seen that higher energy electrons result in a shorter wavelength and thus higher resolving power of the beam, though in practice the upper limit to modern TEM voltages is around 400kV as aberration effects become the resolution limiting factor at higher voltages/energies [83]. Electromagnetic lenses are simply current carrying coils which induce a magnetic field in the beam path. As a result of the Lorentz force the greater the electron's distance is from the stack axis the greater the force on the electron towards the stack axis. A soft iron shell surrounds the lens to minimize the stray magnetic fields generated, with the actual lensing action occurring in the gap region. The strength of the path deflection can be controlled by varying the current through the coil, implying that the cross over point of the rays (within the thin lens approximation) can be adjusted out to any distance. Thus the lenses can both collimate and focus the beam. A schematic of the lens is seen in Figure 4-8a. Two very important parameters of the lens are the spherical, C_s, and chromatic aberration, C_c. C_s refers to the increase in wave front curvature that electrons farther from the stack axis experience whereas C_c (usually a much smaller effect) is due to the fact that the beam is not truly monochromatic and lower energy electrons are deflected

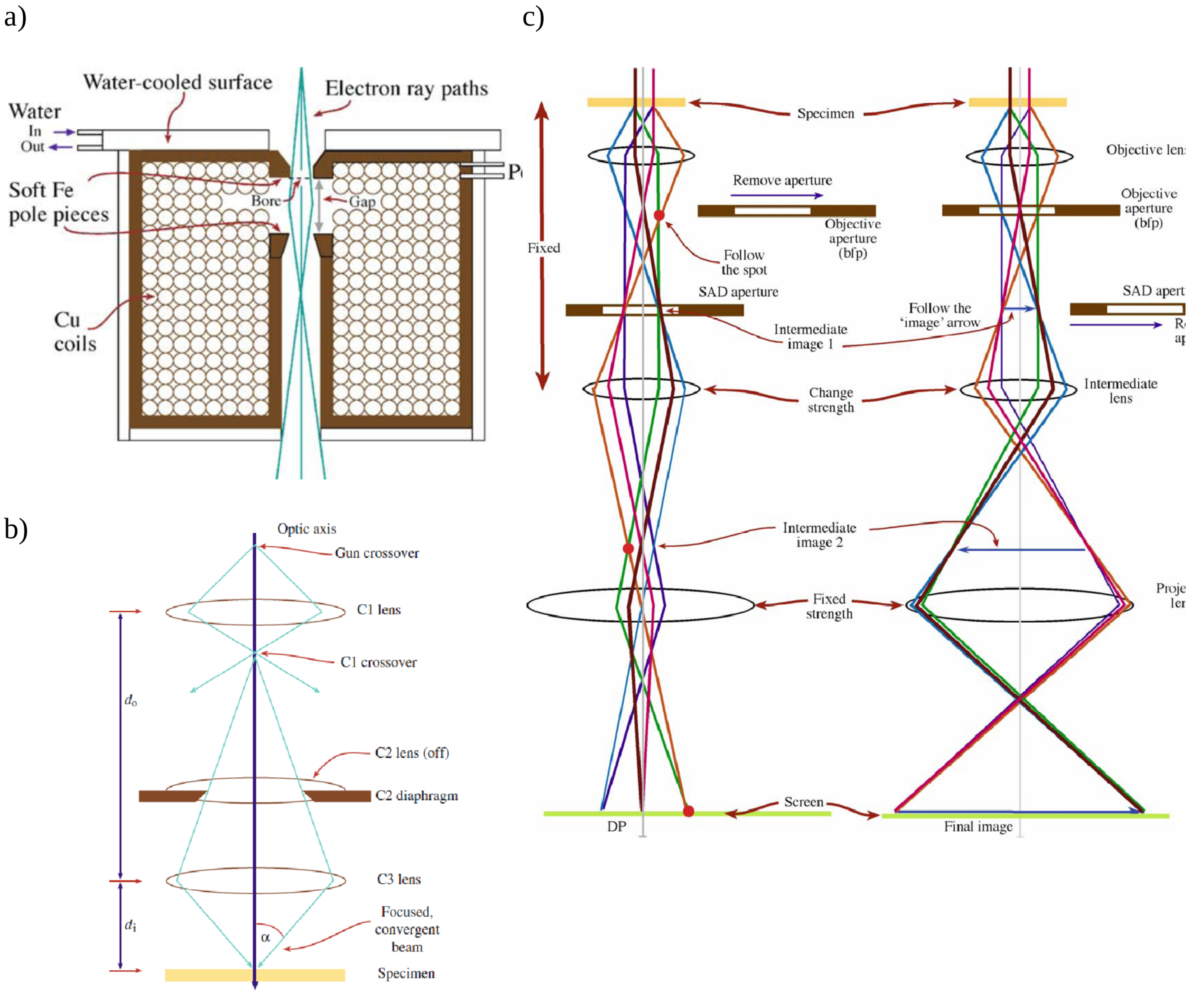

Figure 4-8: a) Schematic diagram of a typical magnetic lens. b) Thin lens ray diagram from the electron gun to the specimen. c) Thin lens ray diagram from the specimen to the detector. All images from [83].

more strongly in the lens. Figure 4-8b and Figure 4-8c are thin lens ray diagrams. In Figure 4-8b the electrons in the beam generated by the electron gun are collected by the first condenser lens, C_1. The second condenser lens and the upper objective lens then are used to direct the electrons towards the specimen in either a convergent beam suitable for STEM work, or into a parallel beam suitable for imaging and diffraction (not shown). Figure 4-8c begins with the beam passing through the specimen and being scattered into an annulus with a size corresponding to the scattering atom and the scattering mechanism. The beam then passes through the second objective lens for imaging or selected area diffraction. Finally the beam passes through the intermediate lens and projector lens for the generation of an image at the detector. Historically, images were taken by exposing an electron sensitive dye to the beam, however, in modern systems the beam is typically collected into a sensitive CCD camera and saved in digital format directly onto a computer.

There are three primary methods (see Figure 4-9) which produce an image when the sample is illuminated by the electron beam, with so-called bright field imaging being the simplest. The collimated beam produced in the condenser is passed through the sample, electrons scatter from the atoms in the sample and are subsequently blocked by the objective aperture whereas the unscattered beam goes straight through. Higher density regions scatter the beam more strongly and thus, appear darker. In contrast, off-axis dark-field imaging is performed by moving the aperture to a location within the annulus of scattered electrons and blocking the straight through beam. Due to the Z-dependence of electron scattering this can be used to give some limited information on the chemical composition of the sample, though for light and closely spaced elements this effect is negligible. On-axis dark field imaging is done by tilting the sample relative to the beam, though this of course increases the path length of the beam through the sample. It is unsuitable for use with the samples produced in this thesis when EELS measurements are also desired due to the sensitivity of EELS to sample thickness. The lens names in Figure 4-8, other than the intermediate lens, are derived from their function in the TEM, thus the condenser lenses “condense” the broad beam produced by the electron gun, the objective lenses focus the beam onto the object, and the projector lens projects the image onto the detector.

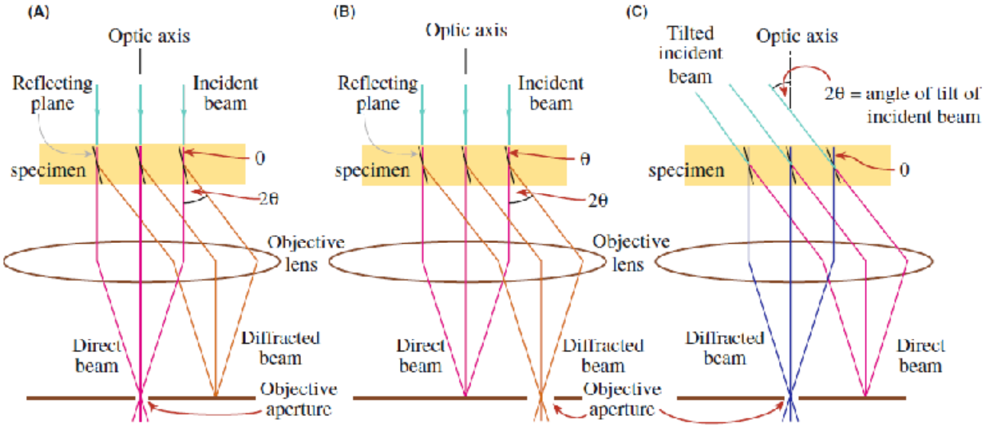

Figure 4-9: The 3 different TEM imaging modes: a) bright field, b) off-axis dark field, c) on-axis dark field, from [83].

Beyond imaging, the most commonly used technique in TEM is undoubtedly electron diffraction. Here, similar to x-ray diffraction, we irradiate the sample with a beam (of electrons instead of x-rays) where the solid sample acts as a diffraction grating. In crystalline solids the x-ray scattering can be interpreted as occurring from planes of atoms, from which we can derive the Bragg relation $n\lambda = 2d\sin\theta$ where d is the distance between atomic layers and n is an integer labelling the diffraction spot. In amorphous materials, however, there is no long range order, so there are no well defined planes for an x-ray to diffract from, and reciprocal space is not well defined. The diffracted signal is not a pattern of sharp spots, like those obtained from crystals, or a series of sharp rings as in polycrystalline films but diffuse rings [84]. From the elastic differential scattering cross section for an unpolarized beam of x-rays

$$\frac{d\sigma}{d\Omega} = \left(\frac{{q_e}^2}{4\pi\epsilon_0 m_e c^2}\right)\left(\frac{1 + \cos^2\theta}{2}\right) \tag{4-43}$$

and by assuming that: 1) the scattered waves can be treated as plane waves, valid providing the scattering centre is many wavelengths away from the detector (very reasonable), 2) the scattering centres possess spherical symmetry (since x-rays interact only with the electron cloud this is more suitable for high Z elements where the directional aspects of the valence electrons caused by bonding are less significant), 3) that no absorption edges or inelastic scattering mechanisms are important, and 4) the material is isotropic, one can derive an expression for the scattered intensity, the Debye equation:

$$I_{eu} = \sum_m \sum_n f_m f_n \frac{\sin k r_{mn}}{r_{mn}} \tag{4-44}$$

where $k = \frac{4\pi \sin\theta}{\lambda}$ is the scattering wavevector, r_{mn} is the distance between two scattering centres, f_m and $f_n$are the atomic scattering factors for the mth and nth atoms respectively. The subscript *eu* refers to the use of electron units, i.e. the above equation is in terms of

$$\frac{d\sigma}{d\Omega}\frac{I_0}{R^2} \tag{4-45}$$

with I_0 being the magnitude of the incident radiation and R the distance to the detector. The atomic scattering factor for x-rays is given by

$$f^x = \sum_j \int_0^\infty 4\pi r^2 \rho_j(r) \frac{\sin kr}{kr} \tag{4-46}$$

The few attempts at x-ray diffraction done during this thesis, however, resulted in essentially featureless rocking curves, so we are more concerned with the results from electron diffraction. The key differences between x-ray and electron diffraction are that the electron has a much smaller wavelength and that it is charged. The charged nature necessitates modifying the atomic scattering factor to

$$f^e = \frac{2m_e {q_e}^2}{\hbar^2}\left(Z - \frac{f^x}{k^2}\right) \tag{4-46}$$

To progress further, details of the atoms involved in the scattering must be invoked for every combination of atoms, and an independent scattering technique applied in each case in order to derive the radial distribution function (RDF) [84]. The RDF is essentially a measure of the number of atomic nuclei at a certain distance from the scattering centre and is the desired function for diffraction based techniques as it contains the bonding coordinations and lengths of the sample [84]. For this reason complete structural data could not be determined from the diffraction patterns obtained (above and beyond the fact that the structural anisotropy of the sample makes this method questionable). A brief description of the electron diffraction results will be given in the discussion section but a truly comprehensive determination of the structure is not possible with diffraction alone.

X-ray absorption spectroscopy

X-ray absorption spectroscopy is an element specific sensitive probe of the chemical environment that results in macroscopic aggregate measurement suitable for determining the bonding environment, electronic structure, and in some cases vibrational structure of the film. The measurements performed in this thesis were done at the Canadian Light Source (CLS) synchrotron facility on the variable line spacing-plane grating monochromator (VLS-PGM) beam line. The basic premise is to direct a beam of x-rays onto a sample and measure either the fluorescence of the sample or the compensation current of electrons that have been ejected from the sample. As the energy of the beam of x-rays increases (the variable x-ray energy is the reason for the use of a synchrotron facility as opposed to a more standard x-ray lamp), it will cross the excitation energy barrier of a core shell electron, exciting the electron to a higher energy state. The electron is excited into an unoccupied state in the conduction band, higher unoccupied bands, or into a continuum state where it is ejected from the sample. At the relatively low energies of only a few hundred eV, the EELS and XAS spectra are directly proportional to one another [85] so the theory covered here regarding core level excitations is similar for both. When this happens, the x-ray absorption coefficient rises sharply and likewise the number of fluorescent x-rays and backscattered electrons increases.

The derivation for the absorption coefficient, according to [86], is similar to the time dependent perturbation theory used above. We begin by defining the total scattering cross section, σ_{if}, for a transition from initial state i, to final state f,

$$\sigma_{if} = \frac{P_{if}}{F_{ph}} \tag{4-47}$$

where P_{if} is the probability that a photon will excite an electron from i to f, and F_{ph} is the photon flux. F_{ph} is determined by assuming a monochromatic electromagnetic plane wave, the x-ray, using the magnetic vector potential in the coulomb gauge

$$\vec{A} = A_0\hat{E}\left(e^{i(\vec{k}\cdot\vec{x}-\omega t)} + e^{-i(\vec{k}\cdot\vec{x}-\omega t)}\right) \tag{4-48}$$

A_0 is the amplitude of the radiation, $\vec{k} = 2\pi/\lambda$ the wavevector, $\vec{x}$ the position, and ω is the angular frequency. However, assuming radiation incident from one direction, we can neglect one of the traveling waves, say the leftward traveling wave. The number of photons is the intensity of the electromagnetic field divided by the energy of each photon

$$F_{ph} = \frac{{A_0}^2\omega}{8\pi\hbar c} \tag{4-49}$$

and P_{if} is given by Fermi's Second Golden Rule

$$P_{if} = \frac{2\pi}{\hbar}\left|\langle\psi_f|H'|\psi_i\rangle\right|^2\rho(k) \tag{4-50}$$

where ψ_f is the wavefunction of the system in the final state, ψ_i is the wavefunction in the initial state, $\rho(k)$ is the density of final states and H' is the time dependent Hamiltonian of the perturbing function. For the plane wave form of the x-ray the perturbation can be taken to be

$$H' = \frac{q_e}{mc}\vec{A}\cdot\sum_i\vec{p_i} \tag{4-51}$$

where the p_i are the linear momentum operators of every electron considered in the system. This yields then a total scattering cross section of

$$\sigma_{if} = \frac{\pi {q_e}^2{A_0}^2}{2\hbar m^2c^2}\left|\left\langle\psi_f\left|\hat{E}e^{i(\vec{k}\cdot\vec{x})}\cdot\sum_i\vec{p_i}\right|\psi_i\right\rangle\right|^2\rho(k) \tag{4-52}$$

The time dependency of the wave introduces only a phase factor and is eliminated when taking the magnitude. Furthermore, under the traditional dipole assumption $\vec{k}\cdot\vec{x} \ll 1$ we arrive at

$$\sigma_{if} = \frac{\pi {q_e}^2 {A_0}^2}{2\hbar m^2 c^2} \left| \left\langle \psi_f \middle| \hat{E} \cdot \sum_i \vec{p_i} \middle| \psi_i \right\rangle \right|^2 \rho(k) \tag{4-53}$$

which is the standard operating formula used in X-ray absorption-near edge structure (XANES) calculations. The initial and final states are not simply represented, and in every case of interest the Schrödinger equations needed to find them cannot be solved analytically. Since the spectroscopy uses core level electrons whose initial states are only minimally affected by the local environment, it is common to take the initial states to be those of an unperturbed, isolated atom. The final states, on the other hand, depend heavily upon the valence electronic characteristics of the material in question. So, more advanced simulation schemes must be employed. Initially the Hartree-Fock self consistent field method was employed, though configuration interaction and DFT based methods have since become more common. For the qualitative analysis performed in this thesis, precise knowledge of the final states is not necessary as the analysis is based on spectral comparison as opposed to first principles calculation. Regardless, the importance of the density of states, $\rho(k)$, is seen and it is the factor that is discussed.

The dipole approximation is suitable when $|\vec{x}|$, the approximate size of the atomic orbitals being probed is $\ll \lambda/2\pi$, which for 100eV radiation of the silicon *2s* and *2p* levels is easily the case. Quadrupole interactions can become important at extremely high energies but such effects are not considered in this thesis. So, in XAS of solids we are probing the partial density of unoccupied states. It is only a partial density of states due to the fact that photons carry a quantum of spin angular momentum $\hbar$ and hence the

$\Delta l = \pm 1$ selection rule applies, though it is relaxed somewhat in the low symmetry states found in amorphous solids.

In the literature there are a large number of silicon, carbon, and nitrogen K-edge (i.e., electrons are excited from the 1s level) spectra reported [87], however there is a relative dearth of L-edge spectra. K-edge spectra have the advantage of lying lower in energy, closer to the atomic nucleus, and hence are less sensitive to the atomic environment. However, L-edge spectra (i.e., electrons are excited from both *2s* and *2p* levels) are able to probe a greater portion of the unoccupied DOS as the $\Delta l = \pm 1$ rule is relaxed somewhat due to stronger interactions with neighbouring atoms.

Electron Energy Loss Spectroscopy

EELS is an advanced spectroscopic technique that can be used to determine the local bonding structure of a film. It is a complementary technique to XAS, producing similar plots and providing similar data, but with a microscopic rather than macroscopic sample area. By far the majority of EELS measurements performed nowadays are performed in the TEM. In another sense it provides complementary information to energy dispersive x-ray spectroscopy (EDX) as it can determine the elemental composition, similar to EDX, but it is best applied at energies below 2keV, which is the region where EDX is least useful [83]. In this thesis the experiments were done in the FEI Titan 80-300 Cryo In-situ microscope in the Canadian Centre for Electron Microscopy (CCEM). It should also be noted that historically EELS found its greatest application in gas phase analysis, and that though only transmission measurements will be further discussed, reflection measurements of EELS, which give surface sensitive results, have also been done. The spectrum is collected by passing the beam, which has been focused for scanning mode operation, through a magnetic prism (a curved magnetic lens), which splits the beam according to energy. The beam then falls on a CCD camera, or a filter and photodiode, for detection.

Energy filtered TEM (EFTEM) is performed in the same way except the beam is scanned across a region and measurements are taken at points distributed over the region. The filtering action can occur either prior to detection, where information from some regions of the loss curve is discarded, or after the measurement using software to select specific regions of interest, as is done in this thesis.

A typical EELS spectrum is usually divided into three main regions, the extremely intense zero loss peak (ZLP), located near zero energy loss, the low loss region, which is where intraband, interband, and plasmon losses occur, and the high loss region where core shell excitation occurs. The ZLP actually contains information regarding the vibrational structure of the material as electrons can lose small amounts of energy (meV, well within the ZLP region), but this structure is typically unresolvable. It is also unnecessary due to the ready availability of FTIR equipment. The ZLP is typically used in conjunction with a filter as a way to increase the resolution, by reducing the effects of chromatic aberration. The low loss region is often the most intense region of the EELS spectrum, particularly for metals, as the high density of relatively free electrons permits a strong response to the electron beam. Key mechanisms for energy loss at only a few eV or less of energy loss are interband and intraband transitions which can be used to derive the electronic band gap or the complex dielectric function. Unfortunately, this typically requires quite high resolution scans and in the case of SiC_xN_y the plasmon excitation is very weak so these will not be discussed further here. In Figure 4-10 most of the possible excitation and de-excitation mechanisms are shown schematically. Excitations of energy ΔE_1 occur from from the core levels (K, L_1, L_2, L_3) to the conduction band and are the most important in EELS. Also relevant to a discussion of EELS (and XAS) are Auger electrons (A.E.), backscattered electrons (B.E.), and secondary electrons (S.E.) as these electrons can be detected in addition to the beam electrons. X-rays (labelled X in Figure 4-10) can also be produced, though only minimal X-ray analysis (EDX) was performed as part of this thesis.

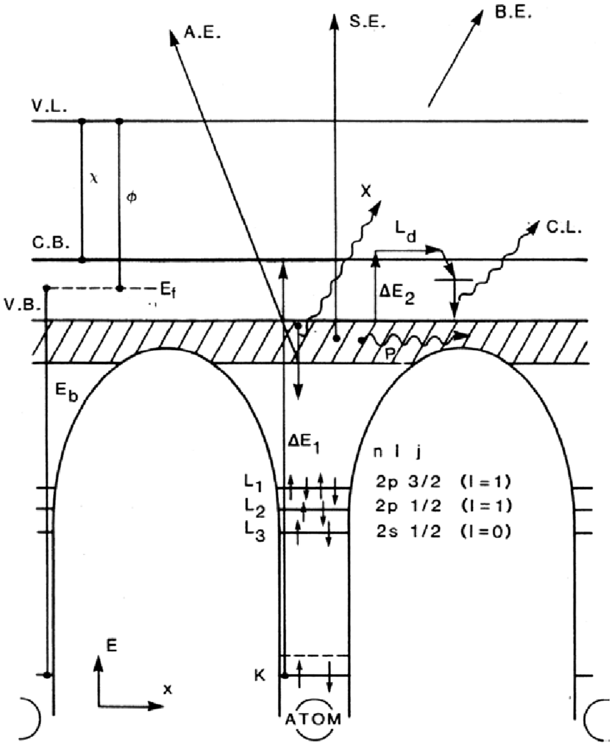

Figure 4-10: Core shell excitation, and de-excitation mechanisms involved in EELS [88]. V.L. indicates the vacuum level, C.B. the conduction band, V.B. The valence band, E_f the Fermi level, χ the electron affinity, ϕ the work function, E_b the bonding energy, C.L. a cathodoluminescent photon, ΔE_2 the energy of the bandgap.

The high loss region contains the information of interest in the majority of EELS measurements, namely element specific bond lengths and atomic coordinations. As with XAS, EELS probes the unoccupied density of states through the excitation of a core electron. The edge notation used in this field is identical to that practiced in XAS though the labels (K, L, M etc.) now refer to ionization edges as opposed to absorption edges [85]. This is a slightly misleading term as core loss EELS excites electrons to any of the states above the Fermi level, not just into the vacuum. Regardless, the intensity of the core loss peaks corresponds directly to the density of scattering elements and their scattering cross section, so integrating these peaks can provide a quantitative measure of the atomic concentration. As well, the high energy loss peaks contain fine structure related to the chemical bonding; for instance, the pre-edge peak of the carbon K-edge is related to sp^2 hybridized carbon like that found in graphite. Unfortunately, the resolution of the spectra taken in this thesis proved insufficient to distinguish much of the structure clearly. There are many effects which can cause this lack of resolution, arguably the most important of which is excessive sample thickness, which reduces the applicability of a single scattering interpretation of the EELS spectrum and causes the spread in energy loss due to multiple interactions. The samples prepared in this thesis were on the order of 50nm thick, i.e. a few times the typical mean free path of an electron in silicon nitride.

Chapter 5 : Results and Discussion

The deposition parameters used for the major samples produced in this thesis are presented in Table 5-1and Table 5-2. Prior to these samples a series of samples was deposited with widely varying nitrogen flow rates, attempting to zero in on the region where luminescent activity could be observed. However, due to a configurational change in the setup of the ICP-CVD system (nitrogen was being flowed through the dispersion ring and not as a plasma gas), even when repeating depositions known to produce luminescent samples this series did not produce any light.

Table 5-1: Deposition parameters for first successful series of luminescent films.

Sample Label	SiH_4 flow (sccm)	CH_4 flow (sccm)	N_2 flow (sccm)	Ar flow (sccm)	T_{heater} (˚C)	Power (W)	t_{dep} (min)
SCNI505*	5	2	4	3	500	300	120
SCNI505a	5	2	4	3	500	300	120
SCNI505b	5	2	4	10	500	300	120
SCNI505c*	5	2	4	10	500	300	120
SCNI516	5	3	4	3	500	300	120
SCNI514	5	3	3	3	500	300	120
SCNI513	5	4	3	3	500	300	120
SCNI512	5	4	3	3.8	500	300	120

* films prepared with nitrogen flow in dispersion ring

Table 5-2: Deposition parameters of a second series of films.

Sample Label	SiH_4 flow (sccm)	CH_4 flow (sccm)	N_2 flow (sccm)	Ar flow (sccm)	T_{heater} (˚C)	Power (W)	t_{dep}
SCNI522	5	2	4	4	600	300	120
SCNI526	5	4	2	4	600	300	120
SCNI532	5	2	4	3	400	300	120
SCNI536	5	4	2	3	400	300	120
SCNI541	5	2	4	3	400	300	120
SCNI542	5	4	2	3	400	300	120
SCNI543	5	2	4	3	500	300	120
SCNI544	5	4	2	3	500	300	120
SCNI545	5	2	4	3	600	300	120
SCNI546	5	4	2	4	600	300	120
SCN01	5	1	3		500	300	120
SCN02	5	2	3		500	300	120
SCN03	5	3	3		500	300	120

The rationale behind choosing the deposition parameters above was based on using known parameters for depositing luminescent silicon nitride films (namely, 5 sccm silane and 4 sccm N_2) then gradually increasing the carbon-nitrogen ratio to determine what role carbon plays in the properties of the film. Given the dependency of the resulting film's composition on the total pressure, gas flow ratios, substrate heater temperature, and RF power, I chose to vary the sample composition primarily by altering the gas flows, one at a time, in increments of 1 sccm. This allows one to determine the differences between samples more easily, but it also means that there is no line on the Si-C-N phase diagram which can follow the gas flow ratios and simultaneously maintain other important deposition characteristics such as chamber pressure. This was deemed non-critical as the detailed relationship between film composition and gas flow rates, though obviously a positive correlation, is unknown. The first four films, SCNI505 to SCNI505c, were used predominantly to determine the effect of repositioning the nitrogen entry point into the chamber. Trying to minimize the presence of argon in the film, an unnecessary and complicating factor, SCNI505a was used as the benchmark for all subsequent depositions. The effect of changing substrate temperature was ventured into for the most nitrogen rich and most carbon rich films with a 90 s HF dip, SCNI52X and SCNI53X, as well as without an HF dip, SCNI54X. Samples SCN0X were deposited on fused quartz substrates for UV-Vis transmission measurements. The 60 min deposition time was assigned so that the films were thick enough to ease RBS/ERD measurements.

Annealing was done in 5% H_2 in N_2 (forming gas) as an attempt to reduce the number of dangling bonds in the film by hydrogen passivation. Some of my earlier work did demonstrate that the use of forming gas would significantly increase the fraction of hydrogen present in the film. The maximum anneal temperature of 1200˚C is simply the highest temperature the tube furnace used for annealing the films could generate. The minimum temperature of 300˚C was used since it became clear that subsequent reductions in minimum annealing temperature would not improve the luminescence.

Rutherford Backscattering and Elastic Recoil Detection

Results from RBS analysis done at the University of Western Ontario are presented in Figure 5-1 for samples SCNI516, SCNI514, SCNI513, and SCNI512. Experiments were performed at normal incidence, with 2 MeV $_4He^+$ ions, and detected at a scattering angle of 170˚. Compositional models neglect surface roughness and dual large angle scattering but include multiple small angle scattering. The inclusion of dual large angle scattering did not make a significant difference in the results but added a great deal of time to the fitting calculation. Energy calibration and the detector solid angle were determined through the use of an amorphized silicon wafer implanted with bismuth. Dosages were 5.0 µC and took over an hour to deliver. Significant beam damage was visible to the naked eye after the measurement with the most obvious damage falling on the AD and lower temperature annealed samples. The model structure consists of a single a-SiC_xN_y:H film on top of a very thick silicon substrate. Manual fitting was used to the best of my ability, then SIMNRA's built-in fitting program was used. The trendlines in Figure 5-1, (the thin lines) show that when the methane to nitrogen flow ratio is increased the silicon concentration increases while nitrogen content decreases and carbon content increases slowly. This is reasonable if the silane derived species are more reactive than their methane derived analogs (certainly true for silane and methane). Uncertainties in the fitting procedure are routinely <1% of the result for Si (i.e.± <1 at.%), but can be very high, around 40% for carbon (approximately ±4-8 at.% carbon) and nitrogen (±12 at.%). The high degree of uncertainty is a result of the carbon and nitrogen peaks lying on top of the silicon substrate background and their low Z value, which means that RBS is less sensitive to their presence. However, the fit error is not the same as the actual uncertainty in the measurement; assuming a good fit, the error in the measurement is the reciprocal of the square root of the number of counts associated with that element, $1/\sqrt{\#\, counts}$. Uncertainties calculated this way again result in <1 at.% for silicon, but only around 2 at.% for nitrogen and carbon. This quite low uncertainty is a consequence of the large doses used. The hydrogen content was used as a fitting parameter and varied widely, though it has been removed from the RBS compositions here. Analysis of the spectrum obtained from sample SCNI505a (not shown) resulted in a nonexistent carbon signal. Indeed, with the results of the TEM work to be reviewed later, where a clear carbon signal is obtained, this is known to be incorrect. The most likely explanation seems to be that the carbon signal is low enough to lie below the noise floor in the background spectrum, i.e., it is below the detection limit of the technique for this system. The rise in silicon content on the 2nd and 4th points is reasonable when keeping in mind that silane flow as a total fraction of gas flow is slightly higher for those samples.

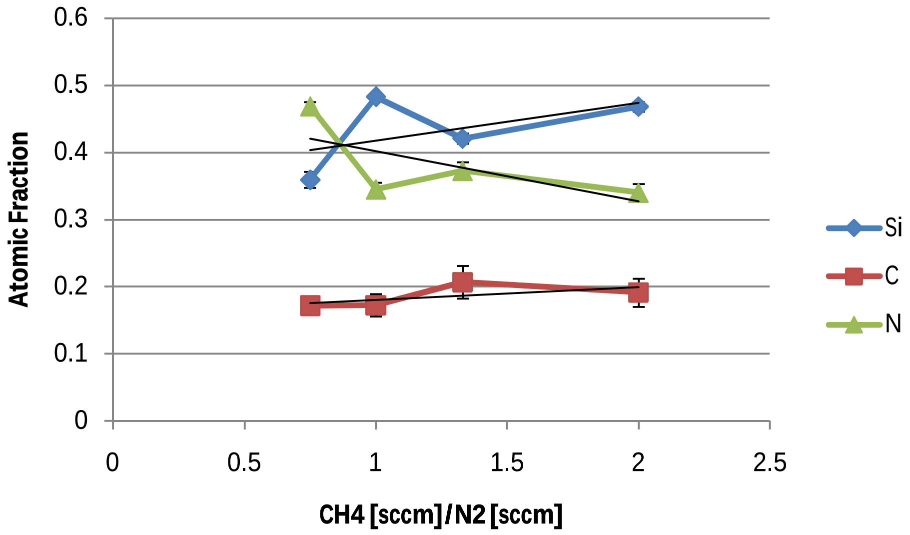

Figure 5-1:Elemental concentrations as a function of the methane to nitrogen gas flow ratios

In the taking of RBS spectra I found that it is good practice to avoid channelling effects through a random rotation of the sample. Channeling effects are supposedly beneficial in that they allow one to distinguish the peaks from the substrate more easily. However, they also prevent accurate assessment of the quality of the simulation. In order to take into account channelling effects, one typically adds a false amount of hydrogen to the silicon substrate, sometimes as much as 95%, for effective channelling. For example, in Figure 5-2 the results of both experiment and simulation are shown. The measurement where there was deliberate channelling has a smaller signal (implying greater experimental uncertainty), slightly better resolved elemental peaks, and a far poorer fit to the background, especially at low energies (i.e. low channel numbers). Even if one performs a simulation with the false substrate hydrogen content tuned to a particular elemental peak, the width of the peaks means that obtaining a good fit to the background remains impossible and calls into question the accuracy of the combined result. This is a typical result, which then often leaves the assessment of the fit quality up to human interpretation.

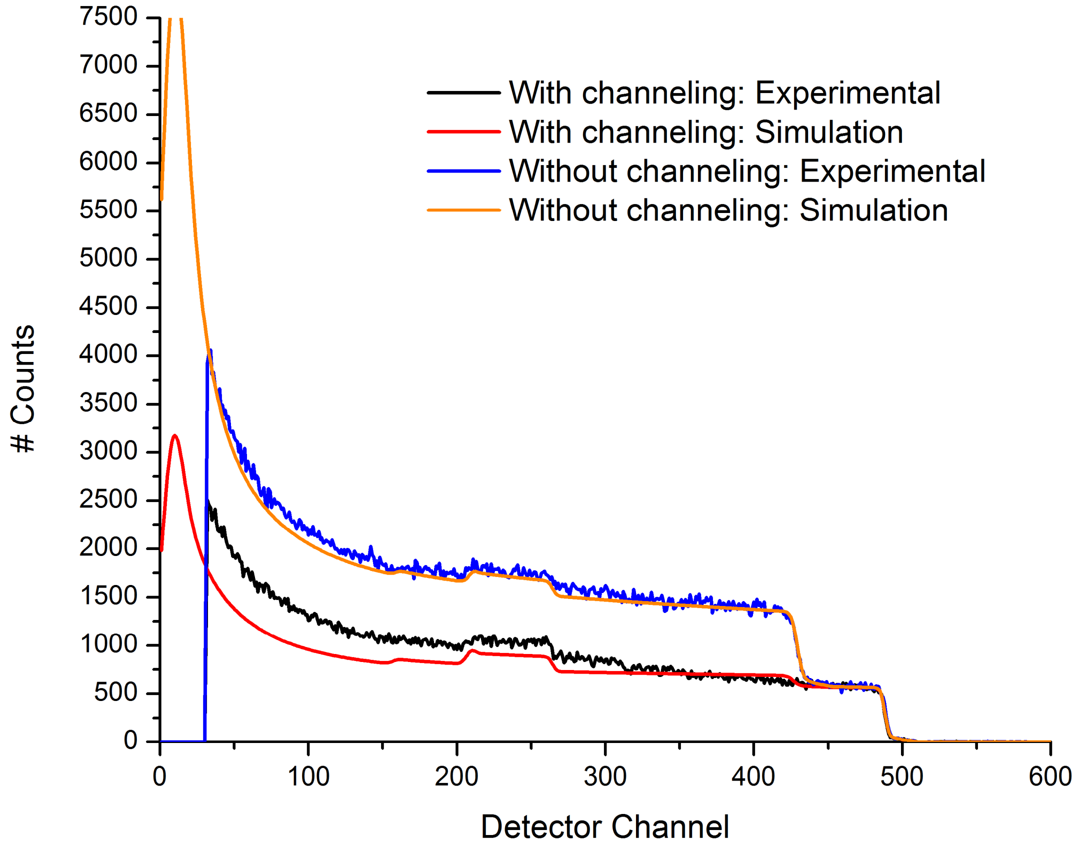

Figure 5-2: SCNI505b experimental RBS results and simulation with and without channelling.

ERD results from sample SCNI505b as a function of annealing temperature are shown in Figure 5-3. The measurements were taken with a $_4He^+$ beam, with energy of 1.6 MeV, at an incident angle 75˚C from the surface normal. The ERD simulation is performed similarly to that of the RBS spectrum though it takes as input for the film composition the results of the RBS analysis. The results of the ERD fitting are then fed back into the RBS fitting routine and the process repeats until the results of the two simulations agree to within a few atomic percent. However, this process means that film compositions are over-parameterized so fit results, while they tend to accumulate around a region, they never truly converge. The choice of which results to use is made by assuming that RBS legitimately measures the non-hydrogen elemental ratios, while ERD accurately determines the total amount of hydrogen. In film SCNI505b significant oxygen contamination is also present, greater than 13 at.% depending on the annealing temperature. It is the only sample considered where significant amounts of oxygen are present and it is also the only sample which saw a large argon flow (10 sccm). It is natural then to associate the oxygen contamination with the presence of argon, presumably the contamination occurs through a small leak in the gas delivery system, though the possibility of a contaminated argon cylinder cannot be ruled out. As expected, hydrogen is driven off at progressively higher rates as the annealing temperature is increased. This loss of hydrogen likely occurs at low temperatures as well, albeit at slow rates, and is thus a form of aging in the samples. No study of the effects of aging was performed in this thesis though it does serve as a possible explanation for the differences in hydrogen concentration between a film whose substrate had been pretreated with HF and one that had not. In comparing the AD sample of SCNI505b, with 18 at.% H with the SCNI54X series of films which were not cleaned in HF, one finds that there is much more hydrogen in the SCNI54X films, up to 40 at.%. The explanation for this is probably related to the presence of oxygen in SCNI505b as it possesses fewer bonding sites than nitrogen, carbon or silicon.

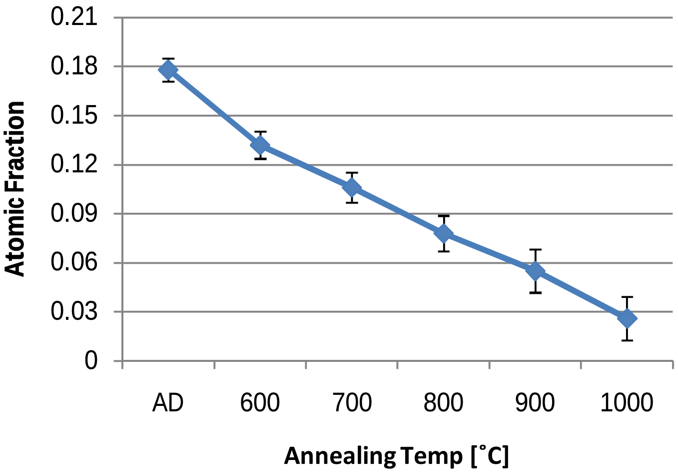

Figure 5-3: Hydrogen concentration as a function of annealing temperature in sample SCNI505b

The RBS and ERD results of the SCNI54X series of films are shown in Table 5-3. As expected, a higher methane gas flow results in a more carbon rich film and a higher nitrogen flow results in a higher nitrogen content. The samples, which were prepared with similar gas flow rates all possess similar ratios of silicon, carbon, and nitrogen even though they were deposited at substrate heater temperatures of 400, 500, and 600˚C. So, the substrate heater temperature only plays a minor role in determining film composition. Its greatest effect is the small reduction in hydrogen concentrations at higher deposition temperatures. This is to be expected as, referring to Figure 3-2 on page 31, we see that changing the substrate heater temperature by large amounts results in a much smaller change in the substrate surface temperature.

Table 5-3: Sample compositions for SCNI54X series films obtained by RBS and ERD.

Sample Label\Element	Silicon	Carbon	Nitrogen	Hydrogen	Substrate Heater Temp (˚C)
SCNI541	25	13	29	33	400
SCNI542	22	19	19	40	400
SCNI543	26	13	29	31	500
SCNI544	24	18	20	38	500
SCNI545	28	12	34	26	600
SCNI546	24	20	19	37	600

Ellipsometry

Ellipsometry was performed at the University of Western Ontario using an M3000 vaariable angle spectroscopic ellipsometer (VASE) made by J. A. Woollam company to determine thin film thicknesses and optical functions. Film thicknesses as a function of annealing temperature are shown in Table 5-4. Looking down the film column, the thickness of the solid film in the model, it is apparent that SCNI512 shrinks significantly more than SCNI505a. This can be attributed, at least in part to the desorption of hydrogen from the films. However, at higher temperatures very little hydrogen remains in the films. Thus, at least some of reduction in thickness is likely associated with structural relaxation of the film. For example, between SCNI512-a1000 and SCNI512a-1100 there is a 4nm reduction in thickness but extremely small amounts of hydrogen are present in either film. Surface roughness, estimated using the effective medium theory with 50% film and 50% void space, almost uniformly increases with annealing temperature. This is to be expected, as significant film reconstruction occurs at the elevated temperatures used in annealing. Indeed, this is the point of annealing: increased

Table 5-4: Film thickness and roughness values determined by ellipsometry simulations. Total is simply the sum of film and roughness thicknesses.

Label	Film (nm)	Roughness (nm)	Total (nm)
SCNI505a-AD	222	6	228
SCNI505a-600	224	5	229
SCNI505a-800	223	5	227
SCNI505a-900	218	5	223
SCNI505a-1000	217	5	222
SCNI505a-1100	218	7	225
SCNI512a-AD	176	4	181
SCNI512a-600	177	5	182
SCNI512a-700	173	5	179
SCNI512a-800	165	6	172
SCNI512a-900	163	7	170
SCNI512a-1000	161	7	168
SCNI512a-1100	156	8	164
SCNI505b-AD	255	5	261
SCNI505a-600	224	5	229
SCNI516-600	237	14	251
SCNI514-600	218	4	222
SCNI513-600	228	5	233
SCNI512-600	177	5	182

atom mobility coupled with the lack of stoichiometric compositions means a rougher surface is thermodynamically preferred. Also, because the hydrogen in the forming gas used as an annealing ambient can act as an etchant, the different etch rates of the different atomic species can lead to film roughening. Finally, increasing any of the gas flow rates increases growth rates, though not necessarily the surface roughness. The increase in film thickness associated with an increase of 1 sccm of nitrogen is much higher than that associated with an increase of 1 sccm of methane, from which I conclude that the sticking coefficient of the carbon containing reactants is less than that of the nitrogen reactants.

The uncertainty in ellipsometry measurements is difficult to assess. Like RBS, the analysis of ellipsometry data is based on simulating a model structure and varying parameters until a certain goodness of fit is obtained. Mean square errors obtained in this thesis were typically quite low, and the model structure is extremely similar to the actual structure, as can be seen in the TEM images. Ellipsometry is usually considered to have sub-nanometre accuracy, so I would feel confident in claiming an uncertainty of ±1-2nm. Of course, this is essentially an ad hoc judgement as TEM images were not taken for every film measured with ellipsometry and additionally, are of insufficient resolution to be taken as true values for comparison with the ellipsometry results.

Figure 5-4 shows the index of refraction for SCNI505a and SCNI505b before annealing. Both spectra are similarly shaped though SCNI505b's index is much lower than SCNI505a's index and is much lower than the typical spectrum found for silicon nitride due to the influence of hydrogen and/or oxygen. At the short wavelength limit of the measurement the refractive index is falling rapidly following the bandgap absorption at even higher energies. Each spectrum possesses slightly more linear regions than the KKR transforms of the Lorentzian or Gaussian curves would lead one to expect, leading to an implication that there are absorption mechanisms between 200 and 400nms. However, their extremely small size prevents further identification. Only one shoulder, around 365 nm in SCNI505b, can be clearly distinguished. There is an additional peak in SCNI505b, at around 625 nm, and in SCNI505a at around 940 nm. Finally, there is a rise in index in SCNI505b at long wavelengths >1300 nm. This anomalous dispersion has been reported in the literature, [73], but no explanation for it has been given. The possibility of modeling error cannot be ruled out. Possible explanations include the traditional NIR absorption mechanism of the excitation of higher harmonics of the vibrational modes, free carrier absorption, as well as nanocluster/defect excitation. The only difference between the two films' deposition parameters is the flow rate of argon through the plasma chamber: 10 sccm for SCNI505b versus 3 sccm for SCNI505a, with the attendant oxygen contamination and reduction in hydrogen content. So, the anomalous dispersion seems unlikely to be related to the presence of hydrogen in the film. The critical point made by Figure 5-4 is to demonstrate the clear effect of oxygen on the refractive index (lowering it as a whole), made possible by the increased Ar flow and justifying its minimization in all future depositions.

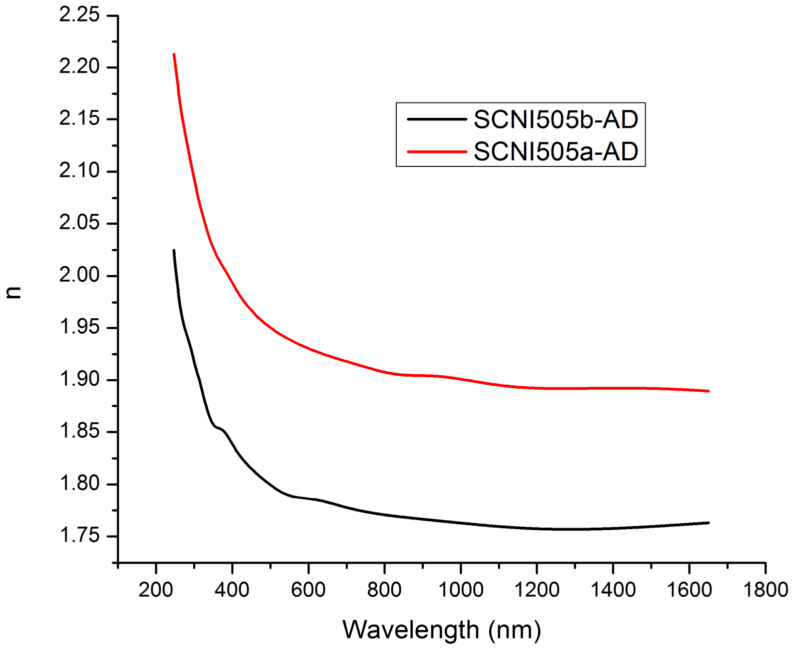

Figure 5-4: Refractive index for SCNI505a and SCNI505b.

Figure 5-5 shows the refractive indices as determined by ellipsometry for several films with a range of compositions (refer back to Figure 5-1 and Table 5-1). Features appear sporadically, though the anomalous dispersion region seems more common in these samples, which have been annealed at 600˚C, than in the as-deposited films. Figure 5-5 makes it clear that the amount of silicon present in the film plays a critical role in the determination of the optical constants with the carbon and nitrogen concentration being less important. For instance, SCNI505a, which has the most nitrogen and least carbon of all the films, does not have the lowest index due to the increased proportion of silicon. SCNI516 has the lowest index as not only does it have high nitrogen content, but also the silicon content is much lower. This serves to reinforce the message of the ion beam measurements and lends credibility to the modeling process used. It also highlights the sensitivity of these films to deposition conditions and demonstrates that a finer grained approach to an analysis of compositional measurements could be useful.

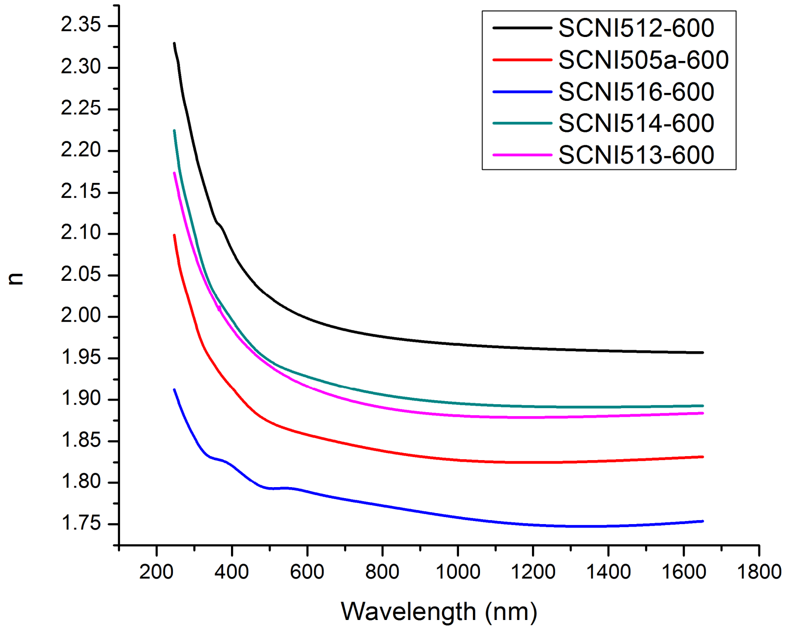

Figure 5-5: Refractive index of SCNI5XX films with various compositions (see Table 5-1).

Figure 5-6 presents refractive indices of the as-deposited films and after annealing at 700 and 1000˚C, as determined by spectroscopic ellipsometry . These curves were chosen for clarity as they are well separated on the plot. As well, these are the only two samples for which a complete set of ellipsometry data was obtained. We see a clear difference between films with higher nitrogen content (e.g. SCNI505a) and higher carbon content (e.g. SCNI512). The increase in index with annealing is what one normally expects for hydrogenated films: the hydrogen is driven off leading to densification and hence a higher index. However, the nitrogen rich film's index instead decreases to lower values. This cannot be explained through hydrogen desorption. The most likely explanation is the formation of voids which have also been observed experimentally.

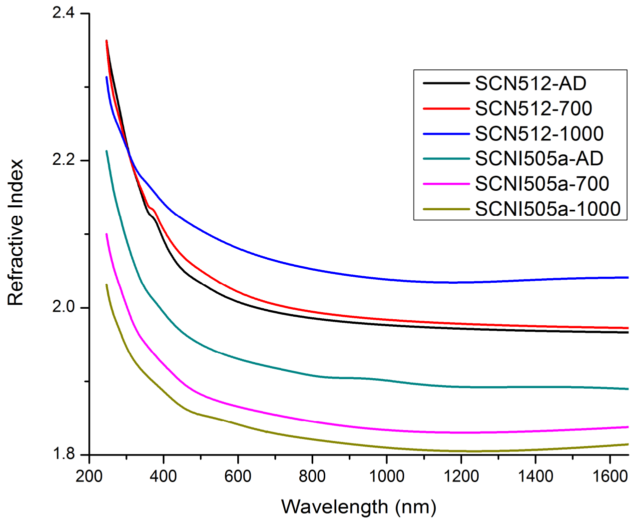

Figure 5-6: Refractive index obtained by ellipsometry of samples SCNI505a and SCNI512 and the dependence upon annealing.

Finally, we consider these two samples' extinction coefficients in Figure 5-7. Here the features are more clearly defined, particularly the small peak near 365nm, and the peak near 900nm in the refractive index of film SCNI505a as deposited. In both films the extinction coefficient increases as annealing temperature is increased. For SCNI505a the peak near 365 nm begins to disappear as annealing temperature increases. This is true for SCNI512 also though the peak reduction begins later and progresses faster. This is an indication that the presence of carbon, which bonds to nitrogen more strongly than silicon, has a stabilizing effect on film structure. Thus, more energy must be supplied to the more carbon rich material before its structure will relax. There is an additional absorption peak in SCNI512 which is not present in the annealed films that could have a similar origin to the peak at 900 nm in SCNI505a. It should also be noted that in the more nitrogen rich films the anomalous dispersion at long wavelengths is present but not in the more carbon rich film. It is unlikely then that it is related to either carbon or hydrogen content.

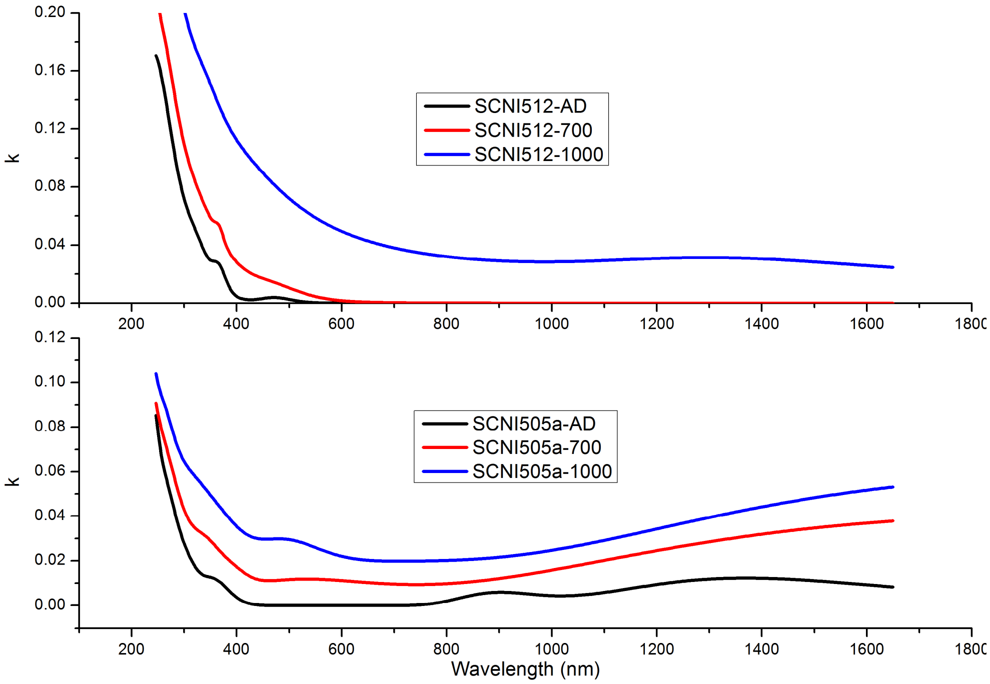

Figure 5-7: Extinction coefficients of SCNI505a and SCNI512. Plotted on separate axes for clarity.

Photoluminescence

Figure 5-8 shows the PL spectra for the as-deposited films of the series SCNI505X. The only relevant changes among the four films are the nitrogen inlet position and the flow rate of excess argon. Clearly, when the nitrogen is flowed through the dispersion ring (samples SCNI505 and SCNI505c) only minimal luminescence is obtained, whereas flowing it through the plasma chamber results in an intense signal. As has been mentioned earlier, this is attributed to an increased number of excited N_2^* species, a critical species for nitride film growth, since it is reasonable to assume that excitation efficiency is higher within a high energy density plasma. The difference between SCNI505a and SCNI505b is mostly caused by the difference in thickness between the two films, which itself is caused by the excess Ar flow acting as a carrier gas for N_2^* molecules, promoting film growth.

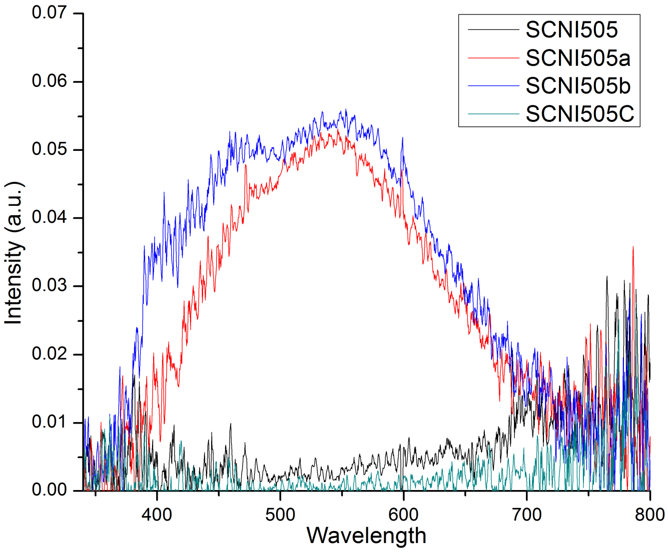

Figure 5-8: PL intensity in the as-deposited films for each combination of nitrogen inflow position (plasma chamber or dispersion ring), and argon flow rate (10sccm or <4sccm).

The spectral shape is more easily seen in Figure 5-9, though it is common across all SiC_xN_y samples with one main broad peak with a smaller shoulder on the high energy side. The wavelength of the peaks shifts with film composition as can be seen from Figure 5-9 the slope of the line connecting the bolded PL signals. The appearance of a shoulder at approximately 400nm is likely an instrumental artefact as this is where the detector begins to saturate. The general trend with increasing carbon content is that PL intensity decreases and the main broad peak shifts to longer wavelength, though the shoulder exhibits little to no shift. This is true as well when comparing directly a SiN_x

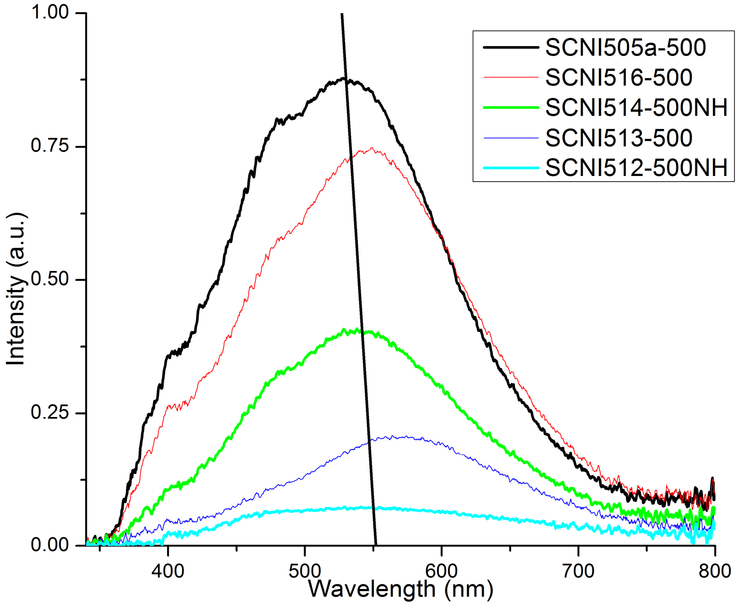

Figure 5-9: Room temperature PL for samples annealed at 500˚C as carbon flow replaces nitrogen. Bolded curves represent samples that were prepared at the same total flow rates. The superimposed straight line shows some shift in peak wavelength across the bolded curves.

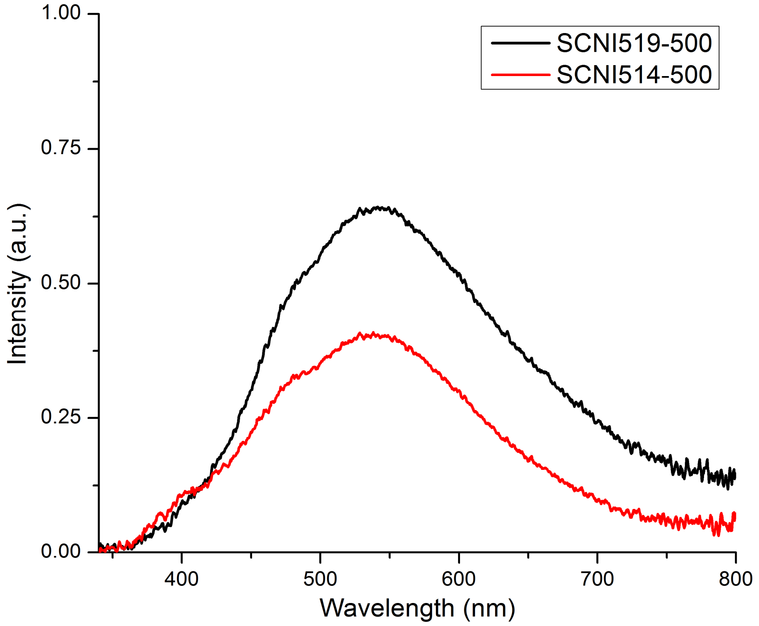

Figure 5-10: Direct comparison of PL showing effects of the inclusion of carbon (SCNI514) into an otherwise identically prepared film (SCNI519).

film and a SiC_xN_y film, as is done in Figure 5-10, where the only difference in the deposition parameters was the methane flow rate. Clearly, the influence of carbon in this structural regime is to reduce the density of luminescent clusters or defects, or to promote the formation of secondary absorbing sites, without playing a part in the generation of significant amounts of light. This effect is seen in particular for the shoulder which has essentially disappeared at the higher carbon concentrations. The overall similarity between the two spectra leads me to believe that the structure of these films is fundamentally similar to SiN_x, though possessing significant carbon contamination. However, one of the last films deposited, SCNI511, shows a different behaviour. As can be seen in Figure 5-11, doubling the methane flow from SCNI512 actually resulted in more than doubling the peak luminescent intensity, as well as a significant redshift of approximately 100 nm. This pattern breaking sample is an excellent sign for future research as it implies that entrance into a new structural regime, possibly that of SiC_xN_y, has begun to occur. That nitrogen plays a key role in this new regime seems likely as films deposited without nitrogen gas flow exhibited little to no luminescence, though their luminescence did possess a red color similar to SCNI519.

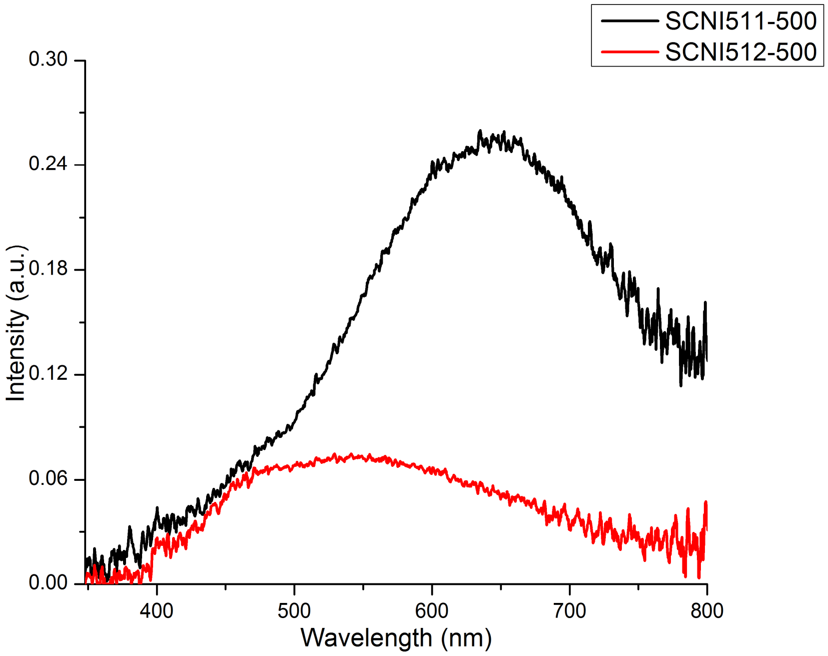

Figure 5-11: PL spectra of SCNI512, and SCNI511 which was deposited usin twice the methane flow.

Figure 5-12, for HF dipped samples, and Figure 5-13, for undipped samples, show PL spectra for films deposited at different substrate heater temperatures after annealing at 600°C. The pre-treated samples which are more heavily carbon rich, the lower three curves in Figure 5-12, have much weaker luminescence at 500 and 600°C than at 400°C. However this is not the case in the undipped samples where the film deposited at a substrate heater temperature of 600°C displays more intense luminescence than the film

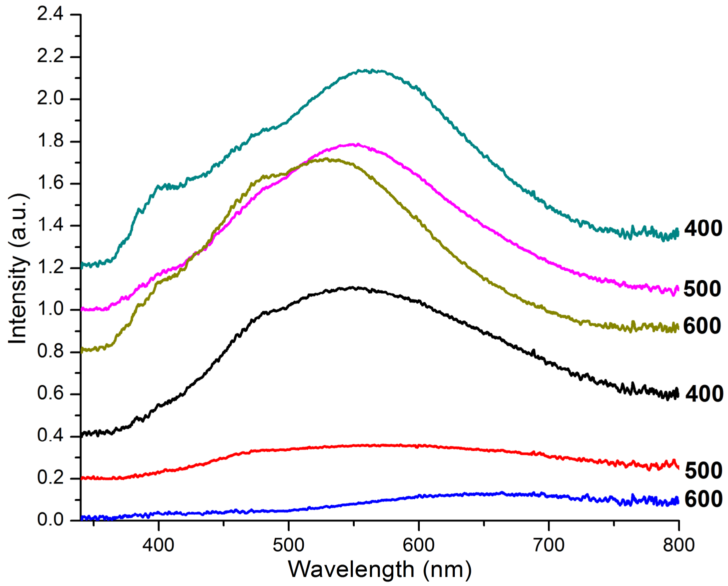

Figure 5-12: PL spectra of HF dipped nitrogen-rich (top curves) and carbon-rich (bottom curves) samples deposited at the indicated substrate heater temperature and annealed at 600°C. Curves have been displaced for clarity.

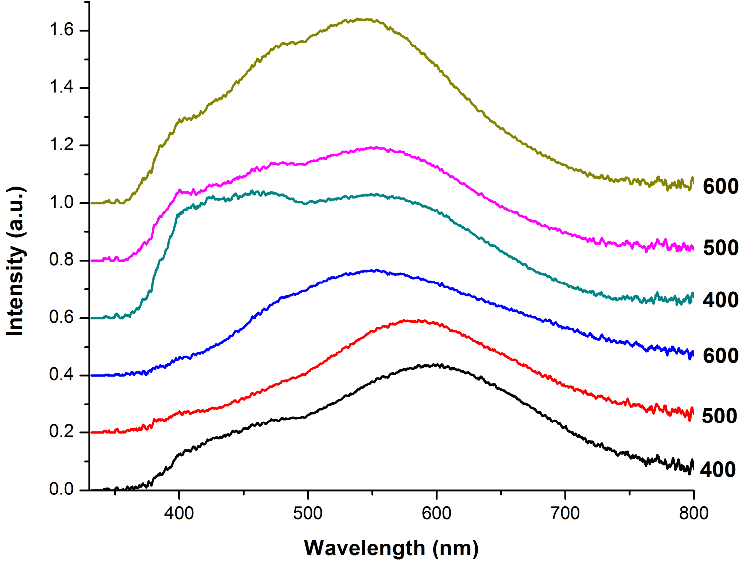

Figure 5-13: Photoluminescence spectra of undipped nitrogen-rich (top curves) and carbon-rich (bottom curves) samples deposited at the indicated substrate heater temperature and annealed at 600°C. Curves have been displaced for clarity.

deposited at a substrate heater temperature of 500°C. So, the interface between the silicon substrate and/or the native oxide and the film can play an important role in determining the luminescent properties. This leads to one of two conclusions: that the silicon substrate-native oxide-film system displays an intense luminescence, or that the deposition reactions of the films are altered. The first explanation is not particularly satisfying as the first few layers of the native oxide, which grow very rapidly, are unavoidable with the equipment available. Thus, the thickness of the native oxide layer is uncontrolled and varies randomly from deposition to deposition. If it was the dominant factor then the trend towards lower intensity emission with increasing carbon content should not exist. Modulation of the emission by the film seems unlikely as the extinction coefficient of the film is very low in many films which exhibit this behaviour. Furthermore, if the luminescence was originating within the native oxide, luminescence at longer wavelengths would be expected, which is not the case. This does not rule out the possibility of dopant diffusion from the substrate to the film playing a role, and indeed could explain the difference between the dipped and undipped samples, though no evidence for this was obtained from the RBS measurements. The second explanation is not much better as it would entail exceptionally long interaction lengths for the atoms in the native oxide. There is also some additional luminescence in lower temperature depositions at short wavelengths. This is most clearly seen in the nitrogen rich sample deposited at 400°C substrate heater temperature in Figure 5-13. There are several possible origins for this luminescence- it could be a tail from a luminescent peak beyond the range of the detector, it could be related to defect levels since no relevant silicon nitride or silicon carbon nitride material possesses a bandgap at these energies, or it could be through a bandgap of SiC related structures. The peak luminescence in the carbon-rich undipped samples shifts slightly to shorter wavelengths at higher deposition temperatures, but in the dipped samples a shift to much longer wavelengths occurs. This shifting of wavelength could prove to be of use when implementing a device based on SiC_xN_y and is the type of behaviour we can expect of SiC_xN_y due to its large parameter space.

Looking at the nitrogen-rich film's spectra, the upper curves in both figures, there is a shift to shorter wavelengths with higher deposition temperatures, as well as a reduction in the intensity of the short-wavelength shoulder. This is a shift in the opposite direction from that which would be expected if the main broad peak was associated with quantum confined nanocluster luminescence. Again, particularly in the undipped samples, there is some additional signal at the short end of the measured wavelength region of unknown origin. PL peak intensities remain similar though SCNI505a-600, the pink curve in Figure 5-12, has slightly lower peak intensity than films deposited at both higher and lower temperatures. Unlike in the carbon-rich films more luminescence is observed from the dipped samples than the undipped samples.

Also of interest is where the luminescent intensity is a maximum with respect to annealing temperature. Lower temperature processing is preferred for microelectronics applications. In silicon nitride a lower temperature is often found to be optimum; Dal Negro *et al.*, [24], found that the luminescence peaked at an annealing temperature around 700˚C. In the films prepared for this thesis the maximum luminescence is usually obtained for annealing temperatures between 500 and 700˚C. The shift in peak wavelength is generally towards longer wavelengths as annealing temperature is increased. In the more carbon-rich films, such as SCNI544 in Figure 5-14, we see that the luminescence has completely died out after annealing at 900˚C, though the more nitrogen-rich films, like SCNI543 in Figure 5-15, are able to maintain the luminescent structures at higher annealing temperatures.

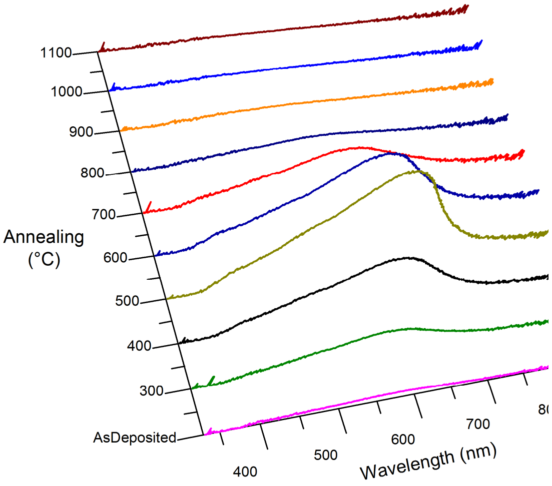

Figure 5-14: PL intensity at each annealing temperature for SCNI544, a carbon rich sample prepared at 500C heater temperature.

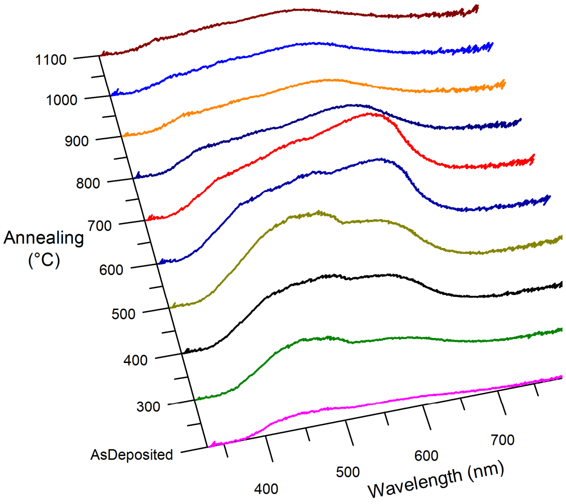

Figure 5-15: PL intensity at each annealing temperature for SCNI543, a nitrogen rich sample prepared at 500C substrate heater temperature.

The rate of decay of the luminescence is important when pulsing the light source at high speed; for instance in a microelectronics application, as it determines the time that must be waited before it can be switched back on. Some preliminary time dependent PL measurements were taken in conjunction with Group IV Semiconductor, an example of which is shown in Figure 5-16 for sample SCNI544 when annealed at 600˚C. The stretched exponential, shown in red, is fitted to the experimental data beginning a few points past the peak, where it is more clear that the laser pulse has ended. The time constants obtained for these stretched exponentials range from 7.9 ns at room temperature for sample SCNI543, to 3.0 ns after annealing at 1000˚C for the same sample at 158K. 3.0 ns is at the bounds of the equipment’s measurement capabilities. The time constant

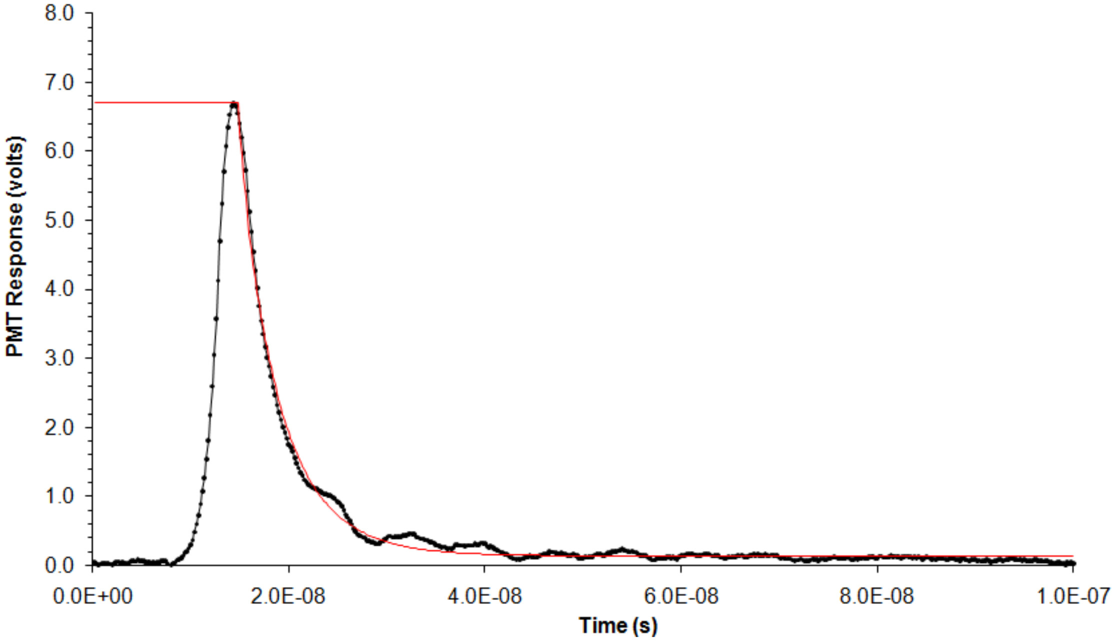

Figure 5-16: Time dependent PL and exponential fit of sample SCNI544 after annealing at 600˚C.

for SCNI543 when annealed at 600˚C is 4.3 ns whereas for SCNI544 it is only 3.9 ns, which could mean that an effect of carbon is to reduce the decay time. However, the statistical significance of this difference is uncertain and trying to claim a trend from two data points is questionable at best. Slightly more reliable is the trend towards longer decay times with increasing annealing temperature. For SCNI543 decay times of 4.3, 3.9, 6.6, 7.1 ns are obtained after annealing at 600, 700, 800, and 1000˚C respectively. The longer decay time for the sample annealed at 600˚C could be a result of a change in the dominant mechanism of luminescence, i.e. defect to nanocluster, or an experimental anomaly. The two cannot be distinguished due to the lack of comprehensive data. Similarly, the increase in decay time from 3.0 ns at 158K to 3.1 ns at 134K cannot be ascribed to a different characteristic of the luminescence or a limitation of the experimental equipment due to a lack of data. Essentially, the results of the time dependent PL are tantalizing in the information they contain but the few measurements made prevent firm conclusions from being drawn.

Fourier Transform Infrared Spectroscopy

A typical spectrum obtained through FTIR spectroscopy consists of some low wavenumber structure around 450cm^{-1}, a main peak with many components around 900 cm^{-1}, and then some smaller peaks at higher wavenumbers, each representing the excitation of a vibrational mode in the film. Prior to analysis a large instrumental background was removed by using a so-called “rubber band method”. This consists of finding the local minima in the spectrum, fitting these points with polynomials, and subtracting off the polynomial curves in an iterative manner to eliminate the background [89]. While necessary, this process has a tendency to exaggerate the sharpness of the different absorption peaks. Peak assignments found in the literature are quoted in Table 5-5 along with the approximate center wavenumbers found through fitting of Gaussian curves for the SCNI54X series of films in parentheses. Gaussian fits performed using the graphing program Origin are shown in Figure 5-17 and Figure 5-18. The dominant absorption mechanism is the Si-N stretching mode near 900 cm^{-1}, with sizable overlap peaks representing the Si-C stretching mode absorption at lower wavenumbers and what is most likely a Si-O stretching peak at higher wavenumbers. Though there is no oxygen present in these films according to the RBS results, the XAS possesses a well known fingerprint of silicon-oxygen bonding. Likely this means that the oxygen content in the films results in a signal below the noise floor for RBS. Alternatively, it could be that the aging process involves the incorporation of oxygen as well, meaning more oxygen was present at the time of the FTIR measurements than during the RBS measurements. The increase in the Si-C stretching mode peak seen in Figure 5-18 casts a certain degree of doubt onto the fitting procedure as this directly conflicts with the expectation of carbon substituting for silicon in the formation of SiC_xN_y. The fit is self-consistent as it also simultaneously assigns increased relative amplitude to the Si-CH_3 bending mode. Also, this analysis neglects the possibility of artefacts introduced by the background subtraction process. In short, while informative, a lack of confidence in the results of the fitting procedure, coupled with the IR insensitivity of homonuclear bonds, means the main peak of the IR absorbance spectrum cannot be used to provide definitive bonding arrangements.

Table 5-5: Vibrational mode absorption wavenumbers [90].

Peak Position (cm^{-1})	Mode
≈462 (450)	Si-N rocking
≈680 (700)	Si-H rocking, wagging
≈800 (831)	SiC stretching, wagging
≈905 (920)	SiN stretching
≈1030 (1015)	SiO stretching/C-N wagging/Si-CH_x-Si bending
≈1170 (1145)	N-H_x bending
≈1260 (1250)	Si-CH_3 bending
≈ 1600 (1500)	N-H_2 wagging
≈ 2170 (2125)	C-N stretching
≈ 2928 (2800)	C-H stretching
≈ 3356 (3300)	N-H stretching

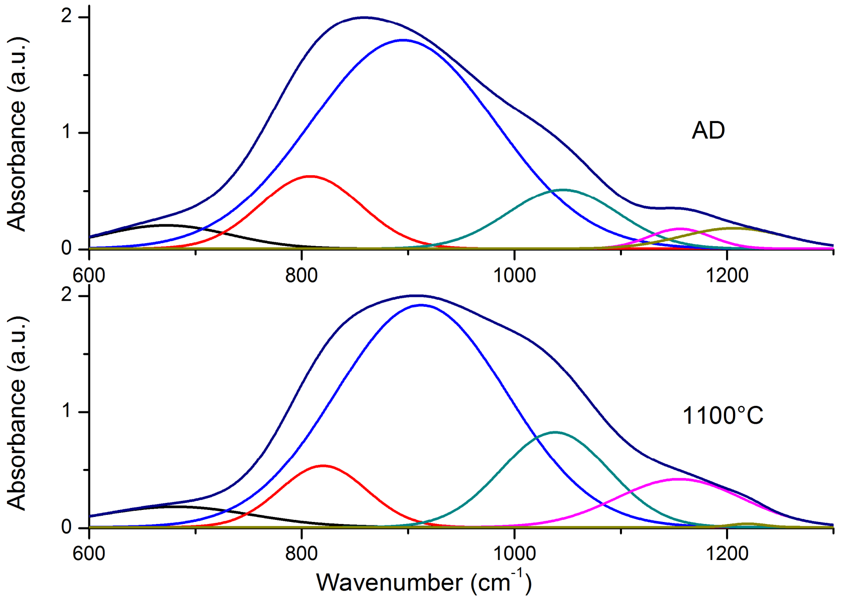

Figure 5-17: Gaussian fit of the FTIR absorbance spectrum of SCNI543 near 900 cm^{-1}.

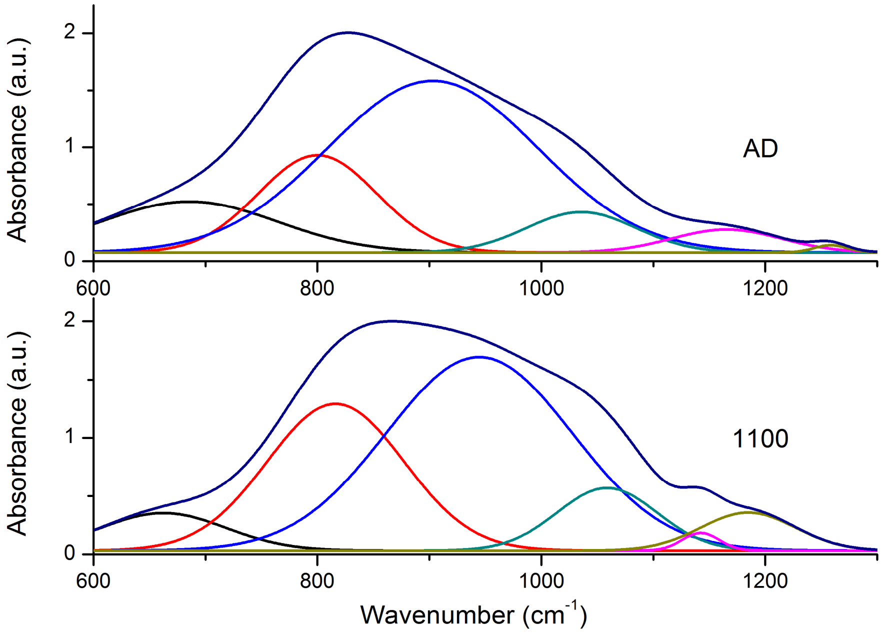

Figure 5-18: Gaussian fit of the FTIR absorbance spectrum of SCNI544 near 900 cm^{-1}.

Figure 5-19 and Figure 5-20 show the normalized absorbance curves of samples SCNI543 and SCNI544 respectively, as-deposited and after annealing. The main peak tends to broaden towards longer wavenumbers, which would be consistent with increased oxygen contamination occurring during the annealing process. In both cases the stretching modes at high wavenumber decrease with annealing, which is consistent with the outgassing of hydrogen. Surprisingly though, SCNI543, which has a higher nitrogen content, maintains its hydrogen bonds through higher temperature anneals than SCNI544. A similar behaviour occurs in the C-N stretching bond absorption, but there is only a small decrease in the Si-H wagging absorption at 680 cm^{-1} which seems to be more reliable than the other components of the main peak due to the above mentioned fitting difficulties. If one looks more closely at the N-H stretching peak one can note a change in shape with annealing from a symmetric to an asymmetric stretch. The relative heights of the symmetric and asymmetric modes remain similar until approximately 600˚C where the importance of the asymmetric stretching mode begins to increase. The asymmetric stretch occurs when the atoms the nitrogen is bonded to have different masses. Thus after having lost a single hydrogen atom all other bonding possibilities result in an asymmetric stretch. Whether it is a dangling bond left behind which serves to quench the luminescence or whether it is that a nitrogen atom bonded to two hydrogen atoms that serves as the main luminescent defect cannot be determined at this point.

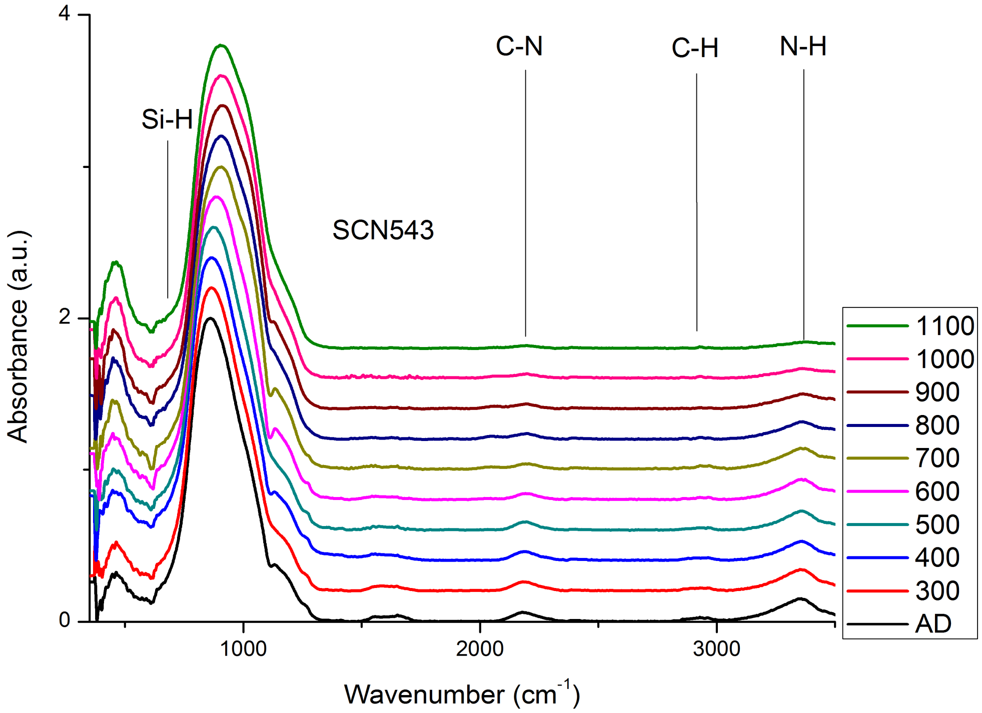

Figure 5-19: Normalized absorbance spectrum of SCNI543 with increasing annealing temperature. Curves offset for clarity.

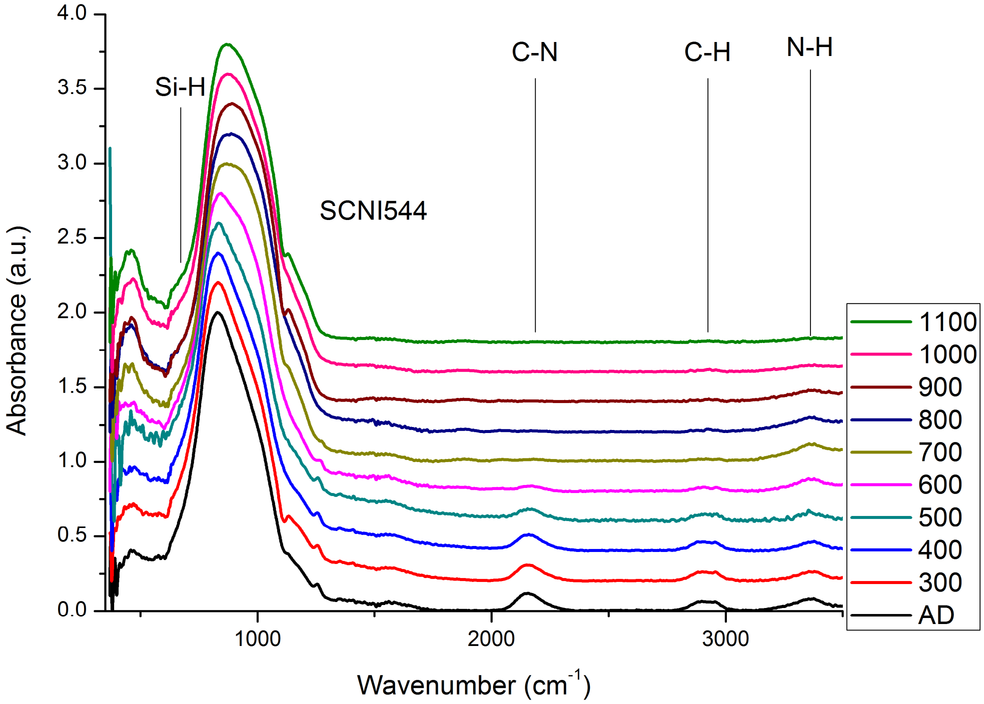

Figure 5-20: Normalized absorbance spectrum of SCNI544 with increasing annealing temperature. Curves offset for clarity.

Ultraviolet-visible Transmission Spectroscopy

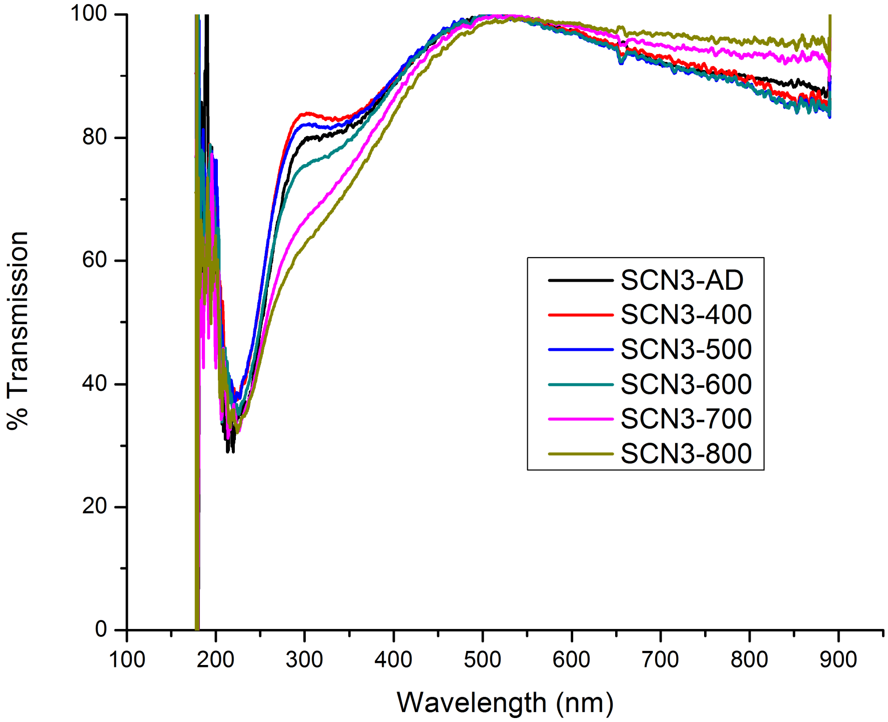

Figure 5-21: UV-Vis transmission spectra for sample SCN3 at various annealing temperatures.

Figure 5-21 shows the normalized % transmission versus wavelength for sample SCN3 at various annealing temperatures. The peak at the far left around 175 nm cannot be attributed to a physical characteristic as this is very close to the edge of the detectors range. Measurement points are taken at a fixed interval of energy. So, when converting the spectrum from energy to wavelength, the change in wavelength between points at the highest energies is smaller than at lower energies. This means that the number of points in any range on the graph decreases towards longer wavelength and could account for the more jagged appearance of the signal at long wavelengths. As with the as-deposited film (shown in black), there are clearly two absorption regimes, seen at approximately 250 nm and 400 nm. As well, there is increasing absorption towards shorter wavelengths, which lends credibility to the trend in the extinction coefficient found during the modelling of the ellipsometry data. Though the curves are most separated in the data for this sample the behaviour is the same for all three samples: the absorption at 250 nm decreases immediately upon annealing, and then begins to increase as the annealing temperature is increased whereas the reverse happens for the long wavelength absorption. It should be noted that these curves have been normalized to their highest point past 200 nm, typically around 500 nm. However, annealing results in only slight differences in transmissivity with the greatest change being a reduction at the higher annealing temperatures.

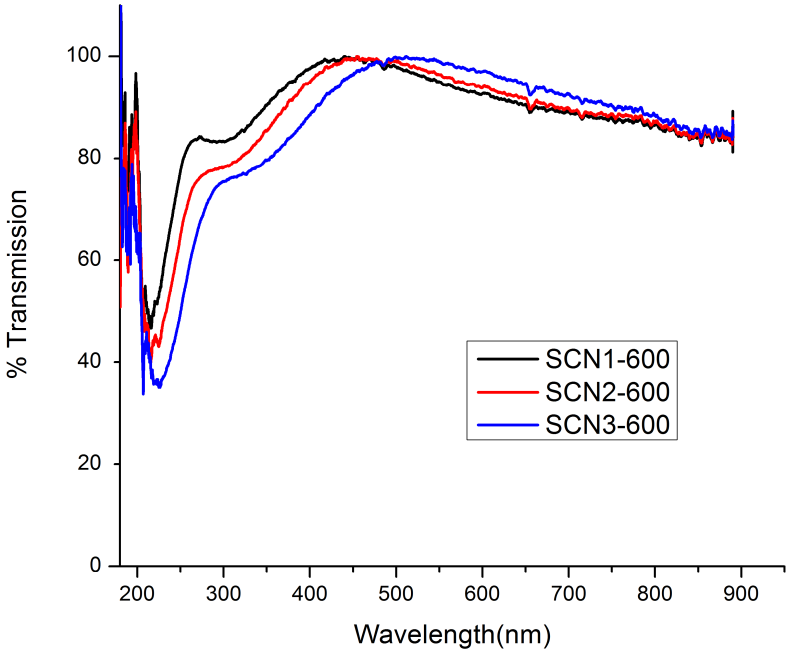

Figure 5-22: UV-Vis transmission spectra showing the changes as carbon content increases.

In Figure 5-22 three transmission spectra are shown, corresponding to a 600˚C anneal for each of the three samples. It is evident that the transmission maximum shifts to longer wavelengths, as do the higher energy absorption peaks. Referring to Figure 5-23, it is seen from the photoluminescence of a similar film (the only difference being the substrate material) that the luminescence peak corresponds to a region with very low absorption. The consequence of this is that attempting to generate stimulated emission in the film would be very difficult. Furthermore, while in Figure 5-23 it could be assumed that increasing the carbon content of the films could result in a shift of the absorption peaks to such an extent that it overlaps strongly with the region of efficient luminescence, it was seen when discussing the photoluminescence data that additional carbon also results in a shift of the peak photoluminescence intensity. This implies that the absorption mechanism at around 300 nm is in fact not a radiative centre. This is a large blow to the possibility of developing a practical device from SiC_xN_y with compositions similar to those of SCNI505a and SCNI512, however, films more similar to SCNI511 may possess a different structure where stimulated emission is possible.

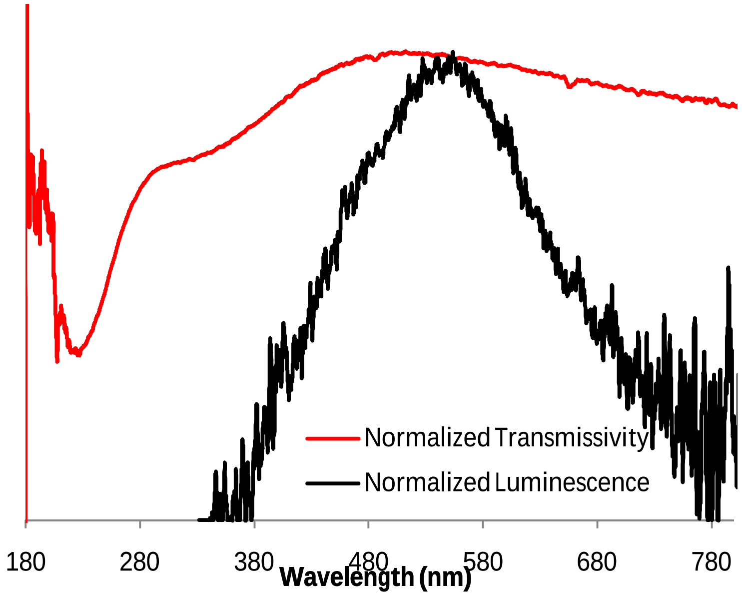

Figure 5-23: Normalized UV-Vis spectrum of sample SCN3 and normalized PL spectrum of SCNI514.

X-ray absorption spectroscopy

Silicon L edge data taken at the Canadian Light Source was obtained from the series of undipped samples which had been annealed at temperatures between 600 and 1200˚C, as well as on the as-deposited sample. A plot of the fluorescence yield is presented in Figure 5-24. Upon comparison of these spectra with those found in [26] no new structural features are found. That is to say, there is no evidence of silicon-carbon bonding in these films under X-ray absorption. This contradicts the results of the FTIR analysis (the fitting procedure produced sizable peaks associated with Si-C vibrational modes). This is interesting, though entirely expected from the literature, as it requires a reinterpretation of the infrared absorption, and shows the inadequacy of the Gaussian fitting procedure that has been used.

However, that is not to say that the carbon plays no role in the development of the film structure (as we have seen from TEM results). The two peaks at approximately 155 and 160 eV occur in the EXAFS region and could correspond to carbon and nitrogen atoms respectively, that are near the silicon atoms, though not necessarily chemically important. The rationale is that the peak near 155eV gradually decreases in intensity whereas the peak at 160 eV increases. This could reasonably correspond to the diffusion of silicon atoms away from the more carbon rich clusters evidenced in TEM, though this explanation is tenuous at best. As well, the films in [26] evidenced a structural breakdown upon annealing at 1200˚C, indicated by a sudden increase in the amount of silicon-silicon bonding at 99.7 eV that is not present here, likely owing to the favourable thermal properties of the carbon/carbon nitride cluster formation.

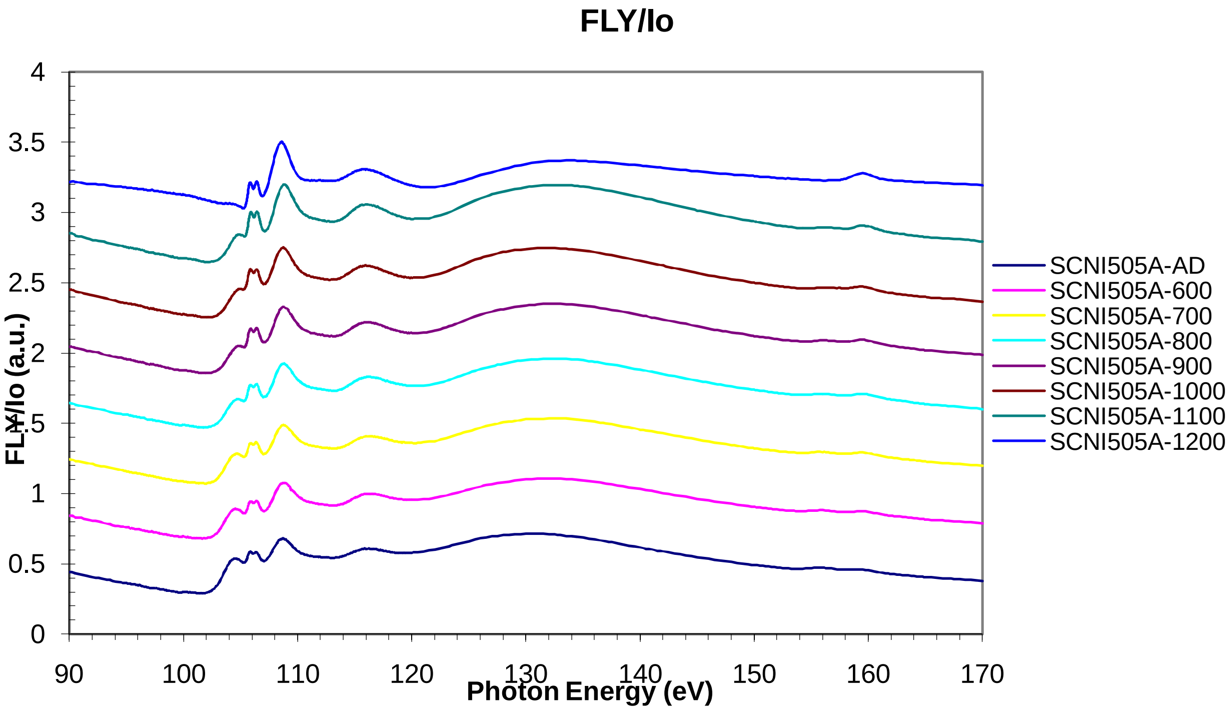

Figure 5-24: Silicon L-edge spectra of sample SCNI505a at various annealing temperatures.

Transmission Electron Microscopy

After some initial TEM work done on the CM12 to determine the suitability of a given prepared sample for high resolution imaging, bright field imaging was performed on the JEOL 2010F. Figure 5-25 shows relatively low magnification images of large areas of film with the silicon substrates being the dark regions, the less dense and hence lighter colored film, and the least dense, essentially transparent epoxy. From the ellipsometry results it was seen that growth rates depend on the gas flow ratios, gas inlet positions, and deposition temperatures. While the possibility of methane acting as an etchant, as was assumed in [91], can affect growth rates and film structure/morphology, the extremely smooth, high quality films produced in this thesis as evidenced by the TEM images demonstrate that this is not occurring at a significant rate. A few randomly selected samples were examined using an atomic force microscope but other than the influence of what is assumed to be dust particles, they remained smooth and relatively flat down to the limits of the AFM's resolution over a wide area.

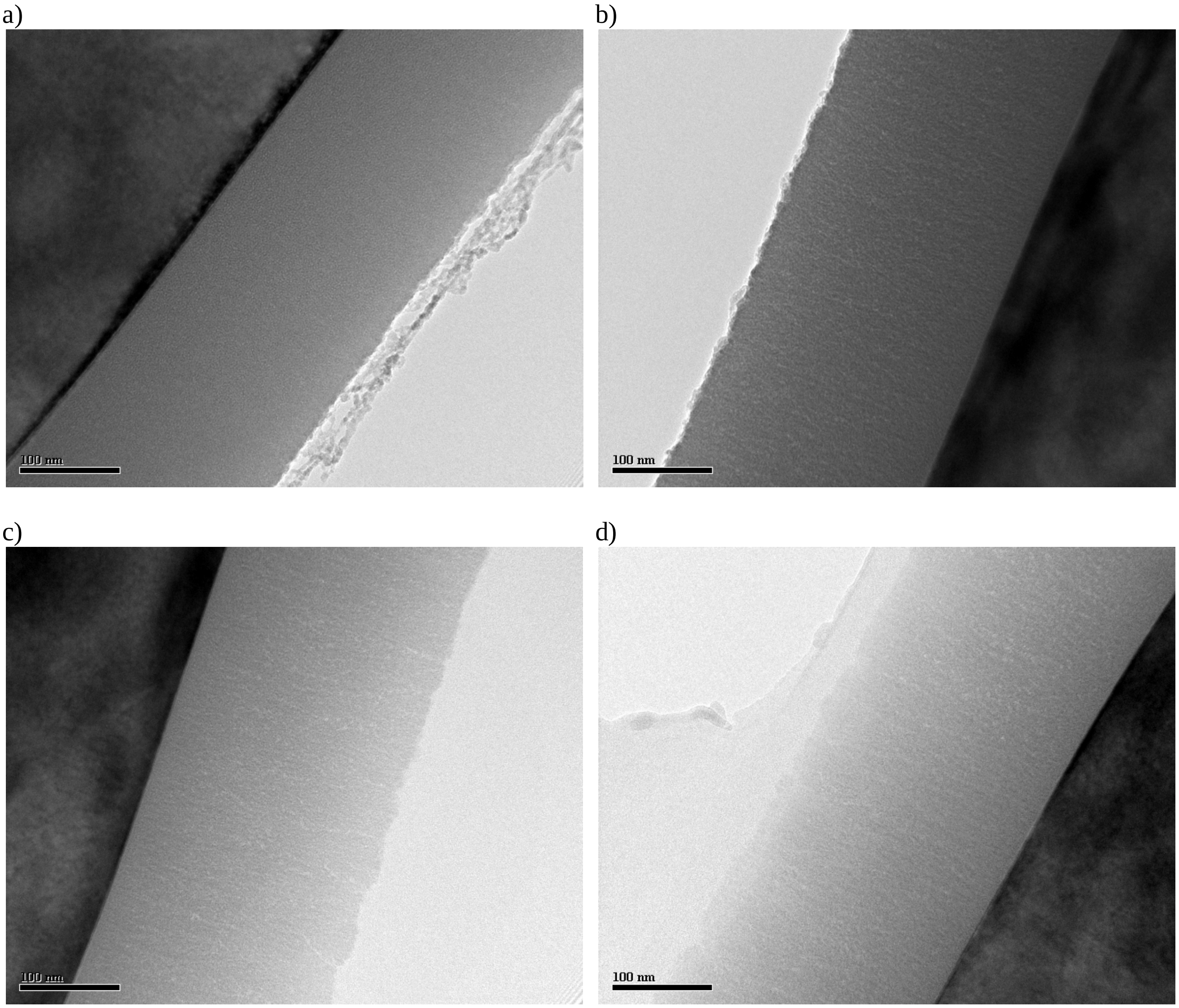

Figure 5-25: Bright Field TEM of SCNI505a a) as-deposited, b) 400˚C, c) 500˚C, and d) 600˚C annealed films.

The films are of extremely uniform thickness with low surface roughness, and little densification with annealing is evident, in agreement with the ellipsometry results.

Low density regions can be seen in the annealed samples (the lighter colored striations running perpendicular to the substrate), but not in the as-deposited sample, thus eliminating as the source of these striations, beam damage occurring during the sample preparation process. Strain relaxation, outgassing, or chemical structure changes could all account for the appearance of these striations. Any more precise difference between the films is not obvious at this magnification. At higher resolution, as seen in Figure 5-26, some evidence of extremely small nanocrystalline regions is observed. However, the extremely small size (some as small as 1 nm^2 and none with areas greater than 5 nm^2 at the lower anneal temperatures) calls into question the suitability of the term crystalline. At 900˚C (Figure 5-26, image d) an extremely large, nearly crystalline region is observed in the film, possibly the result of patterning off of the substrate rather than an example of self-assembled growth. The misalignment in the diffraction fringes provides evidence for at least some degree of self-assemblage.

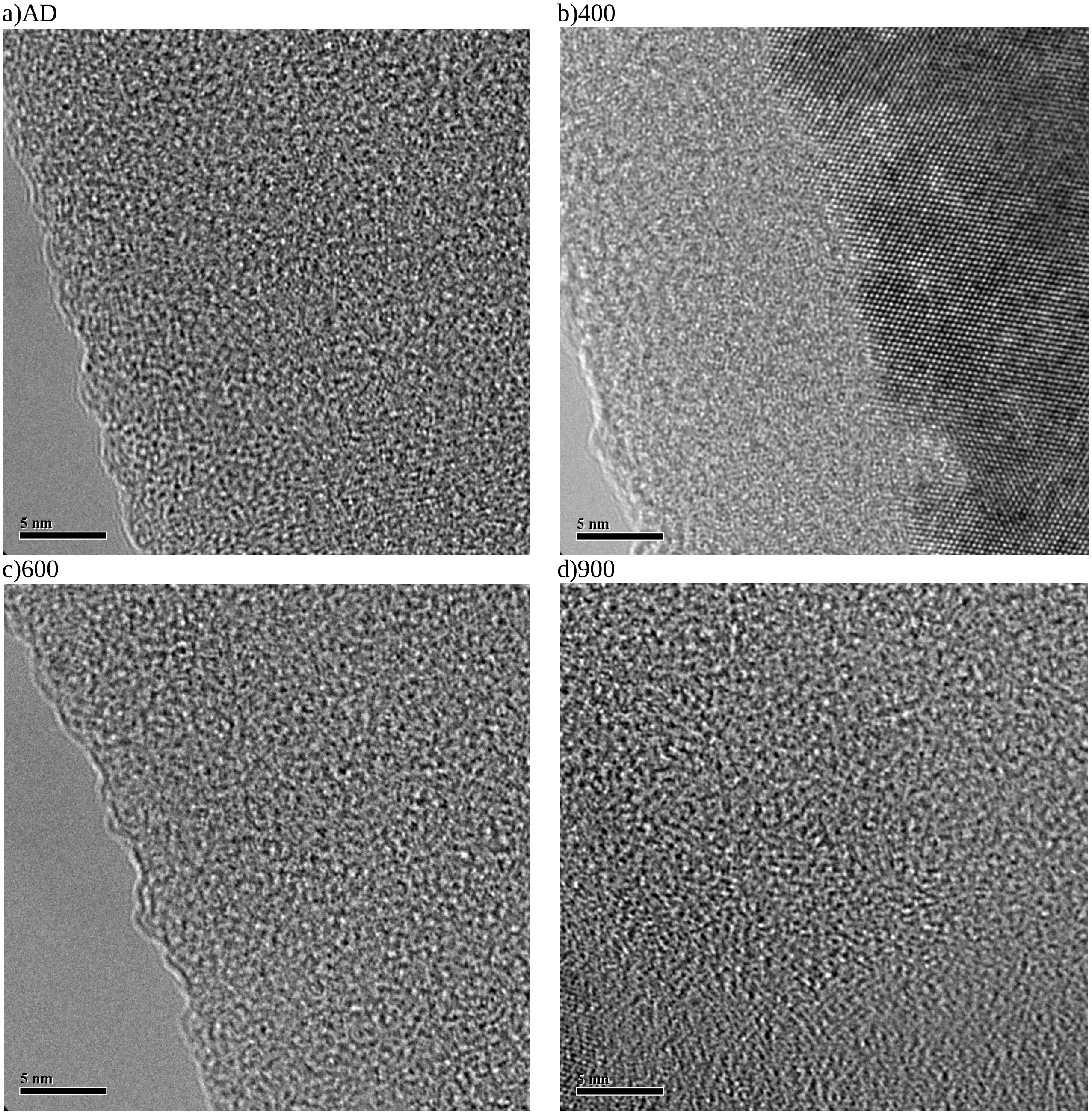

Figure 5-26: HR-TEM showing small nanocrystals formed in the as-deposited and annealed film.

Selected area diffraction (SAD) was applied to each film producing diffraction patterns similar to that found in Figure 5-27 with a pair of concentric rings, reflecting the random alignment found in amorphous/polycrystalline films. Figure 5-27 shows most clearly the nanocrystalline nature of the film as the inner ring at 0.4 nm^{-1} from the straight through beam is most clearly defined. Though this is in the as-deposited film, measurement of other films gave a less clearly defined ring. To obtain a diffraction pattern with the ring well-defined requires measurement of an area where the film is extremely thin. Since there is a distribution of nanocrystal sizes, usually very small, each nanocrystal can exhibit different bond lengths depending on the local environment. Such well defined diffraction rings could not be obtained in the samples annealed at 600 and 900˚C since a suitably thin area could not be found. This inner ring and the faint diffraction spots are most likely silicon nanocrystals, though the formation other small nanocrystals of different composition cannot be ruled out.

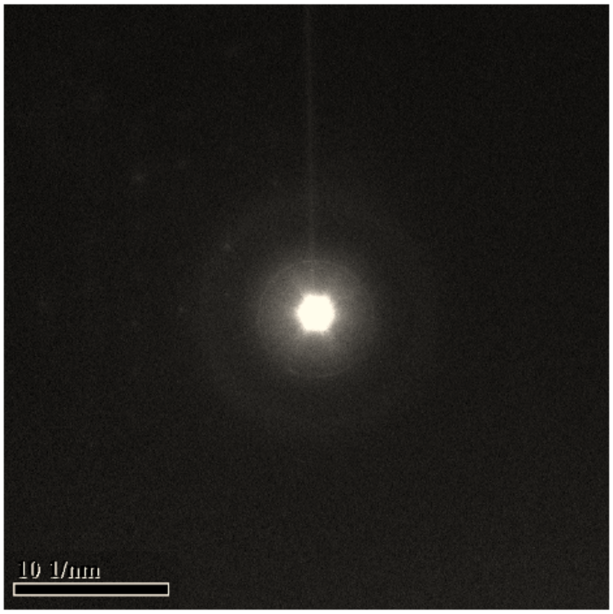

Figure 5-27: SAD from a thin region of sample SCNI505b-AD.

Though difficult to make out at the higher resolutions, there is also evidence of larger, less dense inhomogeneities, as can be seen in Figure 5-28. These large inhomogeneities are of varying size and shape and do not seem to be associated with any crystalline formations.

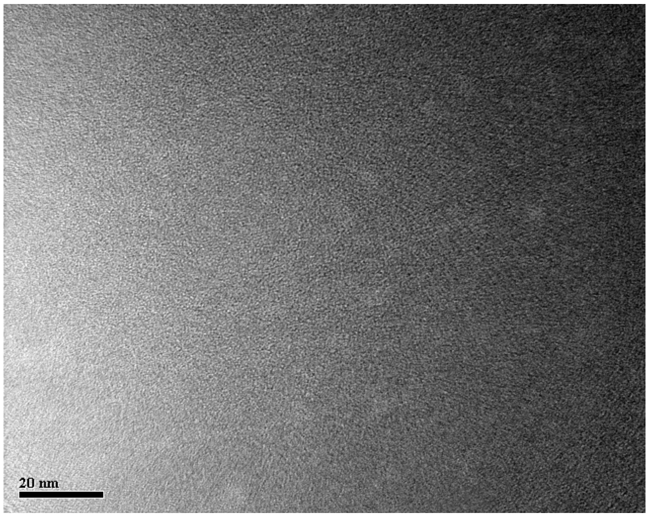

Figure 5-28: Bright field image showing low density inhomogeneities, the lighter regions in the right half of the image.

To more accurately determine the local structure and chemical characteristics of the films, these same samples were examined with dark field imaging and STEM was applied to several of these apparent inhomogeneities. However, in these dark field images no evidence of crystallinity could be observed. Several STEM-EELS line scans were performed. By analyzing the change in peak intensities over the silicon L_{23} edge, carbon K-edge, and nitrogen K-edge at each point one can develop a map of the relative change in compositions over the area subjected to the scan. From these scans it is clear that the low-density inhomogeneities are associated with the migration of silicon and nitrogen atoms out of this region, while little change in the carbon content occurs. This is consistent with other studies, as well as theoretical results, which find that a two phase mixture consisting of Si_3N_4 and C_3N_4 (without considering the presence of hydrogen) is thermodynamically preferred.

An even more convincing example of the two phase structure is seen in Figure 5-29. A set of two dimensional, false color, STEM-EELS maps show clearly the reduction of both silicon and nitrogen content in regions with a high concentration of carbon. This is a clear example of the sample segregating into a carbon rich and a silicon and nitrogen rich region. Indeed, this is what one would expect if one simply compared the bond energies of Si-Si (222 kJ/mol), C-C (346 kJ/mol), Si-C (318 kJ/mol), and Si-N (355 kJ/mol).

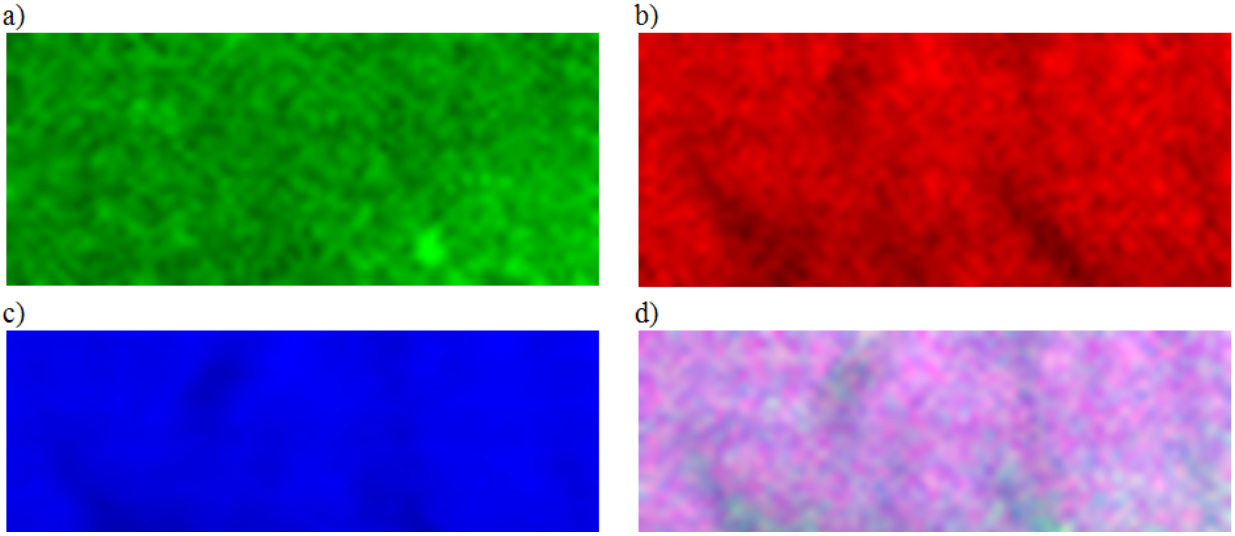

Figure 5-29: STEM-EELS map of integrated high-loss signals of a) carbon, b) nitrogen, c) silicon. d) a compositional map formed through addition of a), b), c).

The major result of the TEM work then is that the film segregates into a two phase system of silicon nitride and a carbon rich region consisting of graphitic bonding as well as carbon-nitrogen bonding (known from the FTIR). It is hypothesized then that a reduction of deposition temperature, as well as possibly annealing temperature, could result in a greater proportion of the film existing in a silicon carbon nitride phase due to decreased adatom mobility.

Electron Energy Loss Spectroscopy and EFTEM

EELS analysis was performed on some annealed films from sample SCNI505a, the sample produced with minimum argon flow that produced the most intense photoluminescent spectrum, using the FEI Titan 80-300. Figure 5-30 shows a typical EELS spectrum. The large peak at the beginning is the zero loss peak with the structure associated with the silicon L-edge excitation at approximately 99 eV, the carbon K-edge at approximately 275 eV and the nitrogen K-edge at approximately 390 eV. Clearly, the silicon signal is much larger than either the carbon or nitrogen edges, which is in agreement with the RBS results. There are hints of fine structure present, but the energy resolution is too low to provide conclusive results. No plasmon loss structure can be resolved, and very little of the fine structure of the sample is present. It can be said that, in agreement with the XAS spectra considered earlier, no large amount of Si-Si bonding is present, given the absence of a peak at 99.7 eV. There is also a definite shoulder present on the low energy side of the carbon K-edge. At higher resolutions this shoulder is normally resolved into a peak, which, according to the literature, is associated with a 1s-π^* transition found in graphite, and hence is indicative of carbon in an sp^2 hybridized state. Again, this is consistent with the two phase model proposed for a- SiC_xN_y.

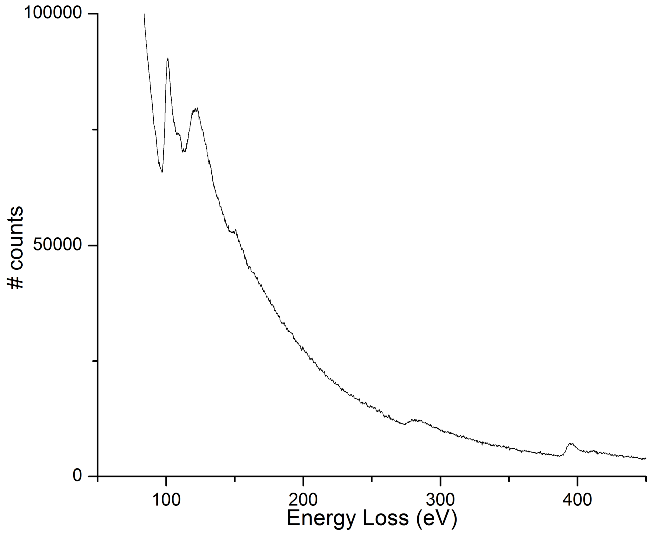

Figure 5-30: EELS spectrum of sample SCNI505b-400. The features are typical for all investigated samples.

EELS linescans performed in the TEM yield fairly conclusive results regarding the micro-structure of these films. In Figure 5-31 the results of a typical linescan and a dark field image showing the path the scan was taken over is provided. It shows a significant decrease in the amount of silicon and nitrogen with an increase in the concentration of carbon. One should look at the changes in intensity as representative of changes in the proportion of that element. However, as the ranges of integration are different for each element, to maximize signal intensity relative to the background while attempting to minimize the overlap between absorption edges, the signals from each element cannot be directly compared. These results are qualitatively consistent with the FTIR results and provide insight into the bonding arrangement even though the scans themselves are of insufficient resolution to directly determine bonding coordinations from them.

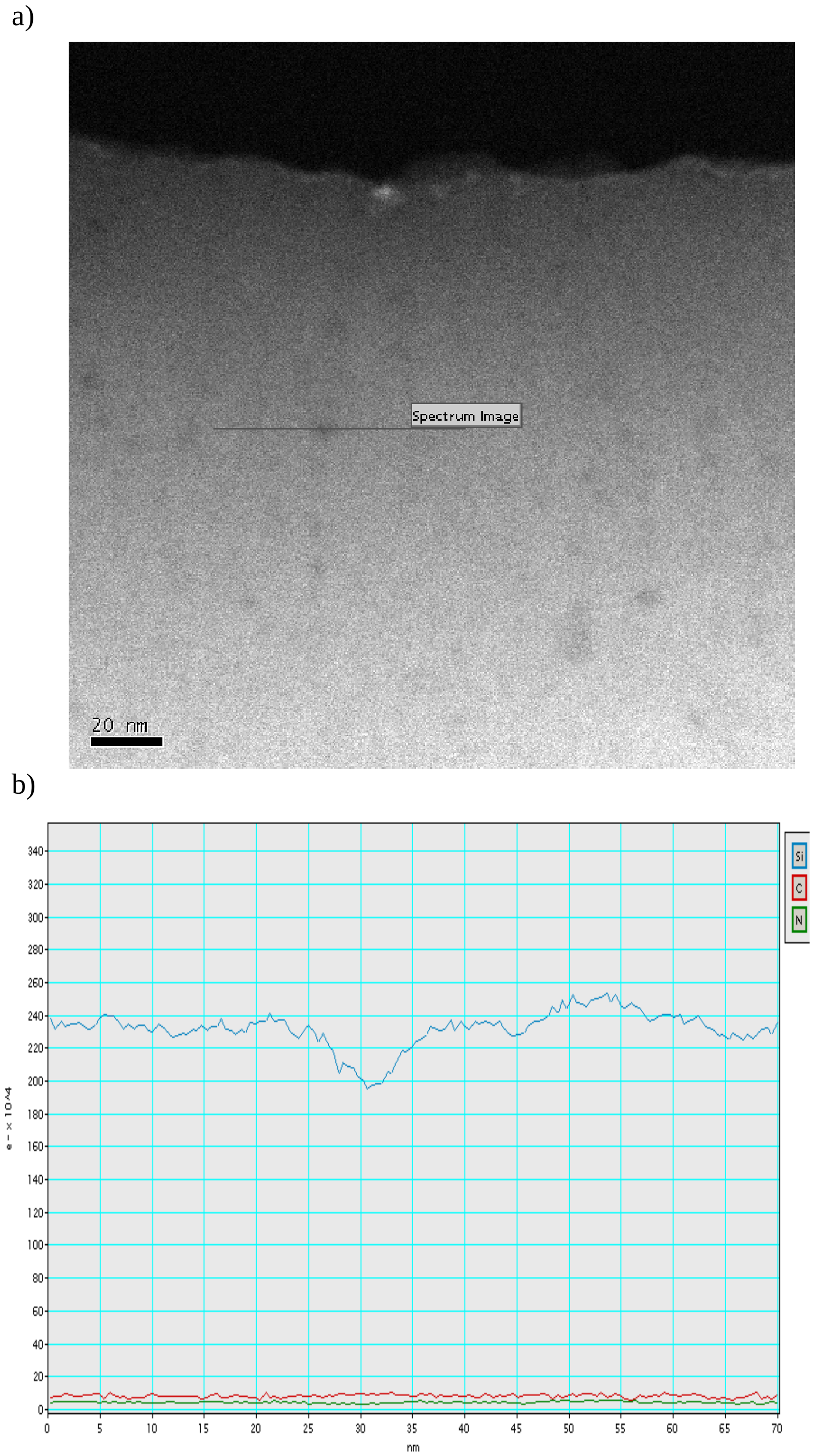

Figure 5-31: a) Dark field image showing low density regions (the darker spots) in the 400˚C annealed film. The line labelled spectrum image shows the path of the beam over the line scan. B) Integrated EELS spectrum for Si (blue), C (red), N (green) show the relative changes in signal intensity for each elements K-edge signal. The large dip in silicon content occurs at the low density region. In the same region there is also a reduction in the nitrogen signal, and a rise in the carbon signal, though these are harder to distinguish.

Chapter 6 : Future Work

Due to the exploratory nature of this thesis several potential avenues of study have opened up. Generally these can be divided into three categories of study: optimizing the sample manufacturing process, examining the structure and properties of the films, and trying to develop them for specific applications.

The easiest and most intuitive follow up to this work would be to continue depositing more films while varying more widely the various deposition parameters and using smaller differences between depositions and annealing temperatures and times. Particularly interesting are more carbon rich films similar to SCNI511, which displayed a much higher PL signal than expected. Developing a model for the film growth dynamics could prove particularly fruitful as a true optimization scheme could be employed in determining the growth parameters instead of the exploratory search method used in this thesis. As well, increasing the total gas flows, and hence the pressure in the chamber during film deposition would increase the growth rate. It is well known that for other materials a low growth rate can promote cluster/crystal formation during growth, and this could be beneficial for the luminescent efficiency. The temperatures attained during deposition are actually not that high (less than 200˚C at its highest). Increasing the surface temperature of the substrate during deposition seems to have a beneficial effect on the luminescence for the samples where the oxide was removed prior to deposition. That brings us to another rather surprising facet of this study, the role that the native oxide plays on film structure and luminescence. Comparing in more detail and more extensively the differences between etched and non-etched samples, as well as introducing other sample pre-treatments, could prove critical in trying to develop devices. The broad radiation profile of the films lends itself well to a basic science study examining the optical excitation and subsequent luminescence of rare earth ions in the more complicated SiC_xN_y (compared to silicon nitride) matrix.

One of the limitations of this thesis is the small quantity of XAS data obtained, particularly silicon K-edge data, but also carbon and nitrogen K-edges. These spectra are much more conclusive than L-edge results since they are more chemically specific, reducing the overlap between edges that was found in the EELS measurements. Further XAS measurements would also serve to explain the seeming contradiction of the FTIR fitting process with the predicted structure and with the core electron excitation experiments. Raman spectroscopy allows one to probe the vibrational structure of materials with bonds that are infrared inactive, relevantly Si-Si, C-C, and N-N. This would serve as a useful complement to the FTIR data already obtained and provide further description of the inconsistency with the advantage that it can be performed at McMaster.

The limited spectral range of the photoluminescence setup was quite vexing as it cuts off the high energy side of the photoluminescence curves. At least a few measurements should be done while detecting at higher energies. The few time dependent PL measurements which were performed showed promising results. A more systematic study could give significant insight into the luminescence mechanism, as well as its suitability for integrated optics. Photoluminescence excitation measurements (preferably spectroscopic), would likewise be useful as the excited and hence the PL signal can change significantly depending on the exciting wavelength. As well, there is a great deal of uncertainty in the RBS/ERD measurements due to the presence of carbon as well as large amounts of hydrogen. Possible experiments to be performed include a high temperature, long duration anneal to drive off all the hydrogen and minimize its effects or possibly switch to using NRA at the University of Western Ontario as the composition measurement technique.

Finally, developing a-SiC$_x$N$_y$:H into an electrically stimulated device structure will entail a great deal of work. The first issue to be overcome is contacting. I have tried using ITO on top of the film and aluminum underneath the substrate, i.e. an MIS structure, but attempting to drive a current through these films has resulted in no luminescence. A word to my successors: most of the aluminum contacts were put on using the aluminum evaporator in room A304 which produced films with extremely poor adherence. The actual sample size with well adhered aluminum contacts is small, limited to a few samples made using the home-built magnetron sputtering system in the Tandem Accelerator Building. As well, the film's DC and RF electrical characteristics should be examined, likely using a four point probe. Finally, electrical defects will need to be examined and minimization techniques proposed, to maximize luminescent efficiency.

Chapter 7 : Conclusions

The need for a CMOS compatible injection laser for optical interconnects, as identified in Chapter 1, is the most likely and most important application for luminescent silicon. The standard materials that have been studied in the past include porous silicon, silicon-rich silicon oxide and silicon nitride, as well as rare earth doped versions suitable for telecom application. However, efficient electroluminescence has proven to be an elusive target that is still the object of many vigorous research programs. Silicon nitride was identified as a potentially useful material for electroluminescence by virtue of its much smaller and direct bandgap when compared to silicon oxide based materials. It also serves as a base structure for the much less studied silicon carbon nitride films that have an even smaller direct bandgap. Noting the trend towards smaller bandgap materials and lower operating voltages in microcomputing, SiC_xN_y could play a critical role in the microelectronics of the future.

While there has been fairly extensive work on SiC_xN_y in the tribological community it remains relatively unstudied for light source applications. This thesis is a first attempt at a broad ranging study of the role carbon plays in luminescent a-SiC_xN_y:H thin films. After going into some detail regarding the technical problem found in microprocessors, the most successful competing technologies are discussed and contrasted to the defect and quantum confinement approach that is utilized here. Descriptions of some relevant properties of the more traditional materials are given before a fairly extensive discussion of the work that has been done to date on silicon carbon nitride. The material deposition system, inductively coupled plasma chemical vapour deposition, and the growth of the films are described. Finally, the basic theoretical principles of the various experimental techniques are provided.

The discussion of the experimental results begins with RBS and ERD for compositional analysis. Significant difficulties are encountered due to the low sensitivity of the technique to carbon and significant hydrogen content. However, while absolute measurements are subject to abnormally large uncertainties, the expected tendency of composition to scale with gas flow rates during deposition is not refuted. Indirect confirmation is also provided by every experimental technique which measures across the different sample depositions. Ellipsometric results confirm this through a tendency to higher refractive indices with increasing inclusion of carbon into a silicon nitride-like host matrix. This can have profound effects on the luminescent efficiency, playing a particularly important role in the thermal evolution of the film. This eliminates the thermal breakdown of the film that has previously been observed and lowers the temperature at which the maximum photoluminescence signal is observed.

FTIR spectroscopy was applied to a series of specially deposited samples to provide information on the vibrational structure of the films and serve as an indirect probe of the bonding environment. While large amounts of data were obtained, unrealistic Gaussian fits cast doubt on their validity in certain regions of the spectrum, leaving mostly smaller satellite peaks to be interpreted. The hydrogen environment of nitrogen has been identified as serving as an indicator for the intensity of the luminescence.

PL spectroscopy results show a great deal of similarity to silicon nitride films, though with the higher energy signal reduced to a mere shoulder. In keeping with the literature these peaks are assigned to defect levels associated with abnormal atomic coordinations of silicon and nitrogen atoms. Increasing the carbon content from a pure SRSN sample mainly results in a reduction of the PL intensity especially the low wavelength shoulder. However sample SCNI511, the most carbon rich sample, displays significant luminescence, likely representing a new growth/chemical bonding regime. Altering the deposition process, especially the substrate heater temperature, can play a profound role in the PL intensity. The overall shape of the spectrum is mostly unchanged, though significant shifting can occur. As well, excess PL signal near the short wavelength detection limits of the PL detector could be evidence of additional defect levels associated with carbon or of a higher energy peak's tail. PL intensity was found to be a maximum between 500 and 700˚C and exhibited a shift with annealing consistent with a quantum confinement model of luminescence.

UV-vis absorption measurements, and to a lesser extent the ellipsometry results, did show the expected bandgap reduction that occurs with increased carbon content. Two bandgaps have been identified, one associated with silicon nitride and the other with the more silicon rich form of silicon carbon nitride. Unfortunately, this is matched by a reduction and shift of the PL signal to longer wavelengths, indicating that the silicon carbon nitride phases are not involved in the luminescence and act to dampen the PL intensity.

Some silicon L-edge XAS results have been obtained at the CLS and are extremely similar to those obtained from silicon nitride films deposited on the ICP-CVD. This implies that silicon tends to bond with nitrogen and hydrogen, but not carbon. This conflict with the FTIR data is responsible for the lack of confidence in the fitting procedure used there. The XAS results indicate a progressively more oxide-like film as the annealing temperature increases, with the silicon nitrogen related bonding structure gradually disappearing.

To examine the film microstructure more conclusively TEM and STEM EELS measurements have been performed at the CCEM. The presence of nanocrystals is confirmed through the use of bright field imaging and is supported by the electron diffraction results. The imaging and STEM EELS results clearly display segregation into two phases: a silicon nitride region and a carbon rich region with the carbon possessing at least some sp^2 character. Thus the main luminescence mechanisms remain the same as in silicon nitride, though dampened by the presence of these carbon rich regions.

Chapter 8 References

[1] G. E. Moore, “Cramming more components onto integrated circuits,” *Proceedings of the IEEE*, vol. 38, no. 1, 1965.

[2] J. Plummer, M. D. Deal, and P. B. Griffin, *Silicon VLSI Technology*. Pearson Higher Education & Professional Group, 2000.

[3] A. Allan, D. Edenfeld, W. Joyner, A. Kahng, M. Rodgers, and Y. Zorian, “International Technology Roadmap for Semiconductors: Interconnect.” 2009.

[4] O. Boyraz and B. Jalali, “Demonstration of a silicon Raman laser,” *Optics Express*, vol. 12, no. 21, p. 5269, 2004.

[5] A. W. Fang, H. Park, O. Cohen, R. Jones, M. J. Paniccia, and J. E. Bowers, “Electrically pumped hybrid AlGaInAs-silicon evanescent laser,” *Optics Express*, vol. 14, no. 20, p. 9203, 2006.

[6] S. G. Cloutier, P. A. Kossyrev, and J. Xu, “Optical gain and stimulated emission in periodic nanopatterned crystalline silicon,” *Nature Materials*, vol. 4, no. 12, p. 887, Nov. 2005.

[7] L. T. Canham, “Silicon quantum wire array fabrication by electrochemical and chemical dissolution of wafers,” *Applied Physics Letters*, vol. 57, no. 10, p. 1046, 1990.

[8] T. V. Torchynska, J. Palacios Gomez, G. P. Polupan, F. G. Becerril Espinoza, A. Garcia Borquez, N. E. Korsunskaya, and L. Y. Khomenkova, “Complex nature of the red photoluminescence band and peculiarities of its excitation in porous silicon,” *Applied Surface Science*, vol. 167, no. 3-4, p. 197, 2000.

[9] L. Nikolova, R. G. Saint-Jacques, and G. G. Ross, “Characterization of Si nanocrystals by different TEM-based techniques,” *Ultramicroscopy*, vol. 110, no. 2, p. 144, 2010.

[10] F. Iacona, G. Franzò, and C. Spinella, “Correlation between luminescence and structural properties of Si nanocrystals,” *Journal of Applied Physics*, vol. 87, no. 3, p. 1295, 2000.

[11] E. Quiroga, W. Bensch, M. Aceves, J. P. Savy, M. Haeckel, and A. Lechner, “Silicon Rich Oxide with controlled mean size of silicon nanocrystals bydeposition in multilayers,” in *Proceedings of the 10th International Conference on ULtimate Integration of Silicon*, Aachen, Germany, 2009, p. 349.

[12] T. Creazzo, B. Redding, E. Marchena, J. Murakowski, and D. W. Prather, “Tunable photoluminescence and electroluminescence of size-controlled silicon nanocrystals in nanocrystalline-Si/SiO2 superlattices,” *Journal of Luminescence*, vol. 130, no. 4, p. 631, 2010.

[13] S. Prezioso, A. Anopchenko, Z. Gaburro, L. Pavesi, G. Pucker, L. Vanzetti, and P. Bellutti, “Electrical conduction and electroluminescence in nanocrystalline silicon-based light emitting devices,” *Journal of Applied Physics*, vol. 104, no. 6, p. 063103, 2008.

[14] R. Soulairol and F. Cleri, “Interface structure of silicon nanocrystals embedded in an amorphous silica matrix,” *Solid State Sciences*, vol. 12, no. 2, p. 163, 2010.

[15] M. Ippolito, S. Meloni, and L. Colombo, “Interface structure and defects of silicon nanocrystals embedded into a-SiO2,” *Applied Physics Letters*, vol. 93, no. 15, p. 153109, 2008.

[16] L. J. Borrero-González, L. A. O. Nunes, M. R. B. Andreeta, J. Wojcik, P. Mascher, Y. A. Pusep, D. Comedi, and F. E. G. Guimarães, “The role of quantum confinement and crystalline structure on excitonic lifetimes in silicon nanoclusters,” *Journal of Applied Physics*, vol. 108, no. 1, p. 013105, 2010.

[17] K. Dunn, J. Derr, T. Johnston, M. Chaker, and F. Rosei, “Multiexponential photoluminescence decay of blinking nanocrystal ensembles,” *Physical Review B*, vol. 80, no. 3, p. 035330, Jul. 2009.

[18] L. Pavesi, L. Dal Negro, C. Mazzoleni, G. Franzo, and F. Priolo, “Optical gain in silicon nanocrystals,” *Nature*, vol. 408, no. 6811, p. 440, 2000.

[19] L. Pavesi, “Silicon Nanophotonics,” presented at the BIMR Seminar, McMaster University, 2010.

[20] M. Ray, T. S. Basu, A. Jana, N. R. Bandyopadhyay, S. M. Hossain, A. K. Pramanick, and R. F. Klie, “Luminescent core-shell nanostructures of silicon and silicon oxide: Nanodots and nanorods,” *Journal of Applied Physics*, vol. 107, no. 6, p. 064311, 2010.

[21] A. J. Kenyon, “Erbium in silicon,” *Semiconductor Science and Technology*, vol. 20, p. R65, 2005.

[22] O. Jambois, Y. Berencen, K. Hijazi, M. Wojdak, A. J. Kenyon, F. Gourbilleau, R. Rizk, and B. Garrido, “Current transport and electroluminescence mechanisms in thin SiO_2 films containing Si nanocluster-sensitized erbium ions,” *Journal of Applied Physics*, vol. 106, no. 6, p. 063526, 2009.

[23] P. Pellegrino, A. Pérez-Rodriguez, B. Garrido, O. González-Varona, J. R. Morante, S. Marcinkevičius, A. Galeckas, and J. Linnros, “Time-resolved analysis of the white photoluminescence from SiO_2 films after Si and C coimplantation,” *Applied Physics Letters*, vol. 84, no. 1, p. 25, 2004.

[24] L. Dal Negro, J. H. Yi, L. C. Kimerling, S. Hamel, A. Williamson, and G. Galli, “Light emission from silicon-rich nitride nanostructures,” *Applied Physics Letters*, vol. 88, no. 18, p. 183103, 2006.

[25] T.-W. Kim, C.-H. Cho, B.-H. Kim, and S.-J. Park, “Quantum confinement effect in crystalline silicon quantum dots in silicon nitride grown using SiH_4 and NH_3,” *Applied Physics Letters*, vol. 88, no. 12, p. 123102, 2006.

[26] P. R. Wilson, T. Roschuk, O. Zalloum, J. Wojcik, and P. Mascher, “The Effects of Deposition and Processing Parameters on the Electronic Structure and Photoluminescence from Nitride-Passivated Silicon Nanoclusters,” in *ECS Transactions*, Honolulu, HI, 2009, p. 33.

[27] K. Ma, J. Y. Feng, and Z. J. Zhang, “Improved photoluminescence of silicon nanocrystals in silicon nitride prepared by ammonia sputtering,” *Nanotechnology*, vol. 17, no. 18, p. 4650, 2006.

[28] B. Rezgui, A. Sibai, T. Nychyporuk, M. Lemiti, and G. Brémond, “Photoluminescence and optical absorption properties of silicon quantum dots

embedded in Si-rich silicon nitride matrices," *Journal of Luminescence*, vol. 129, no. 12, p. 1744, 2009.

[29] S. V. Deshpande, E. Gulari, S. W. Brown, and S. C. Rand, "Optical properties of silicon nitride films deposited by hot filament chemical vapor deposition," *Journal of Applied Physics*, vol. 77, no. 12, p. 6534, 1995.

[30] W. L. Warren, J. Kanicki, J. Robertson, E. H. Poindexter, and P. J. McWhorter, "Electron paramagnetic resonance investigation of charge trapping centers in amorphous silicon nitride films," *Journal of Applied Physics*, vol. 74, no. 6, p. 4034, 2009.

[31] M. Wang, D. Li, Z. Yuan, D. Yang, and D. Que, "Photoluminescence of Si-rich silicon nitride: Defect-related states and silicon nanoclusters," *Applied Physics Letters*, vol. 90, no. 13, p. 131903, 2007.

[32] M. Wang, M. Xie, L. Ferraioli, Z. Yuan, D. Li, D. Yang, and L. Pavesi, "Light emission properties and mechanism of low-temperature prepared amorphous SiN_x films. I. Room-temperature band tail states photoluminescence," *Journal of Applied Physics*, vol. 104, no. 8, p. 083504, 2008.

[33] Z. H. Cen, T. P. Chen, Z. Liu, Y. Liu, L. Ding, M. Yang, J. I. Wong, S. F. Yu, and W. P. Goh, "Electrically tunable white-color electroluminescence from Si-implanted silicon nitride thin film," *Optics Express*, vol. 18, no. 19, p. 20439, 2010.

[34] Z. H. Cen, T. P. Chen, L. Ding, Y. Liu, J. I. Wong, M. Yang, Z. Liu, W. P. Goh, F. R. Zhu, and S. Fung, "Evolution of electroluminescence from multiple Si-implanted silicon nitride films with thermal annealing," *Journal of Applied Physics*, vol. 105, no. 12, p. 123101, 2009.

[35] M. Wang, J. Huang, Z. Yuan, A. Anopchenko, D. Li, D. Yang, and L. Pavesi, "Light emission properties and mechanism of low-temperature prepared amorphous SiN_x films. II. Defect states electroluminescence," *Journal of Applied Physics*, vol. 104, no. 8, p. 083505, 2008.

[36] D. Li, J. Huang, and D. Yang, "Electroluminescence of silicon-rich silicon nitride light-emitting devices," in *Group IV Photonics, 2008 5th IEEE International Conference on*, Sorrento, Italy, 2008, p. 119.

[37] Z. Jiang, X. Xu, H. Wu, F. Zhang, and Z. Jin, "Ab initio calculation of SiC polytypes," *Solid State Communications*, vol. 123, no. 6-7, p. 263, 2002.

[38] O. Madelung, *Semiconductors: Data Handbook*, 3rd ed. Springer, 2003.

[39] M. Künle, T. Kaltenbach, P. Löper, A. Hartel, S. Janz, O. Eibl, and K. G. Nickel, "Si-rich a-SiC: H thin films: Structural and optical transformations during thermal annealing," *Thin Solid Films*, vol. 519, no. 1, p. 151, 2010.

[40] D. Song, E. C. Cho, Y. H. Cho, G. Conibeer, Y. Huang, S. Huang, and M. A. Green, "Evolution of Si (and SiC) nanocrystal precipitation in SiC matrix," *Thin Solid Films*, vol. 516, no. 12, p. 3824, 2008.

[41] Z. Li, J. Zhang, H. He, J. Bian, X. Zhang, and G. Han, "Blue–green luminescence and SERS study of carbon-rich hydrogenated amorphous silicon carbide films with multiphase structure," *physica status solidi (a)*, vol. 207, no. 11, p. 2543, 2010.

[42] A. V. Vasin, S. P. Kolesnik, A. A. Konchits, A. V. Rusavsky, V. S. Lysenko, A. N. Nazarov, Y. Ishikawa, and Y. Koshka, "Structure, paramagnetic defects and light-

emission of carbon-rich a-SiC:H films," *Journal of Applied Physics*, vol. 103, no. 12, p. 123710, 2008.

[43] K. Chew, Rusli, S. F. Yoon, J. Ahn, Q. Zhang, V. Ligatchev, E. J. Teo, T. Osipowicz, and F. Watt, "Gap state distribution in amorphous hydrogenated silicon carbide films deduced from photothermal deflection spectroscopy," *Journal of Applied Physics*, vol. 91, no. 7, p. 4319, 2002.

[44] V. I. Ivashchenko, V. I. Shevchenko, G. V. Rusakov, A. S. Klymenko, V. M. Popov, L. A. Ivashchenko, and E. I. Bogdanov, "Gap states in a-SiC from optical measurements and band structure models," *Journal of Physics: Condensed Matter*, vol. 14, no. 8, p. 1799, 2002.

[45] R. Fischer and E. O. Gobel, "Carrier relaxation in a-Si1-xCx: H studied by picosecond photoluminescence spectroscopy," *Journal of Non-Crystalline Solids*, vol. 114, no. 2, p. 570, 1989.

[46] S. Kivanc, B. Akaoglu, O. Ozdemir, and I. Atilgan, "Electroluminescence properties of a PIN structure made by nearly stoichiometric a-SiCx:H active layer," *Vacuum*, vol. 83, no. 5, p. 813, Jan. 2009.

[47] X. Huang, T. Ma, J. Xu, Z. Li, J. Mei, X. Li, W. Li, X. Huang, and K. Chen, "Visible electroluminescence from amorphous hydrogenated silicon carbide prepared by using organic carbon source," *Diamond and Related Materials*, vol. 12, no. 10-11, p. 1932, 2003.

[48] H. Zhang, "Study of Optimal Deposition Conditions for an Inductively Coupled Plasma Chemical Vapour Deposition (ICP-CVD) System," M.A.Sc., McMaster University, 2005.

[49] B. Batell and B. Ferstl, "Electrically induced magnetic fields; a consistent approach," *American Journal of Physics*, vol. 71, no. 9, p. 925, 2003.

[50] G. Cunge, B. Crowley, D. Vender, and M. M. Turner, "Characterization of the E to H transition in a pulsed inductively coupled plasma discharge with internal coil geometry: bi-stability and hysteresis," *Plasma Sources Science and Technology*, vol. 8, no. 4, p. 576, 1999.

[51] U. Kortshagen, N. D. Gibson, and J. E. Lawler, "On the E-H mode transition in RF inductive discharges," *Journal of Physics D: Applied Physics*, vol. 29, no. 5, p. 1224, 1996.

[52] M. Ohring, *Materials Science of Thin Films: Deposition and Structure*, 2nd ed. Academic Press, 2002.

[53] G. R. Carlow and M. Zinke-Allmang, "Clustering Across Concentration Gradients," *Canadian Journal of Physics*, vol. 72, no. 11-12, p. 812, 1994.

[54] I. C. Markov, *Crystal Growth for Beginners*, 2nd ed. World Scientific Publishing Co., 2004.

[55] S. Logothetidis, M. Gioti, and P. Patsalas, "Real-time monitoring, growth kinetics and properties of carbon based materials deposited by sputtering," *Diamond and Related Materials*, vol. 10, no. 2, p. 117, 2001.

[56] C. Popov, M. F. Plass, R. Kassing, and W. Kulisch, "Plasma Chemical Vapor Deposition of Thin Carbon Nitride Films Utilizing Transport Reactions," *Thin Solid Films*, vol. 355-356, p. 406, 1999.

[57] W. F. A. Besling, A. Goossens, B. Meester, and J. Schoonman, "Laser-induced chemical vapor deposition of nanostructured silicon carbonitride thin films," *Journal of Applied Physics*, vol. 83, no. 1, p. 544, 1998.

[58] L. Operti, R. Rabezzana, F. Turco, and G. A. Vaglio, "Gas-phase ion chemistry of the propyne/ammonia and silane/propyne/ammonia systems," *International Journal of Mass Spectrometry*, vol. 232, no. 2, p. 139, 2004.

[59] B. F. Hanyaloglu and E. S. Aydil, "Low temperature plasma deposition of silicon nitride from silane and nitrogen plasmas," *Journal of Vacuum Science & Technology A: Vacuum, Surfaces, and Films*, vol. 16, no. 5, p. 2794, 1998.

[60] C. W. Chen, "Structural and electronic properties of wide band gap silicon carbonnitride materials—a first-principles study," *Diamond and Related Materials*, vol. 13, no. 4-8, p. 1158, 2004.

[61] N. Resta, C. Kohler, and H. R. Trebin, "Molecular Dynamics Simulations of Amorphous Si–C–N Ceramics: Composition Dependence of the Atomic Structure," *Journal of the American Ceramic Society*, vol. 86, no. 8, p. 1409, 2003.

[62] M. Amkreutz and T. Frauenheim, "Understanding precursor-derived amorphous Si-C-N ceramics on the atomic scale," *Physical Review B*, vol. 65, no. 13, p. 134113, Mar. 2002.

[63] J. Dürr, P. Lamparter, J. Bill, S. Steeb, and F. Aldinger, "An X-ray and neutron scattering investigation of precursor derived $Si_{24}C_{43}N_{33}$ ceramics," *Journal of Non-Crystalline Solids*, vol. 232-234, no. 11, p. 155, 1998.

[64] A. Y. Liu and M. L. Cohen, "Prediction of New Low Compressibility Solids," *Science*, vol. 245, no. 4920, p. 841, 1989.

[65] R. Riedel, A. Greiner, G. Miehe, W. Dressler, H. Fuess, J. Bill, and F. Aldinger, "The First Crystalline Solids in the Ternary Si-C-N System," *Angewandte Chemie International Edition in English*, vol. 36, no. 6, p. 603, 1997.

[66] L. C. Chen, C. K. Chen, S. L. Wei, D. M. Bhusari, K. H. Chen, Y. F. Chen, Y. C. Jong, and Y. S. Huang, "Crystalline silicon carbon nitride: A wide band gap semiconductor," *Applied Physics Letters*, vol. 72, no. 19, p. 2463, 1998.

[67] N. I. Fainer, M. L. Kosinova, Y. M. Rumyantsev, E. A. Maximovskii, and F. A. Kuznetsov, "Thin silicon carbonitride films are perspective low-k materials," *Journal of Physics and Chemistry of Solids*, vol. 69, no. 2-3, p. 661, 2008.

[68] C. WenJuan and M. A. XueMing, "Low temperature synthesis of SiCN nanostructures," *Sci China Ser E*, vol. 52, no. 1, p. 28, 2009.

[69] Z. Chen, J. Zhou, X. Song, X. Xu, Y. Liu, J. Song, Z. Ma, and E. Xie, "The effect of annealing temperatures on morphologies and photoluminescence properties of terbium-doped SiCN films," *Optical Materials*, vol. 32, no. 9, p. 1077, 2010.

[70] Y. Liu, X. Zhang, C. Chen, G. Zhang, P. Xu, D. Chen, and L. Dong, "The photoluminescence of SiCN thin films prepared by C+ implantation into [alpha]-SiNx: H," *Thin Solid Films*, vol. 518, no. 15, p. 4363, 2010.

[71] R. Reyes, C. Legnani, P. M. Ribeiro Pinto, M. Cremona, P. J. G. de Araújo, and C. A. Achete, "Room-temperature low-voltage electroluminescence in amorphous carbon nitride thin films," *Applied Physics Letters*, vol. 82, no. 23, p. 4017, 2003.

[72] A. Canillas, A. Pinyol, J. Sancho-Parramon, J. Ferré-Borrull, and E. Bertran, “FTIR phase-modulated ellipsometry characterization of hydrogenated amorphous silicon nitride thin films with embedded nanoparticles,” *Thin Solid Films*, vol. 455-456, p. 167, 2004.

[73] J.-J. Wu, C.-T. Wu, Y.-C. Liao, T.-R. Lu, L. C. Chen, K. H. Chen, L.-G. Hwa, C.-T. Kuo, and K.-J. Ling, “Deposition of silicon carbon nitride films by ion beam sputtering,” *Thin Solid Films*, vol. 355-356, p. 417, 1999.

[74] M. Mayer, “SIMNRA Home Page.” [Online]. Available: http://home.rzg.mpg.de/~mam/. [Accessed: 02-Jun-2011].

[75] M. Mayer, “SIMNRA User’s Guide.” .

[76] J. F. Ziegler, J. P. Biersack, and U. Litmark, *The Stopping and Range of Ions in Solids*, vol. 1. New York: Pergamon Press, 1985.

[77] J. F. Ziegler and J. M. Manoyan, “The stopping of ions in compounds,” *Nuclear Instruments and Methods in Physics Research Section B: Beam Interactions with Materials and Atoms*, vol. 35, no. 3-4, p. 215, 1988.

[78] P. R. Griffiths and J. A. de Haseth, *Fourier Transform Infrared Spectrometry*, 2nd ed. Hoboken, New Jersey: John Wiley & Sons, Inc., 2007.

[79] H. G. Tompkins and E. A. Irene, *Handbook of Ellipsometry*. United States of America: William Andrew, Springer, 2005.

[80] F. Wooten, *Optical Properties of Solids*. New York, New York: Academic Press, 1972.

[81] R. K. Willardson and A. C. Beer, *Transport and Optical Phenomena*, vol. 8. 111 Fifth Avenue, New York, New York: Academic Press, 1972.

[82] O. H. Y. Zalloum, M. Flynn, T. Roschuk, J. Wojcik, E. Irving, and P. Mascher, “Laser photoluminescence spectrometer based on charge-coupled device detection for silicon-based photonics,” *Review of Scientific Instruments*, vol. 77, no. 2, p. 023907, 2006.

[83] D. B. Williams and C. B. Carter, *Transmission Electron Microscopy*. New York, New York: Springer, 2009.

[84] S. R. Elliott, *Physics of Amorphous Materials*, 1st ed. Longman House Ltd., 1984.

[85] F. de Groot and A. Kotani, *Core Level Spectroscopy of Solids*, 1st ed., vol. 6. CRC Press, 2008.

[86] J. Stöhr, *NEXAFS Spectroscopy: Springer Series in Surface Sciences*, vol. 25. Springer Verlag.

[87] R. Franke, S. Bender, A. A. Pavlychev, P. Kroll, R. Riedel, and A. Greiner, “Si and N K-XANES spectroscopic study of novel Si–C–N ceramics,” *Journal of Electron Spectroscopy and Related Phenomena*, vol. 96, no. 1-3, p. 253, 1998.

[88] J. C. H. Spence, “Absorption spectroscopy with sub-angstrom beams: ELS in STEM,” *Reports on Progress in Physics*, vol. 69, no. 3, p. 725, 2006.

[89] C. Rowlands and S. Elliott, “Automated algorithm for baseline subtraction in spectra,” *Journal of Raman Spectroscopy*, vol. 42, no. 3, p. 363, Mar. 2011.

[90] I. Ferreira, E. Fortunato, P. Vilarinho, A. S. Viana, A. R. Ramos, E. Alves, and R. Martins, “Hydrogenated silicon carbon nitride films obtained by HWCVD, PA-

HWCVD and PECVD techniques," *Journal of Non-Crystalline Solids*, vol. 352, no. 9-20, p. 1361, 2006.

[91] H. Y. Lin, Y. C. Chen, C. Y. Lin, Y. P. Tong, L. G. Hwa, K. H. Chen, and L. C. Chen, "Field emission of nanostructured amorphous SiCN films deposited by reactive magnetron sputtering of SiC in CH4/N2 atmosphere," *Thin Solid Films*, vol. 416, no. 1-2, p. 85, 2002.